FRAMEWORK FOR A PRACTICAL AND COST–EFFECTIVE IOT–ENHANCED STRUCTURAL HEALTH MONITORING WITH DIGITAL TWINNING

AUGUST 2024

UNIVERSITEIT VAN PRETORIA
UNIVERSITY OF PRETORIA
YUNIBESITHI YA PRETORIA

FRAMEWORK FOR A PRACTICAL AND COST–EFFECTIVE IOT–ENHANCED STRUCTURAL HEALTH MONITORING WITH DIGITAL TWINNING

JACK HUANG

A dissertation submitted in partial fulfilment of the requirements for the degree of

MASTER OF ENGINEERING (STRUCTURAL ENGINEERING)

In the

FACULTY OF ENGINEERING, BUILT ENVIRONMENT AND INFORMATION TECHNOLOGY

UNIVERSITY OF PRETORIA

August 2024

FRAMEWORK FOR A PRACTICAL AND COST–EFFECTIVE IOT–ENHANCED STRUCTURAL HEALTH MONITORING WITH DIGITAL TWINNING

JACK HUANG

Supervisor: Professor George Markou

Co-supervisor: Dr André Broekman

Department: Civil Engineering

University: University of Pretoria

Degree: Master of Engineering (Structural Engineering)

The South African civil infrastructure is critical for passenger and freight transit, connecting major cities and ports. Despite state-owned investment efforts aimed at maintaining and improving existing infrastructure, it continues to deteriorate rapidly. This degradation negatively impacts the commercial sector and diminishes the country's global economic competitiveness. With increasing traffic volumes to meet escalating transport demands, effective condition assessment and maintenance of existing civil infrastructure are paramount. Currently, the industry primarily relies on visual inspections, which are useful for identifying visible issues but are subjective, inconsistent, and unable to detect internal problems. Other non-destructive methods exist but are often costly, labour intensive, complex and disruptive to operations. These challenges highlight the urgent need for advanced, automated, and timely monitoring approaches to ensure infrastructure integrity, support economic growth, and promote infrastructure sustainability.

The Fourth Industrial Revolution has introduced advanced smart technologies and data-driven solutions, significantly impacting civil infrastructure management. A critical area within this development is Structural Health Monitoring (SHM), which provides stakeholders with valuable insights into infrastructure conditions. The integration of sensor systems, the Internet of Things (IoT), and advanced data processing has led to the concept of Digital Twins (DTs). DTs offer dynamic, real-time simulations of structural behaviours, aiding in proactive asset management by predicting

potential risks and formulating maintenance strategies. However, current DT-based SHM systems often involve prohibitive costs, complex data processing, and demanding computing systems and power, making them impractical and financially unfeasible, especially for small-scale implementations. Additionally, many existing systems lack user-friendly interfaces and interpretability, reducing user confidence and comprehension.

This study aims to establish a practical and cost-effective SHM framework enhanced by DT technology for civil infrastructure. The primary objectives include demonstrating that affordable contact and non-contact sensors can provide precise and reliable results for DT-enhanced SHM frameworks, proving that cost-effective microcomputing hardware with IoT capability can enable efficient, near real-time data transmission from physical structures to digital models, and developing a practical, comparatively simple numerical DT model to simulate the mechanical behaviour of Reinforced Concrete (RC) structures.

The experimental study performed for this research work successfully developed a DT-based SHM prototype capable of digitally replicating the mechanical response of a RC beam. It introduced two novel low-cost sensors: a potentiometer contact sensor, and an Infrared (IR) non-contact sensor. The potentiometer sensor demonstrated excellent accuracy compared to the LVDT control, with an overall absolute error of 41.2 μm, an overall percentage error of 11.2%, and high stability (overall standard deviation of 37.9 μm), making it ideal for precise measurements. In contrast, the IR sensor, tested within a detection range of 50 mm to 70 mm, exhibited lower accuracy with an overall absolute error of 184.8 μm and percentage error of 202.2%, and greater variability (overall standard deviation of 211.7 μm). Despite higher noise levels, the IR sensor effectively detected sub-millimetre displacements. The hardware system, integrating these low-cost sensors with an IoT-enabled Arduino microcontroller and a custom software program, “ReConTwin,” featured an automated post-processing system for near real-time model updates, analysis, and damage diagnosis. The calibrated DT accurately estimated imposed loads with an average absolute error of 2.11 kN and relative error of 11.6%, and predicted strain with an average absolute error of 281 με and relative error of 34.3%, providing reliable insights into the monitored beam’s structural behaviour. The user-friendly design and compatibility with standard commercial computers significantly enhance the accessibility and feasibility of the proposed DT-SHM framework for widespread adoption. The study demonstrates the potential of practical and affordable DT-enhanced SHM systems, making them more accessible for scalable, real-world civil infrastructure applications.

DECLARATION

I, the undersigned hereby declare that:

- I understand what plagiarism is and I am aware of the University's policy in this regard;
- The work contained in this dissertation is my own original work;
- I did not refer to work of current or previous students, lecture notes, handbooks or any other study material without proper referencing;
- Where other people's work has been used this has been properly acknowledged and referenced;
- I have not allowed anyone to copy any part of my dissertation;
- I have not previously in its entirety or in part submitted this dissertation at any university for a degree.

Signature of student: 

Name of student: **Jack Huang**

Student number: **u11007959**

Date: **30 August 2024**

ACKNOWLEDGEMENT

I wish to express my appreciation to the following organisations and persons who made this project dissertation possible:

a) Professor George Markou, my project supervisor, for his guidance and support.

b) Dr André Broekman, for his invaluable technical guidance and unwavering support.

c) The following persons are gratefully acknowledged for their assistance during the course of the study:

   i) Staff from the Department of Civil Engineering: Professor S.W Jacobsz and Dr M. Brink.

   ii) Technical staff from the Engineering 4.0 laboratory: Mr J. Scholtz, Mr J. Mostert, Mr J. Botha and all other support staff.

d) My family and friends for their encouragement and support during the study.

TABLE OF CONTENTS

LIST OF TABLES

LIST OF FIGURES

APPENDIX

LIST OF ABBREVIATIONS

3D	Three-Dimensional
ABS	Acrylonitrile Butadiene Styrene
ADC	Analog-to-Digital Converter
BIM	Building Information Modelling
BLE	Bluetooth Low Energy
BOFDA	Brillouin Optical Frequency Domain Analysis
BOTDR	Brillouin Optical Time Domain Reflectometry
BS	British Standard
CPU	Central Processing Unit
DC	Direct Current
DIC	Digital Image Correlation
DOFS	Distributed Optical Fibre Sensor
DT	Digital Twin
EMI	Electro-Mechanical Impedance
FE	Finite Element
FBG	Fibre Bragg Grating
FEMAP	Finite Element Modelling and Postprocessing (Software)
FO	Fibre Optic
GPS	Global Positioning System
GUI	Graphical User Interface
I/O	Input/Output
IDE	Integrated Development Environment
IEEE	Institute of Electrical and Electronics Engineers
IMU	Inertial Measurement Unit
IoT	Internet of Things

IP	Ingress Protection
IR	Infrared
ISA	International Society of Automation
LED	Light Emitting Diode
LiDAR	Light Detection and Ranging
LoRaWAN	Long Range Wide Area Network
LVDT	Linear Variable Differential Transformer
MAE	Mean Absolute Error
MEMS	Micro-Electro Mechanical System
MS	Microsoft
MTS	Materials Testing System
OPC	Ordinary Portland Cement
RADAR	Radio Detection and Ranging
ReConAn	Reinforced Concrete Analysis (Finite Element Software)
ReConTwin	Reinforced Concrete Twinning (Software developed in this study)
RC	Reinforced Concrete
RTC	Real Time Clock
SAICE	South African Institute of Civil Engineering
SANS	South African National Standards
SD	Standard Deviation
SHM	Structural Health Monitoring
TLS	Terrestrial Laser Scanning
UAV	Unmanned Aerial Vehicles
USB	Universal Serial Bus
USD	United States Dollar
VSC	Visual Studio Code
Wi-Fi	Wireless Fidelity

LIST OF SYMBOLS

A_c	Cross-sectional Area of the Sample Test Cube
d_c	Cross-sectional Dimension of the Cylinder Specimen
E	Young's Modulus of the Material
E_c	Compressive Static Modulus of Elasticity of the Cylinder Specimen
F	Maximum Recorded Load at Failure
f_y	Yield Strength of the Material
f_{cc}	Compressive Cube Strength
f_{ct}	Tensile Splitting Cylinder Strength
L_c	Length of the Cylinder Specimen
KB	Kilobyte
MB	Megabyte
GND	Ground
mg	Milligram
kg	Kilogram
mm^2	Square Millimetre
m^3	Cubic Metres
Hz	Hertz
MHz	Megahertz
GHz	Gigahertz
μm	Micrometre
mm	Millimetre
m	Metre
km	Kilometre
N	Newton
kN	Kilonewton

MPa	Megapascal
GPa	Gigapascal
ms	Millisecond
s	Second
x_i	Wiper Displacement from Zero Position
x_T	Total Length of Wiper Resistive Track
V	Voltage/Volts
V_{cc}	Voltage Common Collector
V_{IN}	Input Voltage
V_{OUT}	Output Voltage
R	Electrical Resistance
$k\Omega$	Kiloohm
mW	Milliwatt
mA	Milliampere
℃	Degree Celsius
σ_U	Upper Loading Stress
σ_L	Lower Loading Stress
$\mu\varepsilon$	Linear Microstrain
ε	Linear Strain
ε_U	Mean Strain under Upper Loading Stress
ε_L	Mean Strain under Lower Loading Stress
∅	Diameter
%	Percent
$	United States Dollar

1 INTRODUCTION

1.1 BACKGROUND

The civil infrastructure is a vital part of the country's transport system, facilitating passenger and freight transit between major cities and ports. Despite continuous improvements and maintenance by state-owned investments, the infrastructure's condition is deteriorating rapidly. Unmaintained, ageing civil infrastructure adversely affects the commercial sector and reduces the country's global economic competitiveness. With increasing traffic volumes to meet escalating transport demands, effective condition assessment and maintenance of existing civil infrastructure have become paramount.

Currently, the industry relies primarily on visual inspections to assess the structural condition of the civil infrastructure. Although visual inspections offer a broad understanding of the structure's apparent condition and identify visible distress, they have significant limitations in accurately identifying structural concerns and defects. Visual inspections can be subjective and inconsistent due to varying training and guidelines (Agdas *et al*., 2019). Moreover, they provide only discrete, point-in-time observations, limiting timely maintenance and rehabilitation decisions and failing to detect internal issues not visible from the surface (Graybeal *et al*., 2022). Other non-destructive inspection methods (ultrasonic, radiography, and magnetic particles) are also commonly employed, but they are often costly, labour-intensive, complex, disruptive to the operations, and potentially dangerous (Cawley, 2001; Nagarajaiah & Erazo, 2016; Rehman *et al*., 2015). These drawbacks highlight the need for advanced, automated, and timely monitoring approaches to ensure infrastructure integrity, support economic growth, and promote engineering sustainability.

The Fourth Industrial Revolution has introduced innovative smart technologies and data-driven solutions, reshaping conventional paradigms in civil infrastructure management. Structural Health Monitoring (SHM) has recently emerged as a key area of research and implementation, offering stakeholders and engineers profound insights into infrastructure conditions. The integration of sensor systems, the Internet of Things (IoT), and advanced data processing capabilities has further enhanced SHM with the novel concept of the Digital Twin (DT). DT offers a more intelligent, interactive, and proactive asset management strategy. By creating a virtual, dynamic representation of the monitored structure, real-time simulation and analysis of structural behaviour can be performed, assisting engineers and asset managers in anticipating potential risks, formulating maintenance strategies, and extending the serviceable life of critical infrastructure.

However, the current landscape of the DT-based SHM systems often lacks integration of cost-effective sensors and IoT technologies, along with simplified post-processing and digital twinning methods. Existing DT systems often involve complex data processing, intricate architectures, and high computing and power demands (Hemdan *et al*., 2023), making them challenging and financially unfeasible, especially for small-scale SHM implementations. Additionally, some DT systems lack interpretability, reducing user comprehension and confidence in diagnostic results. There is a requirement for simpler, user-friendly, and cost-effective post-processing approaches tailored to relatively straightforward monitoring systems. This study aims to demonstrate the feasibility of establishing a practical and cost-effective SHM strategy enhanced by DT technology for civil infrastructure, ultimately making DT-based SHM systems more accessible and practical for scalable adoption in real-world civil infrastructure damage prognosis.

1.2 OBJECTIVES OF THE STUDY

The primary objective of this study is to demonstrate the feasibility of establishing a practical and cost-effective SHM framework enhanced by DT technology for health monitoring of civil infrastructure, validated through experimentation on simply supported Reinforced Concrete (RC) beams under controlled laboratory loading conditions.

The main objectives of the study are summarised as follows:

- Demonstrate that affordable contact and non-contact sensors, dedicated to measuring the displacement of structural members, can provide precise and dependable results with significant potential for incorporation in a DT-enhanced SHM framework. Contact sensors require direct physical attachment to the structure to measure displacement, while non-contact sensors detect displacement changes remotely without physical contact. In the context of this study, the precision of the sensors is defined as their ability to repeatedly achieve sub-millimetre accuracy, while dependability refers to consistent measurement readings across repeated trials, quantified through comparison with control measurements.
- Prove that cost-effective microcomputing hardware with IoT capabilities can enable efficient and near real-time data transmission from the physical structure to digital model of DT.
- Develop and implement a practical and simplified numerical DT model that accurately simulates the mechanical behaviour of a simply supported RC beam. This includes

defining a streamlined approach for data processing, numerical modelling, and validation against experimental results.

Based on the main objectives, this study hypothesises that IoT-enabled, affordable, easily deployable contact and non-contact sensors will achieve a displacement measurement accuracy of 1 mm or better, comparable to the LVDT control sensor. The resulting DT model is expected to accurately replicate the beam's force-displacement response, achieving a relative error of less than 10% compared to control results. Furthermore, the DT model will demonstrate its predictive capability by accurately estimating the imposed mid-span point loads and maximum strain values along the beam soffit, demonstrating strong correlation with experimental outcomes.

1.3 SCOPE OF THE STUDY

This study serves as a proof-of-concept in demonstrating the feasibility and potential of a practical and cost-effective DT-SHM framework, with the ultimate objective of applying its concepts and methodologies to the monitoring of real-life civil infrastructures. The experimental scope of this research was limited to statically determinate, simply supported RC beams, tested under short-term static three-point bending loads in a controlled laboratory environment. Continuity or statically indeterminate beams were not considered.

The tested RC beams were under-reinforced, specifically designed to induce a ductile flexural failure mode, while adequate stirrups were provided to prevent shear failure. The beams had a shear span-to-depth ratio of 7.8 and were intended to behave as shallow beams. Both elastic and plastic behaviour of the RC beam was studied, encompassing pre-cracking (elastic) and post-cracking (plastic) responses. However, more complex loading conditions, such as dynamic and long-term loading, were not considered.

The calibration and operation of the sensors were conducted without accounting for environmental variables, including variations of temperature and humidity, which can influence sensor performance. The DT developed in this study was specifically designed to replicate the mechanical response of a simply supported RC beam under the given testing conditions.

1.4 METHODOLOGY

The methodology of the experimental study followed a systematic approach with the following key procedures sequentially outlined below:

- Conceptualisation and development of the DT-SHM framework:
  - The framework architecture was conceptualised and designed to numerically replicate the estimated mechanical behaviour of a RC beam, incorporating desired features identified in the literature review. The design criteria for the hardware and software core systems were defined. The core systems serve as vital links between the physical and digital models, allowing synchronised data flow.
  - The hardware system comprising a smart sensor prototype using a potentiometer contact and Infrared (IR) non-contact displacement sensors wired to an Arduino Nano 33 IoT microcontroller, was developed. This involved sensor design, assembly, calibration, software configuration, and implementation. RC beam specimens, experimental loading setup, control result measurement, and material property sampling were planned and prepared.
  - The software system is governed by an automated software program named "ReConTwin". The name "ReConTwin" is derived from the primary Finite Element (FE) analysis software, *ReConAn* (an abbreviation for Reinforced Concrete Analysis), which the developed program uses to create a DT – conveying the notion of extending the analysis software's capability to twin the RC beam it analyses. ReConTwin, developed using Python, includes features such as DT dynamic updates, post-processing, and damage diagnostic functionalities. The DT is intended to closely simulate the force-displacement relationship of the RC beam under three-point bending using a numerical FE model. ReConTwin was also designed to integrate sensor data with the DT for automated FE structural analysis to estimate imposed loads and crack width, predict crack formations, and support damage diagnosis.
- Experimental testing and performance evaluation of the DT-SHM framework:
  - Load Test Stage 1: Four RC beam specimens were tested to obtain mechanical response data for the DT calibration. Strain values along the RC beam soffit mid-span were measured using the control sensors as a comparison benchmark.
  - The calibration process of the DT was conducted through iterative structural analysis of the FE model. The material properties were varied to identify a DT that most resembled the average load-displacement data obtained from Load Test Stage 1.
  - Load Test Stage 2: The final RC beam specimen underwent static-cyclic and static-incremental load tests. The developed DT-SHM framework was applied to monitor the RC beam specimen during the tests. The developed IoT-enhanced smart sensors were introduced during this stage, and their performance against the control sensor results was assessed. The accuracy and reliability of the calibrated

DT in predicting the beam soffit strain, imposed load, and crack formations were investigated. Additionally, the framework's damage prognosis capabilities, facilitated by ReConTwin, were demonstrated.

1.5 ORGANISATION OF THE REPORT

The report consists of the following chapters:

- Chapter 1 serves as an introduction to the dissertation, outlining the objectives, hypothesis, scope, methodology and organisation of this experimental study.
- Chapter 2 contains a literature review examining the principles, components, and current processes in SHM of civil infrastructure. This chapter explores existing and emerging contact and non-contact sensor technologies, as well as IoT wireless communication, and DT methods, providing a broad understanding of evolving SHM practices, their strengths and limitations.
- Chapter 3 presents the detailed development of the proposed DT-SHM framework, a practical and cost-effective health monitoring system designed to digitally twin the mechanical behaviour of a monitored RC beam, with an adequate level of performance in achieving the research objectives.
- Chapter 4 details and discusses the experimental results of RC beam specimens under bending tests, and the calibration outcome of the DT FE model. This chapter evaluates the reliability of the calibrated DT, the accuracy of the displacement sensors, and the overall performance of the framework. It demonstrates the post-processing procedures and the software program, ReConTwin used for model analysis, mechanical response estimation, and damage diagnosis.
- Chapter 5 concludes with a summary of the research objectives and hypothesis outlined in Chapter 1. Recommendations for future improvement and implementation of the framework are discussed.
- References contains a list of the referenced literature discussed in the manuscript.
- Appendix A provides additional information, experimental result graphs and tables, concrete sample preparation and test procedures, electrical circuit configuration, sensor calibration results, ReConTwin user interface development, and IoT cloud configuration information.

2 LITERATURE REVIEW

2.1 INTRODUCTION

The South African civil infrastructure forms part of the country's vital transport system, serving in the transit of both passengers and freight between major cities and ports. Despite its well-established presence in the country and the continuous improvements made by state-owned entity investments, the condition of the civil infrastructure is exhibiting a degrading trend, as indicated in the recent Infrastructure Report Cards published by the South African Institution of Civil Engineering (SAICE, 2017; 2022). The deterioration of the ageing infrastructure has adversely affected its support in the commercial sector and reduced the country's economic competitiveness in the global market (Joynt, 2019). In the face of a substantial rise in traffic volume to compensate for escalating transport demands, the upkeep of the existing infrastructure in the form of condition assessment and maintenance is of utmost importance.

At present, the industry's preferred approach for assessing the structural condition of most civil infrastructure, is solely by visual inspections. Though this method provides the inspectors with a holistic understanding of the structure's ostensible condition and identifies locations of visible distress, it imposes many limitations on the accurate and efficient identification of structural concerns and defects. Agdas *et al*. (2019) state that visual inspections can be subjective and inconsistent due to discrepancies in training and inspection guidelines utilised. Moreover, the nature of visual inspections only offers discrete observations on site at a single point in time and limits the response agility for making informed maintenance and rehabilitation decisions. The greatest drawback of all is the inability to accurately detect internal issues that are neither visible nor discernible from the surface (Graybeal *et al*., 2022). Other inspection techniques include the application of manual, non-destructive tests such as ultrasonic, radiography, and magnetic particles. However, they are inherently costly, labour-intensive, complicated to install, potentially disruptive, and dangerous during their operations (Cawley, 2001; Nagarajaiah & Erazo, 2016; Rehman *et al*., 2015). These drawbacks highlight the need for more innovative, efficient, and timely monitoring approaches to ensure that infrastructure remains sound, to maintain the quality of life, economic growth, and engineering sustainability. A similar view is conveyed in the White Paper of the National Rail Policy (DoT, 2017), whereby the problem statement concludes: "*old solutions have been reapplied and have not enabled rail to rise to the country's transport challenges. Innovative thinking is required to address these issues*".

The ongoing industrial revolution, unfolding since the late 18th century, has progressed through transformative stages and marked pivotal shifts in the advancement of human civilisation (Figure 2-1). In the current era of the Fourth Industrial Revolution, a continuous influx of innovative, smart technologies and data-driven solutions is reshaping conventional paradigms, offering innovative approaches to address longstanding challenges, and redefining user interactions with civil infrastructure (Schwab, 2017). The field of Structural Health Monitoring (SHM) is at the forefront of this transformation, with extensive research and development programs underway to demonstrate its ability to provide stakeholders and engineers with a profound understanding of the condition of their infrastructure assets.

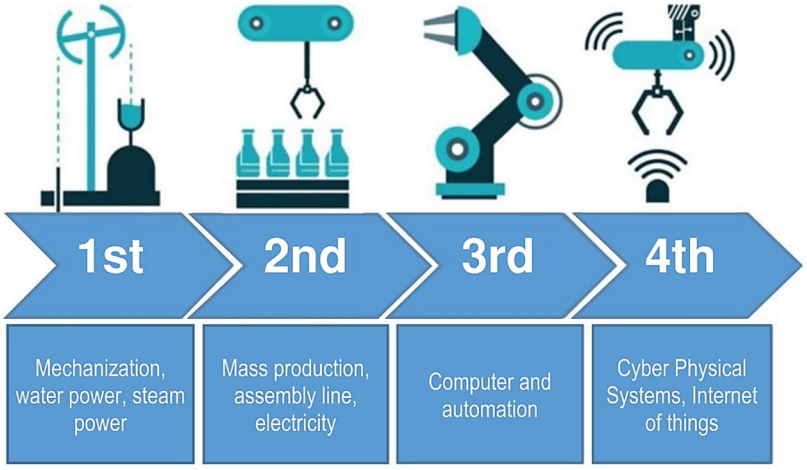

Figure 2-1: Industrial revolution evolution (Sikandar *et al.*, 2021)

The incorporation of sensor systems, the IoT, and advanced data post-processing capabilities has significantly augmented the digitisation of SHM, creating the novel concept of DT. DT enables the creation of a virtual counterpart or replica of a civil infrastructure, such as a bridge, by continuously extracting and processing real-time data from embedded sensors and IoT devices. This digital model provides a dynamic and detailed representation of the current structural condition, facilitates real-time monitoring, analysis, and predictive maintenance through prognostic processes (Errandonea *et al.*, 2020). The incorporation of these technologies not only enhances the accuracy and efficiency of SHM but fosters a paradigm shift towards new possibilities for proactive and data-driven decision-making in the management and maintenance of critical civil infrastructures in the future.

This literature review examines the basic principles, components and current processes involved in SHM of civil infrastructure. A selection of popular and emerging contact and non-contact type sensor technologies designed to measure the physical behaviour of the

structure are explored and discussed. Additionally, IoT capabilities and techniques, including the use of wireless communication and digital twinning, to create a next-generation SHM method are presented. The investigation into these subjects contributes to a broad understanding of the evolving SHM practices, gaining insights into their inherent strengths and limitations.

2.2 STRUCTURAL HEALTH MONITORING

The continual ageing and degradation of civil infrastructure have heightened the owners' and operators' incentive to pursue more precise and efficient methods to assess their structural conditions. Understanding the performance and the degree of deterioration not only equips the owners and operators with the requisite information to make well-informed repair and maintenance decisions, but also offers insights into the remaining service-life and capacity of the infrastructure. SHM is an emerging approach that aims to achieve these goals and is attracting growing research attention and global recognition (Annamdas *et al.*, 2017; Karbhari & Ansari, 2009).

The main objective of SHM is to continuously monitor and evaluate the structural condition to identify, diagnose, and detect damages without excessive human intervention. Boller *et al*. (2009) classify the level of knowledge of the structure's damage state based on the sophistication of the SHM system (Figure 2-2).

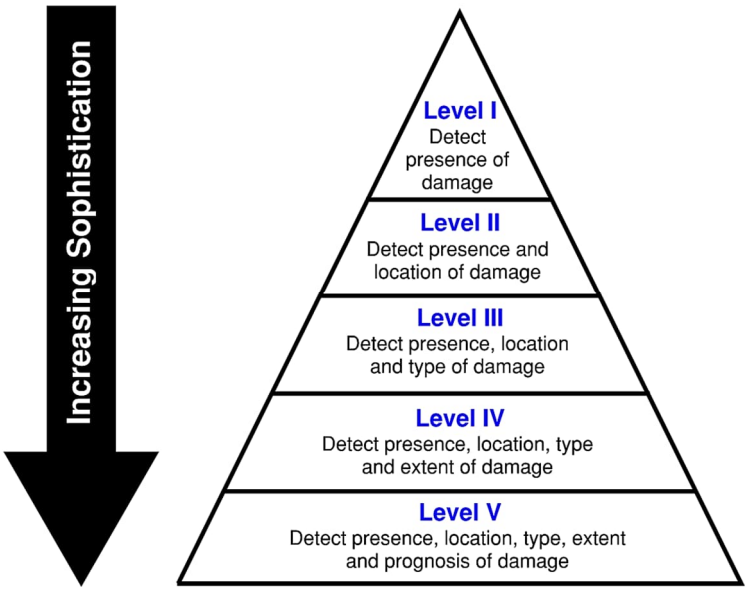

Figure 2-2: Relationship between the sophistication of an SHM system and the level of understanding of the damage state (Boller *et al.*, 2009)

The hierarchy of levels is outlined by a progressive understanding of the damage state of the monitored structure, with each level building upon the knowledge acquired from preceding levels. From the basic detection and localisation of damage, the system advances to acquire more complex capabilities of damage type classification and its extent estimation. Ultimately, at the most sophisticated level, the system can perform damage prognosis, which provides information pertaining to the safety of structure usage. This is typically achieved by estimating the structure's remaining future performance through analytical predictive modelling.

Sun *et al*. (2010) identified that a SHM system generally consists of the following three primary components:

- Sensor technology
- Data processing system
- Health evaluation (post-processing) system

Hassani & Dackermann (2023) describe that these components form part of the two primary groups of a SHM system, namely the sensing, and data processing and analysis groups (Figure 2-3).

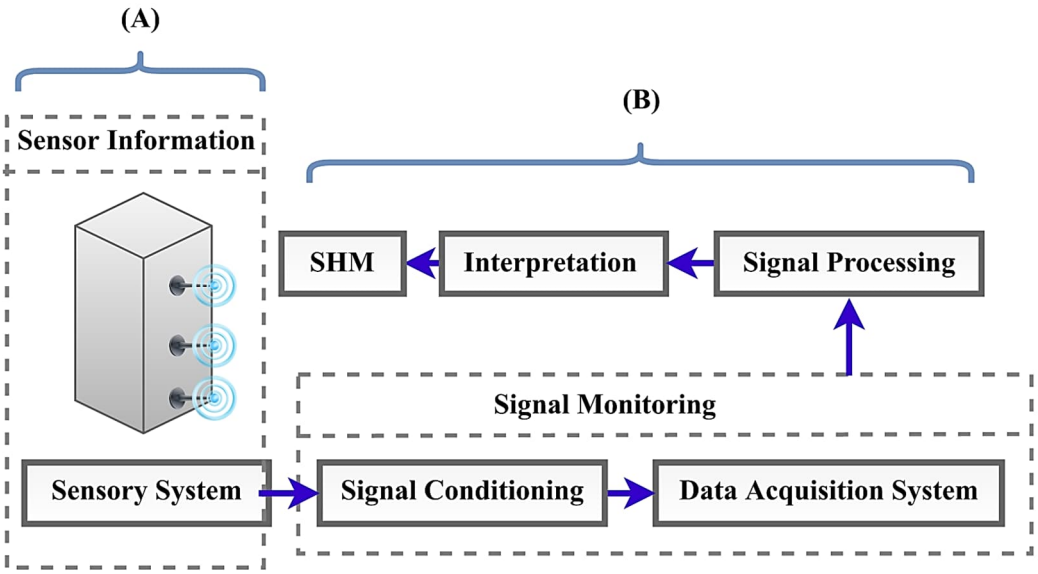

Figure 2-3: Two primary groups of a typical SHM system: (A) sensing group, and (B) data processing and analysis group (Hassani & Dackermann, 2023)

Sensor technologies are critical to Levels I, II, and III SHM systems, gathering crucial monitoring parameters essential for assessing the structural condition. Equally important at these levels is a robust data processing system, which enables autonomous, real-time

monitoring. Raw data collected is required to be efficiently transferred, stored, and processed to provide readily accessible and meaningful information to the user. In recent years, the processing of data has been improved through the integration of wireless communication and IoT technologies. Levels IV and V prioritise health evaluations, where filtered and evaluated data is post-processed using novel analytical and numerical methodologies to forecast deterioration. Subsequently, an interactive system is generated to offer proactive recommendations based on the health assessment. A sophisticated SHM system has the capability to continuously detect and monitor damages of structural assets in real-time and online, enabling optimal maintenance of structures to ensure their safety and longevity.

2.3 CONTACT TYPE SENSORS

Sensors are a critical component of SHM. They serve as highly automated data acquisition tools, capturing real-time data pertaining to the behaviour and responses of instrumented civil infrastructure, minimising human intervention. They are progressively evolving to operate with greater efficiency while becoming more cost-effective. Amongst sensor types, contact sensors are fundamental and widely used, requiring physical contact with the structure being monitored. In this section, popular contact sensor technologies dedicated to quantifying the physical behaviour of structural components are identified and discussed.

2.3.1 LVDT Sensors

A Linear Variable Differential Transducer (LVDT) is a type of electromechanical passive device that converts linear displacement of a connected moving object into a corresponding electrical signal (Wu *et al.*, 2008). It operates on the principle of electromagnetic induction, where the variation in voltage between the primary and secondary coupled coils, caused by the change in core position, is used to determine displacement, as shown in Figure 2-4. The measured displacement can then be quantified by proportioning the change in output voltage (Joshi & Harle, 2017). LVDT sensors are highly precise, stable, and durable in the continuous measurements of structural deformations, making them valuable and popular for the physical monitoring of displacements and vibrations in various civil infrastructure.

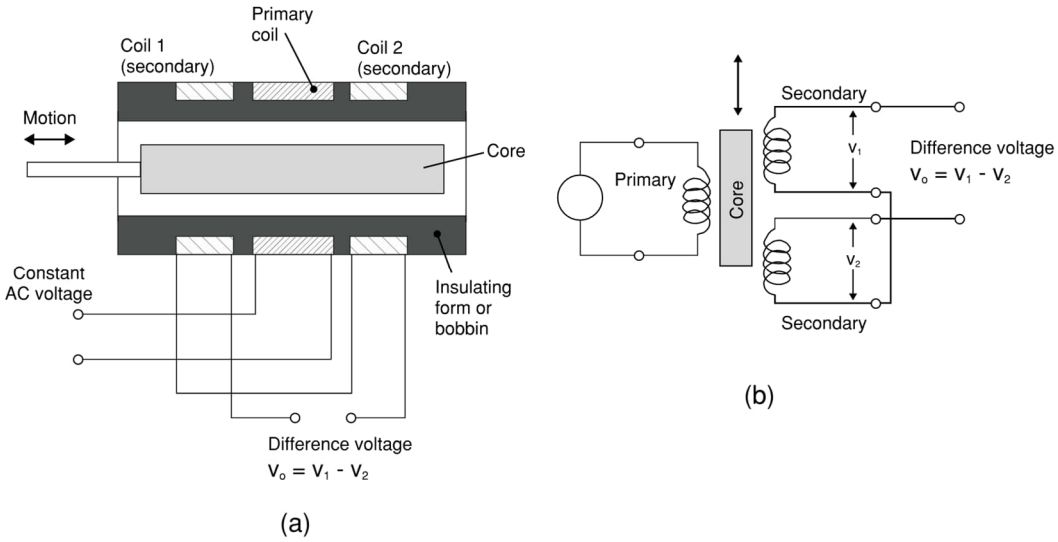

Figure 2-4: Working principle of a LVDT: (a) Cross section view of its construction, and (b) Equivalent circuit diagram (Joshi & Harle, 2017)

Nhung *et al*. (2023) investigated the use of LVDT sensors to continuously monitor the displacement of an in-service railway bridge. The measured field data, in conjunction with FE modelling, enabled the development and implementation of LVDT sensors in the SHM of urban railway bridges. A research study performed by Mayunga & Bakaone (2021) incorporated Global Positioning System (GPS) and LVDT technologies to monitor the deformation of the Lotsane Bridge in Botswana. The obtained GPS measurements was used to establish the horizontal positions of the reference and monitoring points, while employing the LVDT to measure vertical deflections to quantify accelerations, and strains. The authors concluded that the proposed monitoring system could provide valuable data on the structural integrity of the bridge and serve as an indicator of the bridge's performance.

Wang & Yim (2010) realised a SHM system on the Kishwaukee Bridge in the USA, utilising strategically installed LVDT sensors along both the internal and external surfaces of the box-girder deck depicted in Figure 2-5. The automated monitoring system facilitated the collection of shear crack displacements at the measured locations, enabling analysis to determine possible yielding of the embedded shear reinforcement. Subsequently, the system could estimate the shear stiffness of the bridge deck web. This information proved valuable to formulate retrofitting strategies for the compromised components.

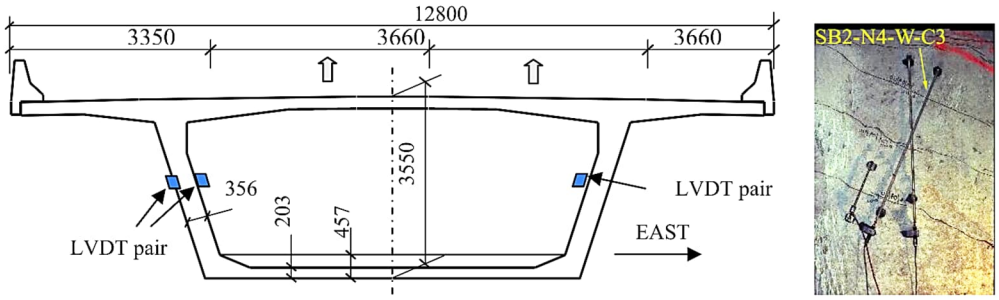

Figure 2-5: Installation location of LVDT sensors on Kishwaukee Bridge (dimension units: mm) (Wang & Yim, 2010)

LVDT sensors are characterised by high accuracy, precision, and long-term reliability, making them ideal for monitoring small displacements and vibrations in civil structures. Nevertheless, their performance may be affected by environmental factors including temperature variations and magnetic field interferences. Moreover, the on-site installation of the LVDT can be cumbersome and challenging (Ma *et al*., 2023). Despite these limitations, LVDT sensors remain indispensable for SHM in civil infrastructures and are often regarded as the control sensor, especially when precision and reliability are paramount.

2.3.2 Piezoelectric Sensors

Piezoelectric sensors utilise the piezoelectric effect to detect mechanical changes such as displacement, force, temperature, and acceleration. This effect relies on materials such as quartz, ceramics, or synthetic crystals composed of a crystalline structure with an asymmetrical charge distribution. When subjected to external forces, these materials undergo minor deformations, resulting in the separation of positive and negative charges across the material, creating a potential difference in the connected electrical circuit (Rupitsch, 2019). The flow of electrons in the circuit generates a measurable electric signal which is processed for interpretation of the magnitude, duration, and even the direction of the exerted mechanical impedance (Figure 2-6). The monitoring method described above is commonly known as the electromechanical impedance-based sensing method.

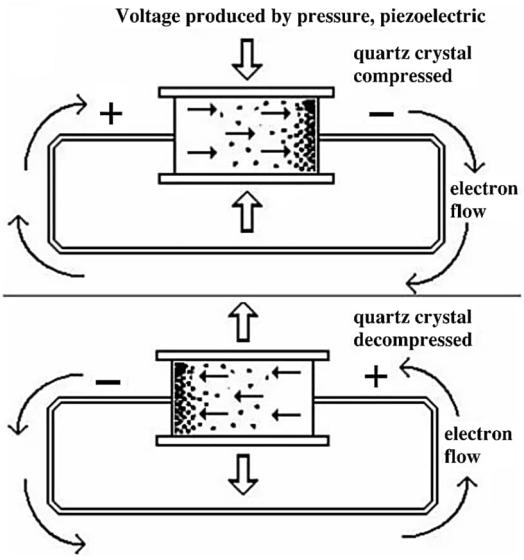

Figure 2-6: Potential difference in an electric circuit caused by mechanical impedance on the piezoelectric material (Elfick, 2024)

Due to the materials' unique electro-mechanical properties, piezo-electric material can function both as an actuator and a sensor due to its unique electro-mechanical properties. This characteristic has paved the way in the introduction of two main SHM methods in recent years of development (Ju *et al*., 2023), namely the Electro-Mechanical Impedance (EMI) method, and the guided wave or ultrasonic propagation method.

In an earlier experimental study of the EMI method, Tseng *et al*. (2000) conducted destructive load tests on a RC bridge model instrumented with piezoceramic sensors at strategic points of likely crack formation (Figure 2-7). The sensors were scanned for the acquisition of electrical frequency signatures at various load stages, and successfully quantified the tensile cracks in non-parametric terms.

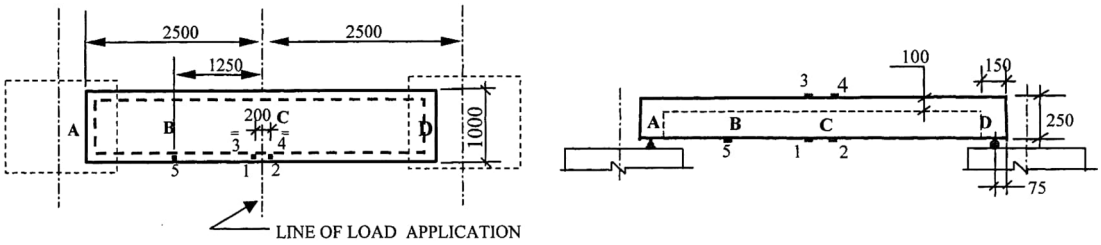

Figure 2-7: Piezoceramic sensor locations installed on the RC bridge model (Tseng *et al*., 2000)

Voutetaki *et al*. (2022) performed an experimental investigation by applying a repeated compressive load on a 150 mm fibre-reinforced concrete cube with a network of surface-mounted piezoelectric transducers. The sensors were designed to possess a dual-sensing functionality whereby the monitoring system vibrates them as actuators, and simultaneously monitors their signal output as sensors. The study found that the custom-made electro-mechanical admittance-based SHM system could identify cracking damage in fibre-reinforced concrete cubes containing synthetic fibres. Song *et al*. (2017) developed an aggregate-shaped piezoelectric sensor which was embedded within the structural body during construction. Test results showed that the embedded sensors exhibit excellent mechanical-electrical coupling performance.

SHM utilising the guided wave or ultrasonic propagation method has been widely applied in detecting damage in composite and metallic structures. Due to their strength in having a longer surface propagation range and minimal energy loss, they are better suited for performing global monitoring than the EMI method. Four main propagating operational techniques using guided waves are illustrated by Giurgiutiu & Soutis (2012) in Figure 2-8.

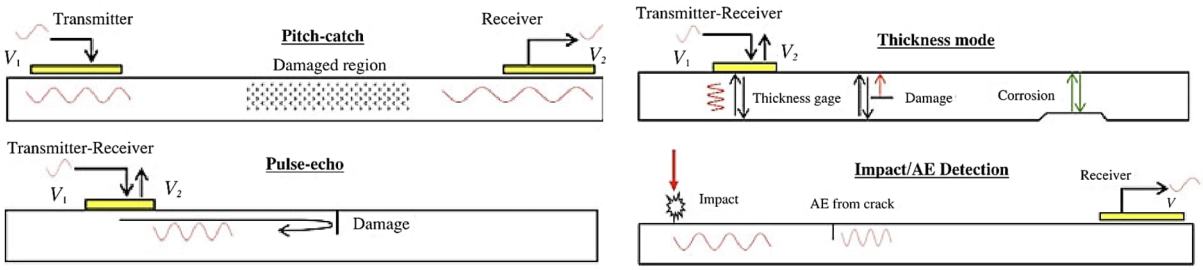

Figure 2-8: Operational techniques of piezoelectric sensors using guided Lamb waves (Giurgiutiu & Soutis, 2012)

Kee & Zhu (2013) studied the feasibility of using an ultrasonic-based SHM method by embedding two piezoelectric sensors in a RC specimen. Through a series of ultrasonic tests on the specimen under various external loadings, the measured sensor signal exhibited a broad bandwidth and good coherence in an adequate frequency range. Research conducted by Yu *et al*. (2008) investigated the use of piezoelectric wafer active sensors in SHM and found the Lamb-wave methods are suitable in detecting cracks and corrosion in metallic structures. Liu *et al*. (2020) developed an embedded piezoelectric ultrasonic transducer for monitoring crack and corrosion damages in steel bars. The study concluded that the proposed piezoelectric

transducer efficiently monitored different types of damage in steel bars, proving its potential contribution for SHM applications.

The EMI method of SHM utilising piezoelectric sensors offers a convenient, qualitative approach, as the output result can be easily interpreted without specialised knowledge. While this method excels at detecting local damage where the sensor is installed, its qualitative nature poses challenges in differentiating other damage characteristics, such as steel corrosion and delamination. Consequently, when an EMI sensor detects damage, additional assessments are necessary for precise damage characterisation. Future research calls for more efficient methods to directly determine the nature of the damage and its magnitude from the sensor data. Conversely, the SHM based on guided wave and ultrasonic propagation methods intrinsically covers larger detecting areas. These methods leverage various wave propagation characteristics, including amplitudes, time of arrival, phase, and frequency shifts, to identify structural damages. Most existing research and experimental work on SHM using piezoelectric sensors have focused on small-scale or structural-scale models. Further research is necessary to effectively integrate these sensors with wireless communication technologies to realise their full potential in real-world infrastructure monitoring (Chen & Xue, 2018).

2.3.3 Potentiometer and Extensometer Sensors

Potentiometer and extensometer sensors are widely used sensors in SHM to measure displacements and deformations in civil infrastructure. Potentiometer measure displacement by converting linear or angular motion into a change in electrical resistance, making them cost-effective and simple solutions for displacement measurement. Extensometers are commonly designed to measure strain or displacement directly within materials or structures. Both sensors have been extensively applied in geotechnical monitoring, bridge assessments and structural analysis.

de Battista *et al*. (2014) installed a pull-wire extensometer equipped with a potentiometer at the deck expansion joint of the Tamar Suspension Bridge to measure longitudinal deck extensions caused by thermal effects. The potentiometer enabled precise tracking of deck movement in response to temperature variation, demonstrating the effectiveness of the potentiometer-based system in monitoring thermal-induced bridge deformations. Guerriero *et al*. (2017) developed an Arduino-based extensometer as a low-cost and adaptable solution for continuous landslide monitoring. The system is equipped with a high-precision position transducer (measuring range of 1023 mm, accuracy of ±1 mm), demonstrated high measurement reliability and monitoring stability in field tests. In France, extensometers are equipped on the raft foundations of nuclear

power plant reactor buildings to monitor long-term structural behaviour. The data collected from these devices were used by Pineau *et al*. (2024) to analyse curvature, deflections, and settlements over the building's lifespan. Their findings provided insights into the raft's mechanical response, allowing for comparisons with design predictions and contributing to the optimisation of future nuclear power plant foundation designs on soft soils.

Linear potentiometers and extensometers are widely utilised in displacement and strain measurement applications. Linear potentiometers offer high accuracy, repeatability, and cost-effectiveness, making them ideal for various position-sensing applications (ETI Systems, 2025). However, they are susceptible to wear and tear over long-term use due to the mechanical contact between the wiper and resistive element, and their exposure to dust and other contaminants can degrade performance, necessitating protective measures in certain environments. Extensometers are commonly employed for precise strain measurement in material testing, providing reliable data on material deformation across various materials, including metals, plastics, and composites (McEnteggart, 2008). Despite their accuracy, extensometers may introduce setup complexity and often require a higher investment cost (Pan & Tian, 2016).

2.3.4 Fibre Optic Sensors

In recent decades, Fibre Optic (FO) sensing technology has not only become a trending alternative to traditional electrical sensors in the telecommunication industry, but is emerging as an innovative tool in structural monitoring of critical civil infrastructure. Due to their characteristic strengths of durability, performance consistency, compact size, and insensitivity to electromagnetic disturbances, FO technology has found promising significance in SHM of civil structures (Lopez-Higuera *et al*., 2011).

The basic principle of a FO sensor involves an interrogator emitting light within the core of an optical fibre, as shown in Figure 2-9. In its simplest form, an optical fibre is a cylindrical tube consisting of a glass or plastic core with a uniform refractive index and a diameter ranging between 4 μm and 600 μm (Gupta, 2006). Surrounding the core is a cladding material that shields the core from external mechanical and environmental effects. The cladding material possesses a lower refractive index medium than that of the core's medium, allowing the light signal to transmit effectively along the length of the fibre by refracting between the cladding interfaces. As the interrogator continuously injects light into one end of the fibre, external factors such as displacement and temperature changes in the monitoring structure alters the wavelength of the reflected light. This variation is detected and converted into engineering units

such as strain, vibrational amplitude, and temperature variation, providing valuable information about the conditions of the surrounding environment and structure.

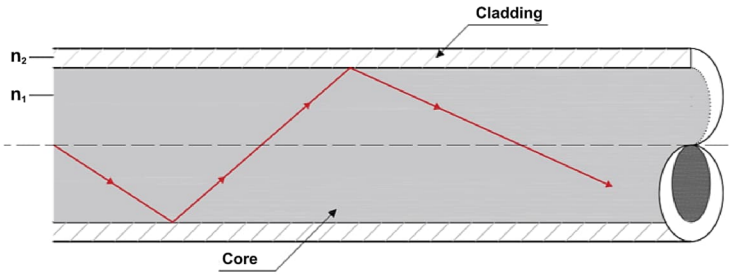

Figure 2-9: Cross section side view of an optical fibre and refraction of propagated ray within the core (Barrias *et al.*, 2016)

FO sensors are constantly evolving with ongoing research and development efforts in their application for the SHM of civil infrastructure. Outlined by Wu *et al.* (2020), they can be commonly classified based on the following key criterion:

- Light operating principles – modulated by light intensity, phase, polarisation state, wavelength, or frequency changes
- Sensing mechanisms – modulation occurring within the optical fibre as the light travels from the source to the detector is termed an intrinsic sensing type (if it occurs externally, it is referred to as an extrinsic sensing type)
- Sensing range along the fibre length – point type (a specific point), quasi-distributed type (several points), and distributed type (continuous measurements along a length)

Numerous laboratory experimental works carried out by many researchers have demonstrated the FO sensors' promising potential in SHM of various RC elements. Berrocal *et al.* (2021) explored the efficacy of embedded Distributed Optical Fibre Sensor (DOFS) cables with a durable external polyamide coating in accurately evaluating the mechanical response of three RC beams. The DOFS were strategically affixed to the reinforcement bars with a multi-layer configuration, installed along the longitudinal bars, spanning between the stirrups, and onto the formwork (Figure 2-10). The outcome of the four-point bending tests successfully yielded a reliable estimation of beam deflection, with errors ranging from 6.5% to 12.3%. Additionally, strain measurements exhibited minimal variation with deviations as small as 20 μm compared to the control results.

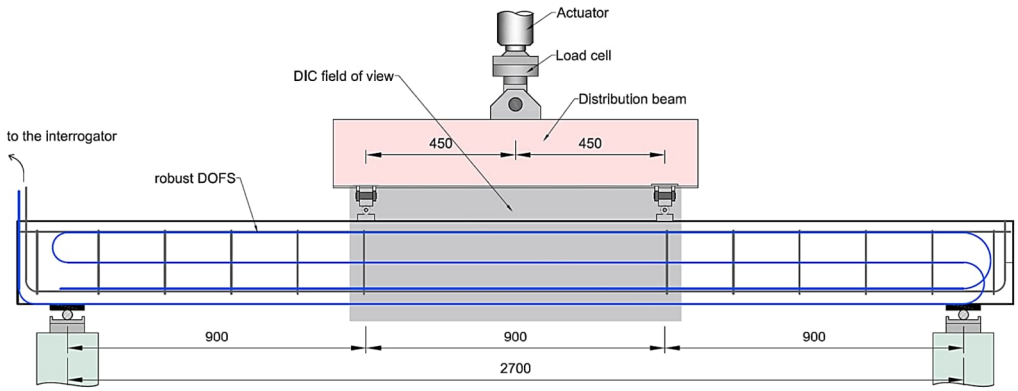

Figure 2-10: Embedded DOFS installed within the RC beam samples with multi-layer configuration (Berrocal *et al.*, 2021)

The configuration of the DOFS also allows the generation of a contour plot of crack patterns by superimposing and interpolating between the cracking profiles along their respective heights along the beam depth, as illustrated in Figure 2-11.

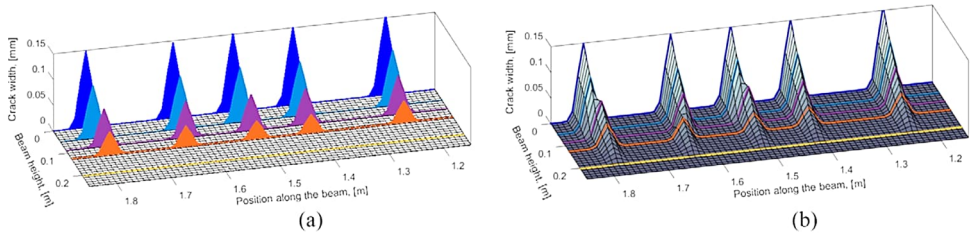

Figure 2-11: Contour plot of crack patterns: (a) superposition of crack functions onto a grid mesh of beam surface location, and (b) generation of crack width profile by interpolating between the crack functions (Berrocal *et al.*, 2021)

Nurmi *et al*. (2019) conducted a study by measuring the distributed strain profile of DOFS instrumented on two-way RC slabs with varying reinforcing ratios and axial restraint levels subjected to a central point load. The measured strain data allowed the identification of changes in support conditions and accurately captured the reinforcement yielding mechanics. The feasibility and effectiveness of DOFS in SHM of actual civil infrastructure have been substantiated through numerous successful case studies in the past. Ye *et al*. (2020) evaluated prestress loss in four prestressed concrete beams of a newly constructed railway bridge in Staffordshire, UK. They deployed both distributed and discrete FO sensors to monitor immediate and time-dependent prestress losses during beam manufacturing (Figure 2-12). The

extracted prestress loss measurements enabled a comparison with the design code calculation methods, assisting in revealing an underestimation.

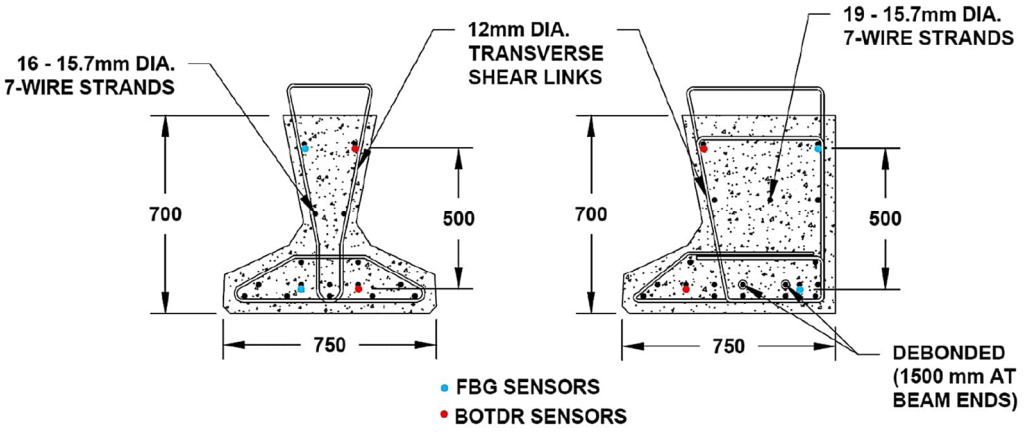

Figure 2-12: Cross sectional view of prestressed concrete beam with distributed (BOTDR) and discrete (FBG) FO sensors (Ye *et al*., 2020)

Using a similar approach, Webb *et al*. (2017) monitored the long-term structural behaviour of a three-span pre-tensioned prestressed concrete bridge located in Cambridge, UK. FO cables were instrumented in six beams, allowing for accurate strain calculation by removing temperature effects on the Brillouin frequency shift. By comparing the in-situ measurements with empirical creep and shrinkage models, good correlations between the measured strains and the design code methods were identified. FO sensing techniques were also employed and proved viable in SHM of structural steel bridges by many studies, such as Matta *et al*. (2008).

Fiber Bragg Gratings (FBGs) are optical sensors that function by reflecting specific wavelengths of light while transmitting others, creating a periodic variation in the refractive index along the FO core. When subjected to strain or temperature changes, the reflected wavelength shifts, enabling precise measurements of these parameters. In SHM, FBGs are employed to detect deformations, stresses, and other structural changes. Unlike DOFSs, which provide continuous monitoring along the entire length of the fibre, FBGs offer discrete sensing points, allowing for targeted measurements at specific locations within a structure.

Several researchers have successfully integrated FBGs into SHM applications. Zhang *et al*. (2020) proposed the incorporation of FBG sensors into aluminium alloy structures to monitor crack growth, demonstrating the effectiveness of FBGs in detecting early-stage structural failures. Kinet *et al*. (2014) focused on embedded FBGs into composite materials,

addressing challenges related to temperature-strain discrimination and sensor integration, thereby enhancing the reliability of SHM in composite structures. Wu *et al*. (2018) conducted an experimental study demonstrating the use of FBGs in ultrasonic SHM, showcasing their capability in detecting high-frequency stress waves within structural materials.

The advantages of FBGs in SHM include high sensitivity, immunity to electromagnetic interference, and the ability to multiplex multiple sensors along a single fibre, facilitating comprehensive monitoring of large structures. However, challenges such as the need for precise calibration, potential signal loss over long distances, and sensitivity to environmental factors such as temperature variations can impact their performance (Majumder *et al*., 2008). Despite these drawbacks, the numerous benefits of FBGs make them a highly valuable tool in the SHM applications.

In comparison to conventional electrical sensors, FO sensors are light, non-conductive, electrically passive, and immune to electromagnetic interference, making them a safe and reliable alternative in environments subject to noise, corrosion, or high voltage. However, they also inherently possess a few notable disadvantages. FO sensors are comparatively more costly than traditional electrical sensors (Sabri *et al*., 2013). This is primarily due to the need for specialised equipment and skilled personnel for its implementation and maintenance. Additionally, once embedded within a RC element, FO sensors become irreplaceable without resorting to destructive means. Even when installed along the external perimeter of the structure, it necessitates laborious inspections of bond quality. Furthermore, the complexity involved in designing, installing, and calibrating FO sensor systems demands specialised knowledge and expertise in signal processing and optical engineering.

2.4 NON-CONTACT TYPE SENSORS

Since their inception in the mid-twentieth century, non-contact sensors and methods were initially developed for scientific and industrial applications. Over time, these sensors have undergone progressive improvements and are regarded as next-generation measurement technologies in the field of SHM of civil infrastructure. In contrast to conventional contact sensors, non-contact sensors can operate without requiring direct physical contact or attachment to the surface of the structural element being monitored (Sony *et al*., 2019). They offer a non-invasive solution for inspection and data acquisition, eliminating the need for direct physical intervention and ensuring a safe and time-efficient monitoring process. In this section, emerging contactless sensor technologies and methods in measuring the physical changes relating to displacements and deformations of the structure are identified and discussed.

2.4.1 LiDAR Sensors

In the last decade, Light Detection and Ranging (LiDAR) sensing technology has witnessed widespread adoption across various SHM applications. Ongoing advancements in design have made LiDAR sensors increasingly sophisticated while simultaneously reducing their cost, size, weight, and power consumption (Raj *et al*., 2020). LiDAR devices are generally categorised according to their ability to gather different types of information relating to spatial and spectral aspects. Spatial data, typically generated by using laser pulsing technologies to determine distances to object surfaces, can perform precise three-dimensional (3D) mapping. Alongside spatial data, LiDAR instruments can also record spectral information, such as material identity, by applying laser return intensity methods. These features empower the LiDAR sensors to play a significant role in civil infrastructure monitoring with the following capabilities: 3D model generation, damage detection, structural assessment, and integration in digital information modelling (Rashidi *et al*., 2020).

Cha *et al*. (2019) explored the feasibility of using terrestrial LiDAR for constructing building information models and monitoring deformation in bridge structures. This was achieved by obtaining 3D position information through terrestrial laser scanning and implementing an octree data structure for efficient data processing. Laser scanning was initially conducted on two steel bridges to generate a compressed and calibrated shape information model. This model was then utilised to estimate deflection in another steel box-girder bridge in service, showing promising results comparable to LVDT measurements. Erdélyi *et al*. (2020) investigated deformation response in bridge monitoring using terrestrial laser scanning and ground-based radar interferometry. The study concluded that both methods were highly effective for deformation analysis, with laser scanners providing millimetre-level accuracy, which can be further improved through advanced data processing. By computing the image orthorectification, the precision of the deformation measurements was significantly enhanced.

Apart from structural deformation detection, researchers have also applied the terrestrial LiDAR technology to identify damages. Valença *et al*. (2017) introduced a novel method named MCrack-TLS for automated crack assessment in concrete bridges by combining image processing and terrestrial laser scanning. By orthorectifying images with terrestrial data, the method overcomes challenges in applying image processing to large structures. Experimented on a concrete viaduct, the method demonstrated high potential for increased productivity and safety while enabling the creation of detailed 3D models of bridge conditions and record-keeping capabilities (Figure 2-13).

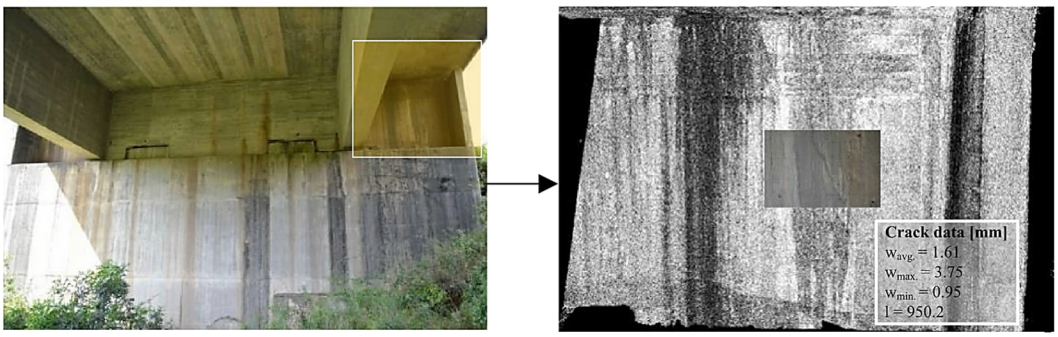

(a) (b)

Figure 2-13: Terrestrial laser scanning and image processing for crack identification: (a) Identified crack area, and (b) 3D model of identified crack area (Valença *et al.*, 2017)

The most valuable benefit of LiDAR sensors is their independence from physical instrumentation and direct access to structures. This characteristic significantly reduces time and labour costs while enhancing workplace safety. Moreover, LiDAR sensors can operate without the need for natural light sources, making them valuable tools for field measurements. Despite these advantages, they are not without limitations. As highlighted by Kaartinen *et al*. (2022), their shortcomings include:

- Operability is highly dependent on the weather conditions, and performance diminishes with increased distance from the monitored structure. Additionally, strategic positioning is essential to prevent overlapping or targetless scans, with the sensor's field of view playing a crucial role in what is captured.
- The cost of the LiDAR sensor and associated equipment is high.
- Due to the necessity for multiple scans at different locations and the need to filter out non-structural elements, data processing techniques for extracting objects and interpolation can be complex and time-consuming.
- LiDAR sensors only inspect and allocate defects found on the surface of the structure, limiting their ability to detect subsurface issues.

2.4.2 Vision-Based Sensors

With the rapid advancements of digital cameras and computers, vision-based sensors are increasingly incorporated into the contactless approach of SHM (Feng & Feng, 2018). These sensors employ photogrammetry techniques to capture images and videos, determining attributes of a monitored structural object, such as position, geometry, and surficial features. A notable distinction from traditional image inspection systems is their integration of camera,

controller, and light source into a single component, streamlining both installation and operation processes. This integration offers several advantages, including ease of use, versatile application, and the elimination of the need for physical contact or extensive wired networks.

A non-contact dynamic displacement measurement system for a railway bridge using video technology was presented by Ribeiro *et al*. (2014). The system employs a high-speed camera, which was successfully tested to accurately measure displacement induced by a passing train. Digital Image Correlation (DIC) is an innovative technique that constructs comprehensive deformation data by comparing captured digital images of an object undergoing deformation (McCormick & Lord, 2010). Numerous research studies, including those by Nonis *et al*. (2013) and Reagan *et al*. (2017), have shown that DIC can be effectively applied in SHM of bridges for identifying crack deformations and accurately quantifying displacement responses.

Kim *et al*. (2018) utilised Unmanned Aerial Vehicles (UAV) equipped with deep learning algorithms for crack identification on concrete bridges, as shown in Figure 2-14. Supported by a 3D point cloud-based background model, the system is trained with a combination of pre-existing datasets and collected crack images to identify cracks and automatically visualise them on inspection maps. The field tests validated the effectiveness of this technique, proving UAV-based vision bridge inspection methods to be a promising strategy for crack detection.

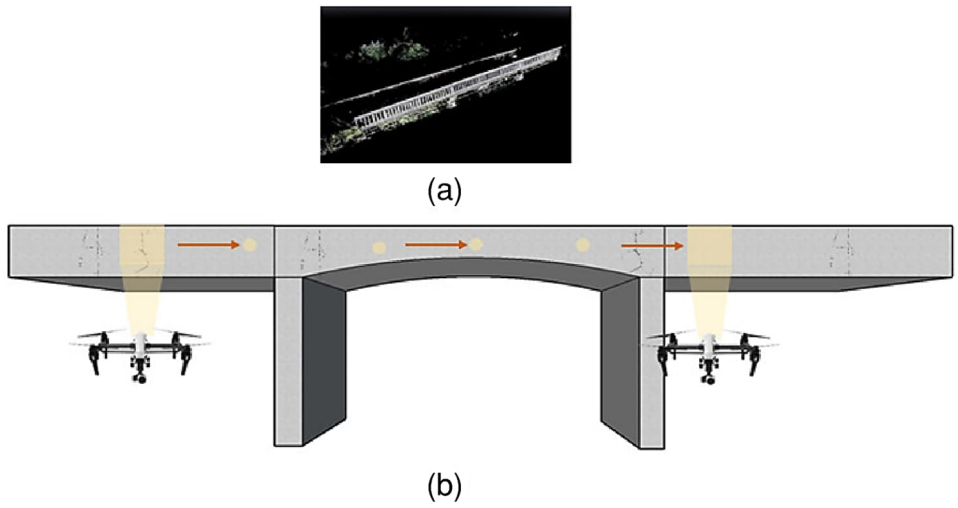

Figure 2-14: UAV-based SHM method in crack detection: (a) Background model generation, and (b) Scanning of an existing bridge structure (Kim *et al*., 2018)

Vision-based sensors have numerous advantages in SHM and are widely regarded by researchers as the most effective and versatile non-contact sensing technique. Although they represent a notable technological advancement, they also present certain drawbacks that offer

opportunities for further research and improvements. For instance, inadequate lighting conditions in the field can compromise measurement accuracy (Amezquita-Sanchez *et al.*, 2018). Additionally, vision-based methods primarily perform surface inspections, limiting their ability to identify subsurface structural defects. The computational demands of DIC can be substantial, driven by the processing of extensive image data. Processes such as feature extraction, correlation analysis, and iterative optimisation necessitate sophisticated algorithms and specialised methods. When assessing vibration in structures through image-based methods, reliance on these advanced post-processing approaches is crucial and cannot depend on the vision-based sensors alone.

2.4.3 Radar Sensor

A radar, an acronym for Radio Detection and Ranging, is a sophisticated electrical sensor device invented not only to detect targets and determine range, but also to assess the distance, velocity, and direction of objects by emitting radio waves and analysing their reflections (Richards *et al*., 2010). Radar sensors are classified based on the two main working mechanisms: the pulse radar and continuous wave radar. The pulse radar operates by emitting short pulses of radio waves and receiving echoes reflected from objects, while the continuous wave radar emits an uninterrupted signal and relies on the Doppler effect to measure frequency changes of the reflected signal. These characteristics have been utilised by many researchers for estimating the displacements of structural buildings and bridges. Earlier studies using radar sensors in the laboratory environment were conducted by many researchers, including Guan *et al*. (2014) and Gentile & Bernardini (2008). They introduced continuous wave radar sensing methods by transmitting low-frequency wave signals to the target objects attached to the structural samples. The reflected and processed radar signal were used to determine the displacement of the monitored target points on the structural model.

This sensor technology has also been extensively experimented on real structural bridges. Zhang *et al.* (2020) developed a ground-based interferometric radar system utilising the continuous wave sensing method to measure the displacements of a 1200 m long suspension bridge. Good agreements were found between the results from the radar system and those from the control systems on site, demonstrating the effectiveness of using this type of sensor. Guan *et al*. (2018) introduced a novel concept by merging continuous wave radar sensors with a wireless sensor to develop a Wise-Radar system for measuring the structural deflections of a full-scale bridge. The measurement results validated the efficacy of the radar-integrated monitoring system as a promising technology for wirelessly measuring both static and dynamic

responses of the bridge with sub-millimetre accuracy. In contrast to most conventional approaches where ground-mounted radar sensors target reference points on the bridge, as depicted in Figure 2-15a, the radar sensor in this study is mounted beneath the moving bridge deck, as shown in Figure 2-15b.

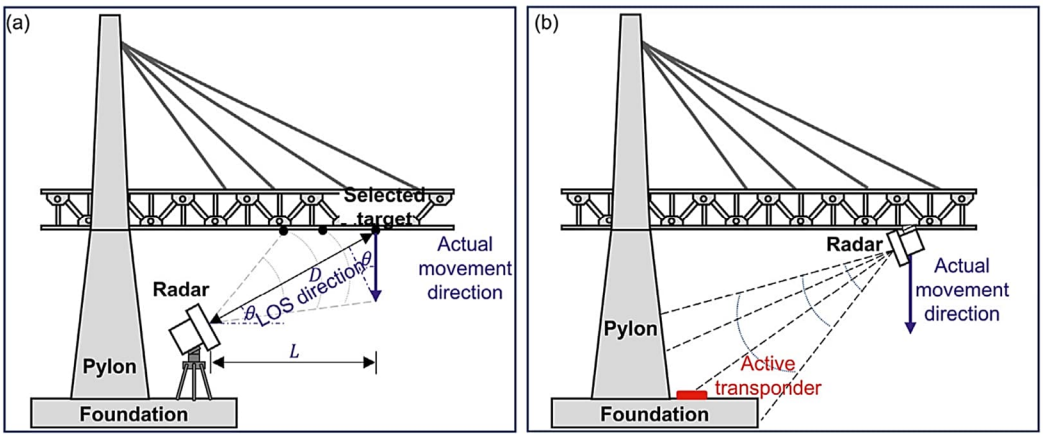

Figure 2-15: Radar sensor setup on structural bridge: (a) Radar sensor mounted on ground monitoring the moving target on bridge, and (b) Radar sensor mounted on the moving bridge monitoring the fixed ground target (Ma *et al.*, 2023)

Continuous wave radar sensors are low-cost, stable, robust, and uncomplicated to use. The sensing system is easily modulated and inherently has low transmitting power, broad bandwidth, high resolution, and simplicity in signal processing (Zhang *et al.*, 2020). They are also suitable for integration with wireless sensor networks due to their affordability and compact size (Guan *et al.*, 2014). However, these sensors have limitations. As highlighted by Ma *et al.* (2023), structural displacements exceeding the radar wavelength can lead to phase wrapping issues, especially in millimetre-wave radar sensors. Additionally, identifying reference targets near desired displacement measurement locations is a manual process, which can be cumbersome. Furthermore, mounting the radar sensor either on the ground or on the monitoring structure may not always be practical in real-world applications.

2.5 WIRELESS COMMUNICATION SENSORS

In any SHM system with contact or non-contact sensors, the collected sensor data must be transmitted and stored for further processing. Traditionally, wired sensor networks have been employed to transfer acquired data via wired lines, such as electrical cabling. While these networks offer stable power supply and reliable data transmission, their real-world

implementation can be challenging. Longer cable lengths can lead to a higher noise level, susceptible to environmental factors, and unforeseen site conditions. Additionally, their installation can be labour-intensive (Mustapha *et al*., 2021). Consequently, wireless communication technologies have emerged and received increasing attention for addressing these issues.

Wireless sensors enhance data transmission by enabling wireless communication between on-site sensors and central data collection systems, eliminating the need for physical network connections. Advances in Micro-Electro-Mechanical Systems (MEMS) have allowed wireless sensors to become miniaturised while operating with greater efficiency and cost-effectiveness. Their performance is mainly dependent on the following aspects: sampling frequency, power consumption, wireless signal range, and Analog-to-Digital Converter (ADC) capabilities. These sensors also leverage a wide range of communication protocols, such as IEEE 802.11 (commonly known as Wi-Fi), IEEE 802.15.4 (used by ZigBee and ISA 100), Bluetooth, and LoRaWAN (Long Range Wide Area Network) technology, which offers long-range communication with lower power consumption.

A notable validation study conducted by Lynch (2007) involved implementing a wireless SHM system on an operational bridge. Through forced vibration testing, the accuracy and reliability of wireless communication amongst sensing units and the user were demonstrated. Spencer *et al.* (2017) developed a wireless smart sensor platform dedicated to transmitting multi-scale sensor data on several sensing parameters. The hardware module incorporated a highly precise ADC with eight channel inputs and a power-optimised communication system with a signal range reaching up to 1 km. Hung *et al.* (2019) created an intelligent, energy-efficient wireless sensing network utilised in SHM for an early earthquake warning system. This technology can enable non-active sensors to operate in low-power modes while being capable of quickly awakening them when motion is detected. Many researchers have highlighted the persistent challenge of power consumption and advocate for further investigation into the prolonged field deployment.

The integration of wireless technology has transitioned conventional wired SHM methods to IoT-based SHM methods. This shift allows real-time data storage and accessibility on cloud-based systems, transforming them into next-generation wireless smart sensors.

2.6 SHM POST-PROCESSING

Post-processing of the obtained sensor data is a fundamental feature of any SHM system for evaluating the health status of monitored civil infrastructure. This process involves two main functions: data evaluation and damage prognosis. Data evaluation focuses on extracting critical information necessary for damage diagnosis, while damage prognosis entails interpreting the data to detect damages and formulating informed decisions on the operation and maintenance of infrastructure assets.

2.6.1 Data Evaluation

The complexity of data processing in SHM is directly influenced by the type of loading and environmental factors affecting the monitored structure. In controlled laboratory settings, where the experimental conditions can be precisely regulated, the generated noise is typically easier to process. However, in practical SHM applications, structures are subjected to complex time-dependent, dynamic loading and various environmental effects, such as temperature fluctuations. Consequently, advanced data science methods and tools are necessary to adequately process the signal and extract relevant features for identifying, locating, quantifying, and classifying the damage (de Castro *et al*., 2019).

Wang & Ke (2024) identified two widely adopted feature extraction techniques for processing SHM-generated signals:

- Data-based feature extraction: This technique operates in the time domain, fitting suitable time series models to accurately represent the measured vibration data. It focuses on characteristics such as data linearity, amplitude, frequency, and signal duration. Techniques utilised include peak detection, statistical and waveform analyses.
- Physics-based feature extraction: This technique operates in the frequency domain, fitting suitable frequency series models to accurately represent the measured response data. It focuses on characteristics such as resonance frequencies, damping ratios, and modal frequencies. Techniques utilised include Fourier Transformation.

Irrespective of the feature extraction techniques utilised, the aim of data evaluation is to statistically compare the normalised sensor data with either a data-based or physics-based model. This process assists in identifying prominent anomalies that may indicate damage features for further damage prognosis.

2.6.2 Damage Prognosis

Damage prognosis represents a pivotal stage in SHM, where the severity of identified structural concern or damage is evaluated. It forecasts the probability of structural degradation or failure, allowing for proactive maintenance or repair measures to mitigate risks and ensure the structure's prolonged performance and safety. This process often relies on advanced model-based or data-based damage detection methods to make informed predictions regarding structural health. A flowchart broadly outlining these two methods is illustrated in Figure 2-16.

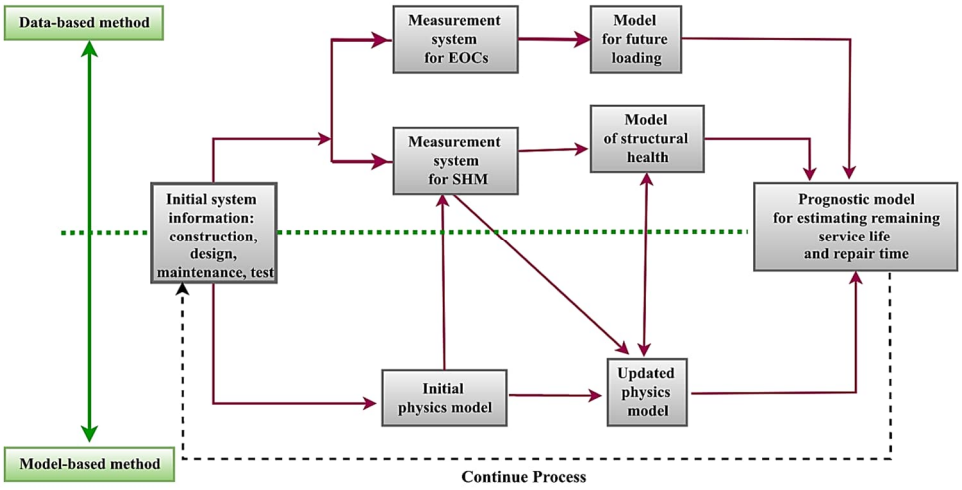

Figure 2-16: Flowchart of data-based and model-based damage prognosis approaches in SHM (Hassani & Dackermann, 2023)

In model-based methods, a numerical representation of the monitored structure in the form of a FE model is often utilised to estimate damages and responses under various conditions. An initial model is typically created using analysed design and experimental data and is continuously refined using sensor measurement data. An FE model can simulate material properties, geometry, support conditions, and loading to identify the causes of changes in behaviour and assess their impact on the structure's performance. The advantages of employing this method include the ability to predict the effects of loading and usage changes, provide recommendations for further measurement and inspection, and plan for rehabilitation and repair. Additionally, simpler data interpretation can be achieved when explicit links are established between measurements and potential causes. However, several drawbacks must be considered. Model development can be expensive and time-consuming, and errors in modelling may lead to erroneous predictions. Managing numerous candidate models can be challenging, and combinatorial challenges may arise, particularly with complex structures (Karbhari & Ansari, 2009).

In data-based methods, the state of a system is evaluated using data collected from historical records. This is achieved by identifying irregularities in structural behaviour using principles of pattern recognition. Unlike model-based methods, data-driven methods do not depend on the system behaviour model, making them adaptable to various scenarios due to their simplicity of implementation. The benefits of employing this method include the elimination of modelling and its associated costs, versatility in signal analysis options, and the ability for incremental training to track damage accumulation over time, making it suitable for long-term use in early detection scenarios. However, its drawbacks include the challenges in physically interpreting signals, limited support for decisions pertaining to rehabilitation and repair, indirect guidance for structural management activities like inspection, and an inability to justify replacement avoidance (Karbhari & Ansari, 2009).

Many researchers, including Zhang & Sun (2021) have integrated the physics-based FE models with data-based machine learning to enhance damage identification. This strategic integration leverages the strengths of each prognosis method to address unique challenges in implementing SHM and forms the basis for the development of DT systems.

2.7 DIGITAL TWIN APPROACH

A DT is a virtual representation of a physical asset or system, harnessing real-time data and advanced analysis models to replicate and visualise its features and behaviours. Originating from its early applications in the production and manufacturing industries (Garetti *et al*., 2012), DT is now gaining traction in civil engineering as an increasingly favoured SHM approach. While sharing many similarities with conventional SHM systems, DT-based SHM offers several additional advancements:

- Enables fully automated and networked transmission and storage of sensor data in real-time, eliminating the need for manual intervention
- Provides graphical detail and data via IoT platforms (such as BIM or point cloud), which can be readily accessed and understood by end-users
- Allows seamless integration of sensor data to modify analysis models (such as FE models) in a timely manner to predict the structure’s realistic performance condition
- Facilitates automated damage prognosis based on the structural performance and suggests measures to be taken by the end-users

DT-based SHM accentuates the digitisation and automation of the conventional SHM technique, promoting a more intelligent, interactive, and proactive asset management strategy (Liu *et al.*, 2023). Mahmmodian *et al*. (2022) describe that the four integration levels between

the physical and its virtual counterparts are categorised by the degree of automated data flow (Figure 2-17).

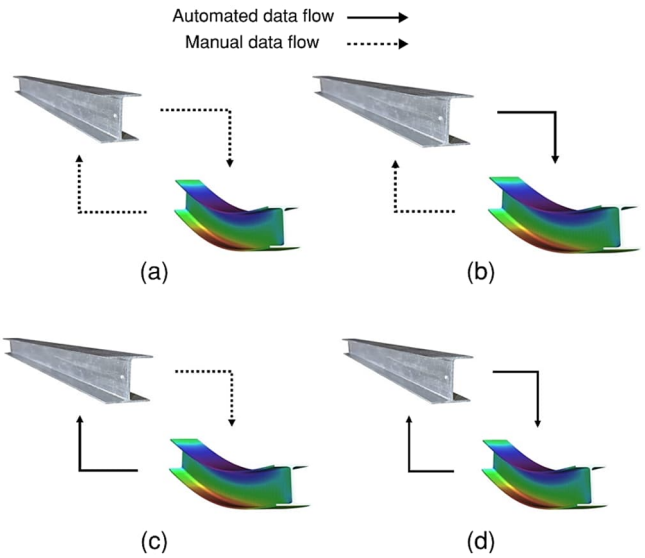

Figure 2-17: Data flow between physical and digital entities of different level of integration: (a) Digital model (b) Digital shadow (c) Digital generator, and (d) Digital twin (Mahmoodian *et al.*, 2022)

A digital model serves as the fundamental prerequisite for implementing a DT system. Within the infrastructure construction industry, digital models are often manually created as a conceptual blueprint for construction purposes or generated by simulating existing structures for desktop assessment. Tekinerdogan & Verdouw (2020) define other similar DT systems including a digital shadow and a digital generator. In a digital shadow, sensors are embedded within the physical object to automatically gather vital information for creating and updating the digital model. Conversely, a digital generator functions similarly to a digital model, but it automatically generates information derived from the digital model for the preventative maintenance strategies of the physical asset. A conventional SHM approach is generally classified within these three categories.

The manual development of a digital model without an automated flow of information through its physical entity does not embody the concept of a complete DT system. A complete DT system is characterised by the automation of information synchronisation between physical and digital assets. For systems considered to have DT integration from the perspective of SHM of civil infrastructure, the digital entity receives real-time information from the sensor measurement to dynamically replicate the characteristics and predict the behaviour or response

of the physical structure. Following a prognostic conditional assessment, the digital counterpart provides an automated preventive maintenance action to the physical structure, which the owner and the maintenance team can undertake.

Over the last decade, numerous research studies have explored the application of DT technology for damage detection in urban infrastructure. Ritto & Rochinha (2021) developed a DT framework by integrating physics-based computational models with machine learning capabilities. The machine learning classifier serves as the DT, trained with a stochastic computational model to support real-time detection of structural damages. Shim *et al*. (2019) proposed a DT-enhanced maintenance system for prestressed concrete bridges. This system combines a 3D DT model with a digital inspection system using image processing technology to identify and locate structural damage throughout the structure's lifecycle. Yu *et al*. (2022) employed a DT-based hybrid SHM and fatigue evaluation method for the steel deck of a cable-stayed bridge. This method synthesises monitoring data and FE models to develop a DT of a cable-stayed bridge, enabling the prediction of fatigue cracking in the steel deck.

The implementation of DT-based SHM is currently faced with numerous challenges that are continuously being addressed by many researchers. Foremost amongst these concerns is the high cost associated with the method due to the need for sophisticated software and hardware components (Hemdan *et al*., 2023). Employing DT-based SHM on civil infrastructure also involves highly technical and complex procedures, especially when incorporating advanced capabilities like machine learning and 3D image processing. Additionally, considerations must be made to ensure sensors are designed with reduced power consumption and weight, as highlighted by Chacón *et al*. (2023), to improve deployment and operational efficiency. Moreover, the lack of interpretability in some DTs poses an obstacle, as users may face difficulties comprehending and trusting predictions, particularly results generated by complex algorithms or black-box models. Furthermore, while gathering ample information is crucial, it is essential to avoid over-measuring the physical model, focusing instead on outputs relevant for identifying potential damage or accurately predicting future performance. Overcoming these challenges is vital in realising the full potential of DT in enhancing SHM and maintenance practices for civil infrastructures.

2.8 DISCUSSION

The traditional approach to evaluate the health of civil infrastructure, which relies solely on visual inspection and manual non-destructive test methods, is becoming an increasingly inefficient strategy in the face of rapid structural deterioration and growing traffic demand.

Innovative SHM methods offer a promising alternative, providing real-time, cost-effective, and accurate assessments of the structural integrity and performance of critical infrastructure assets. These advanced SHM techniques assist engineers and structural asset owners in evaluating and prioritising structural maintenance and repair activities, thereby ensuring the longevity and sustainability of structures and enhancing public safety.

Sensor technology is an essential component of an automated SHM system for collecting real-time measurement data with minimal human input. In this study, a selection of widely used and emerging contact and non-contact sensors dedicated to measuring the physical structural response was identified. These sensors, along with their key advantages and limitations, are summarised in Table 2-1.

Table 2-1: Summary of key advantages and limitations of various sensors for SHM

Sensors		Advantages	Limitations
Contact Type	LVDT	Precise, stable, reliable, and relatively low-cost.	Sensitive to magnetic field interferences and temperature variations.
	Piezoelectric	Excellent for local damage detection, small, and relatively low-cost.	Require specialised knowledge and methods in post-processing to determine damage magnitude and location.
	Potentiometer and Extensometer	High accuracy, repeatability, and relatively cost-effective.	Susceptible to wear and tear over long-term use. Extensometer may introduce higher setup complexity and cost.
	Fibre Optic	Consistent performance, lightweight, provides versatility in various measurements (strain, vibration, and temperature), non-conductive and electrically passive.	Require specialised knowledge in signal processing and optical engineering for post-processing, cumbersome and laborious installation, and high cost.
Non-contact Type	LiDAR	Ability to capture spatial and spectral data for digital information modelling, less operation disruption, and enhances safety.	Operability dependent on environmental conditions, requires strategic positioning, demanding post-processing (noise filtering and data interpretation), and high cost. Only offers surface inspection.
	Vision-Based	Ability to capture high quality images and videos, drones can increase efficiency, less operation disruption, and enhances safety.	Operability highly dependent on lighting conditions, requires sophisticated algorithms and methods for post-processing, and moderate-to-high cost. Only offers surface inspection.
	Radar	Stable, robust, and relatively low-cost.	Operability limited to signal range, requires strategic mounting of reference targets and radar sensors. Only offers surface inspection.

Sensor selection for an SHM system depends on factors such as the target physical characteristic (geometry, displacement, strain, crack, or vibration), desired performance criteria, environmental conditions, ease of installation, deployment efficiency, post-processing complexity, and cost. It can be observed that sensors dedicated to measuring local physical changes are generally low-cost with relatively simpler post-processing, while sensors capturing readings for a larger area may necessitate advanced filtering to extract relevant data.

Contact sensors are known for their precision and reliability, however, certain types, such as strain gauges, though inexpensive as standalone components, often require costly interfacing equipment and labour-intensive surface preparation. These factors, along with the need for specialised knowledge and meticulous installation, significantly increase deployment time and labour costs. To address these limitations, alternative contact sensors that emphasise ease of installation and minimise labour-intensive setup are essential. In contrast, non-contact sensors, are typically associated with higher costs due to sophisticated hardware and software requirements for long-range data collection. However, little research has explored the feasibility of using non-contact sensors for short-range monitoring in SHM systems. In situations where structures can be monitored in close proximity without physical contact, sensor performance does not need to be highly advanced. Such short-range non-contact systems could potentially achieve sub-millimetre accuracy while significantly reducing costs and installation complexity, making them a practical and affordable solution worthy of further investigation.

The integration of wireless communication sensors is critical for next-generation SHM and DT systems, enabling seamless data transmission and real-time monitoring. However, current IoT-enabled SHM systems often lack near real-time integration with DT models, relying on manual data retrieval and processing. This manual approach undermines the automation essential for a DT-based SHM system. A cost-effective IoT system capable of effortless deployment and real-time data integration with DT models would bridge this gap, ensuring efficient transmission of sensor data to predictive models.

The DT paradigm is emerging as a transformative approach to SHM, offering intelligent, interactive, and proactive asset management. By creating a virtual replica of the monitored structure, DTs allow real-time simulation and analysis of structural behaviour, enabling engineers and asset managers to anticipate risks, optimise maintenance strategies, and extend service life. Despite their potential, DT systems are often complex and prohibitively expensive, particularly for small-scale SHM applications. A simplified, cost-effective numerical DT model that balances accuracy with practicality for such applications remains largely unexplored. Developing such an approach would facilitate more accessible and scalable DT-based SHM systems, making them viable for real-world infrastructure damage prognosis and asset management.

3 DT-BASED SHM FRAMEWORK

3.1 INTRODUCTION

In this chapter, the conceptualisation and development of a DT-based SHM framework designed to simulate the mechanical behaviour of monitored structures is presented. The framework comprises two core systems, the hardware and software systems, which permit the automated transfer of data between the physical structural model and the virtual digital model in realising the smart monitoring of structural behaviour using DT principles. The hardware system is a smart sensor prototype that includes both the proposed contact and non-contact displacement sensors, as well as a cost-effective IoT-enhanced wireless communication sensor. The software system constitutes a FE model-based, numerical model with automated and interactive post-processing functionalities, facilitated by a developed software program named "ReConTwin". The name "ReConTwin" is derived from the FE analysis software, *ReConAn* (an abbreviation for Reinforced Concrete Analysis), which ReConTwin uses to create a DT – conveying the notion of extending the analysis software's capability to twin the RC beam it analyses. Supported by ReConTwin, the software system can perform near real-time model updates for automated structural analysis, mechanical behaviour prediction, and damage diagnosis.

The outline of this chapter is sequentially organised as follows:

- Overview of the framework architecture for the DT-SHM
- Physical structural model development and experimental setup
- Contact and non-contact displacement sensor platforms
- Integration of the wireless communication sensor
- Assembly and calibration of the hardware system
- Conceptualisation of the software system architecture
- Implementation and calibration of a FE model-based DT model
- Development of ReConTwin, incorporating features for automated model update, post-processing, and damage diagnosis
- Conclusions

3.2 FRAMEWORK ARCHITECTURE

The primary aim of this study is to demonstrate the feasibility of establishing a practical and cost-effective SHM framework enhanced by DT technology for health monitoring of civil infrastructure. The key features required for this implementation include:

- Affordable sensors
- Real-time monitoring facilitated by a cost-effective wireless communication network
- Relatively simple post-processing procedures
- Interactive and user-friendly software interface

In this study, a DT-based SHM system was developed to digitally predict the mechanical behaviour of a RC beam. The hardware configuration includes IoT-enhanced displacement smart sensors capable of wirelessly transmitting real-time deflection data of the physical beam specimen to cloud storage. The software system consists of a FE-based digital model supported by interactive and automated post-processing capabilities to perform near real-time model updates, analyses, and damage diagnosis. These two core systems serve as vital links between the physical and digital object domains, permitting automated data flow and synchronisation between the physical and digital models. Figure 3-1 provides an overview of the proposed framework architecture.

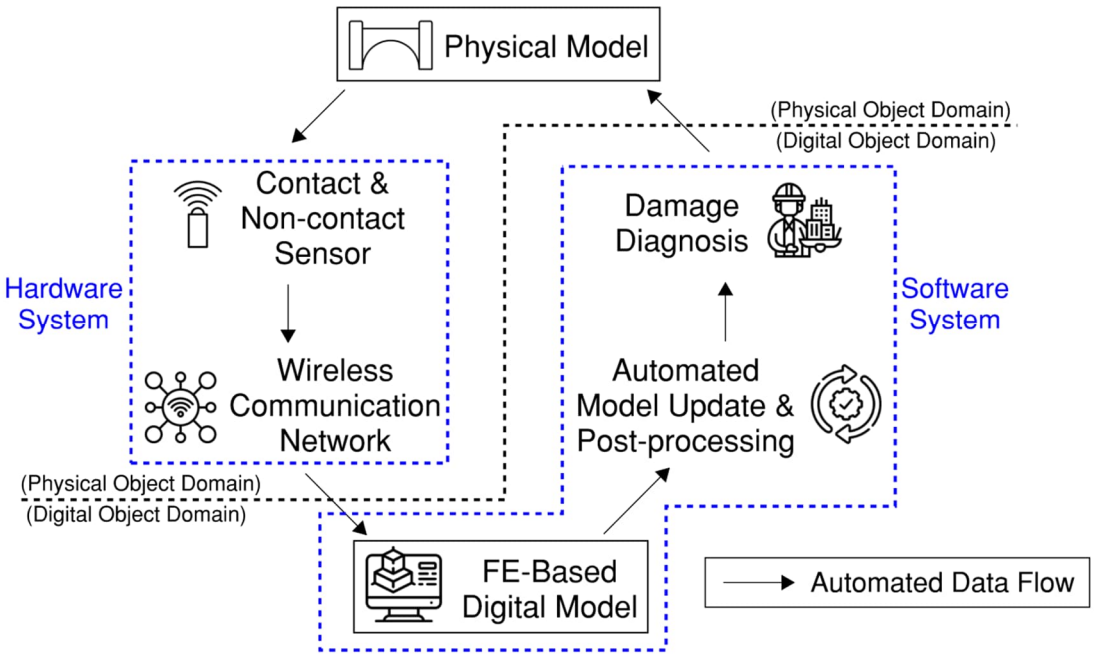

Figure 3-1: DT-based SHM framework architecture overview

3.3 PHYSICAL MODEL AND EXPERIMENTAL SETUP

The structural element representing the physical model of the monitoring subject in this study's implementation of a DT-based SHM framework is a RC beam specimen fabricated in a laboratory. Five identical RC beam specimens were constructed, each embedded with DOFS cables for strain result verification. The load testing of the beams was carried out in two test stages while subjected to an incremental, three-point bending static loading. In the first test stage, four beam specimens were tested to generate data for calibrating the digital FE model based on resultant force-displacement behaviour, and to collect strain data for comparison purposes. In the second test stage, the remaining beam specimen was tested to assess the performance of the developed DT-based SHM system, and the accuracy of its post-processing capability in estimating the applied loading and surface strain. This section elaborates on the procedures involved in preparing the beam specimens and illustrates the load testing setups, both of which contributed to the creation of the physical model for the DT-based SHM system.

3.3.1 Beam Specimen and Loading Setup

The RC beam specimens used in this experimental study have a total longitudinal length of 2060 mm with a rectangular cross-sectional width and depth of 150 mm by 230 mm, respectively, with a shear span-to-depth ratio of 7.8. Each beam was under-reinforced with two Ø12 mm bottom and two Ø10 mm top high-yield tensile reinforcing longitudinal bars, designed to ensure a ductile flexural failure mode. The strength of the high-yield reinforcing steel was verified through tensile testing conducted in the laboratory, as highlighted in Chapter 3.3.3. Adequate anchorage of the longitudinal Ø10/12 bars extending past the beam supports was provided. Additionally, Ø8 mm closed-loop vertical mild steel stirrups without surface deformation patterns were equally installed and spaced at 100 mm intervals along the beam length to prevent shear failure modes. A concrete cover of 25 mm between the concrete perimeter and the nearest reinforcing steel surface was achieved with the provision of plastic spacing blocks. The geometry of the beam specimen and the layout of the reinforcement are illustrated in Figure 3-2 and Figure 3-3, respectively.

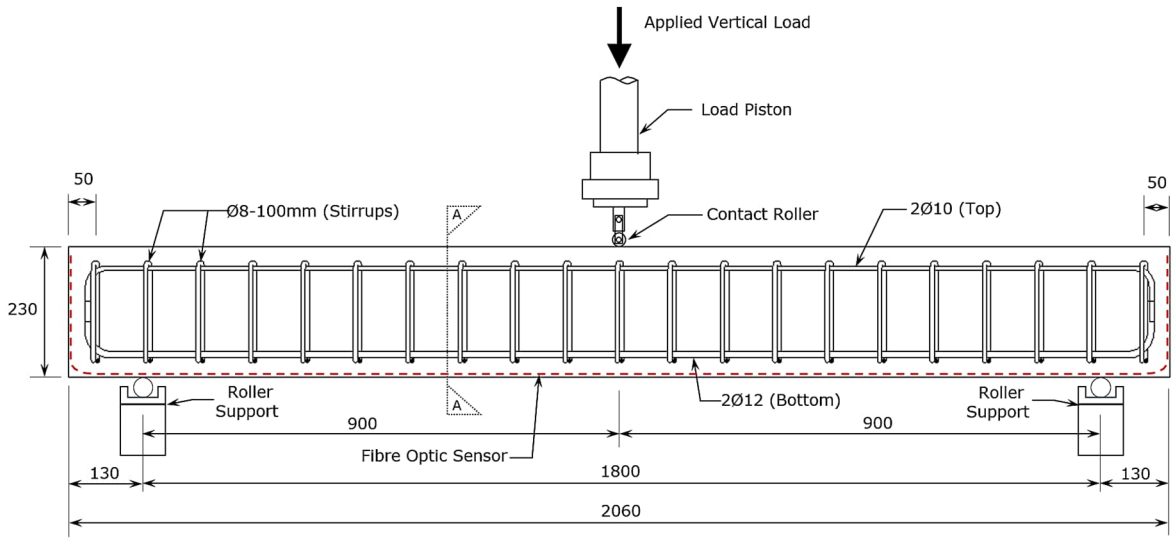

Figure 3-2: RC beam specimen longitudinal elevation (measurements in mm)

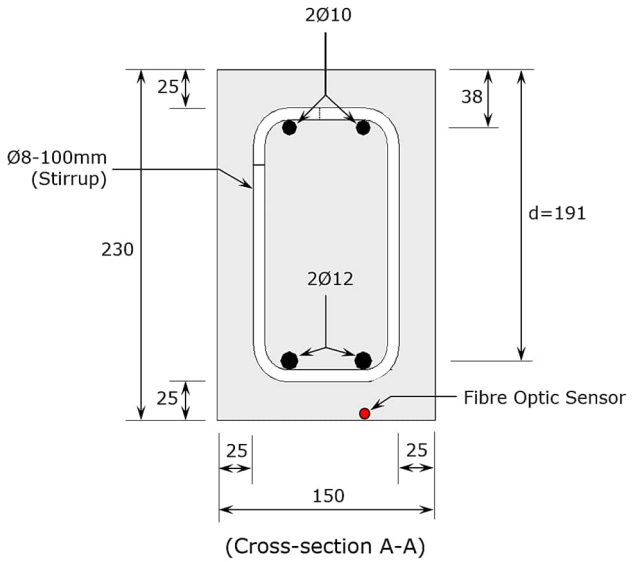

Figure 3-3: RC beam specimen cross-sectional view (measurements in mm)

The load test setup for all beam specimens adopted a three-point bending test configuration, with beams simply supported on two roller supports at a clear span of 1800 mm. A static, vertical load was applied at the beam mid-span location with a contact roller, facilitated by the load piston of an MTS – 500 kN hydraulic testing machine. The loading and unloading of the beams were force-controlled at a constant rate of 4 kN per minute. The load testing of the beam specimens comprised two main stages:

- Load Test Stage 1: Four RC beam specimens were each subjected to an incremental loading, reaching a maximum load of 56 kN. The load step was 4 kN, with each load increment maintained for 3 minutes for data collection. This test stage aimed to determine the beam's average force-displacement response using LVDT for vertical displacement measurement, which served as crucial data to calibrate the digital FE model. Moreover, surface strain measurements obtained from embedded DOFS during this stage were used to verify against those estimated by the FE-based digital model.
- Load Test Stage 2: A single RC beam specimen was subjected to two phases of testing, with a 2-minute data collection period at the end of each loading or unloading cycle.
    - In the first test phase, the beam underwent three load cycles, progressively loading and unloading between 0 kN and 4 kN, 4 kN and 12 kN, and 12 kN and 20 kN. The maximum load of 20 kN was within the beam's elastic limit. This phase aimed to simulate the repeated day-to-day use of the RC beam structure within the beam's elastic limit.
    - In the second test phase, the beam test procedure mirrored Load Test Stage 1, where the load was incrementally increased from 0 kN to a maximum load of 56 kN with a load step of 4 kN. This phase aimed to simulate the condition under which the RC beam structure is overloaded, exceeding its elastic limit.

The second test stage aimed to evaluate the performance of the hardware system (IoT-enhanced smart sensors) and the software system's ability to accurately estimate the imposed load and surface strain of the monitoring beam.

3.3.2 Control Measurement Sensors

Two sensor systems, LVDT and DOFS, were utilised during the load testing stages to measure the vertical displacement and the tensile strain at the beam's soffit at mid-span, respectively. These sensor systems were not part of the developed DT-based SHM framework and were solely dedicated to gather control displacement and strain measurements for comparison with the DT-SHM's results. The LVDT was positioned centrally beneath the beam, supported vertically by the secured clamp arms, with its spring-loaded core consistently in contact with the beam's soffit surface (Figure 3-4). In stage one of the testing, the measured deflection combined with the known applied point load, was utilised to establish a force-displacement behaviour benchmark based on which the FE model can be calibrated. Additionally, in test stage two, the LVDT served to assess the accuracy of the proposed contact and non-contact

sensors. The LVDT had a measurement resolution of 0.001 mm (1 μm), and due to the steady nature of the applied static loading, the sampling rate was set to 1 Hertz.

Figure 3-4: LVDT installed beneath the beam for mid-span displacement measurement

The DOFS system utilised to determine the maximum tensile strain along the bottom surface of the test beams consisted of embedded Fibre Optic (FO) cables and a laser signal processing interrogator. Provided that the point of maximum strain might not align precisely with the centre of the beam, this system allowed for the identification of multiple strain measurement points along the length of the FO cable, enabling accurate determination of the largest strain value.

Two types of FO cables were applied. The cable embedded within the concrete was a 3.2 mm diameter BRUsens V9 strain sensing cable by Solifos (Interlab, 2024). Encased in a metal tube and outer polyamide sheath, these cables were highly flexible for installation with small bending radii, resistant to crushing, and possessed high tensile strength capable of measuring strain up to 1%. Prior to applying the debonding agent for concrete casting, the surfaces of the beam mould were meticulously cleaned. The FO cable was straightened and affixed to the side and bottom surfaces of the beam mould using aluminium adhesive tapes at equal intervals of 120 mm apart (Figure 3-5). The second type of FO cable was a 3 mm diameter E2000 cable (EFBElektronik, 2024), featuring an aramid yarn protective layer and end-angle polished connectors, and was spliced to form a complete loop between the BRUsens V9 cables and the FO interrogator.

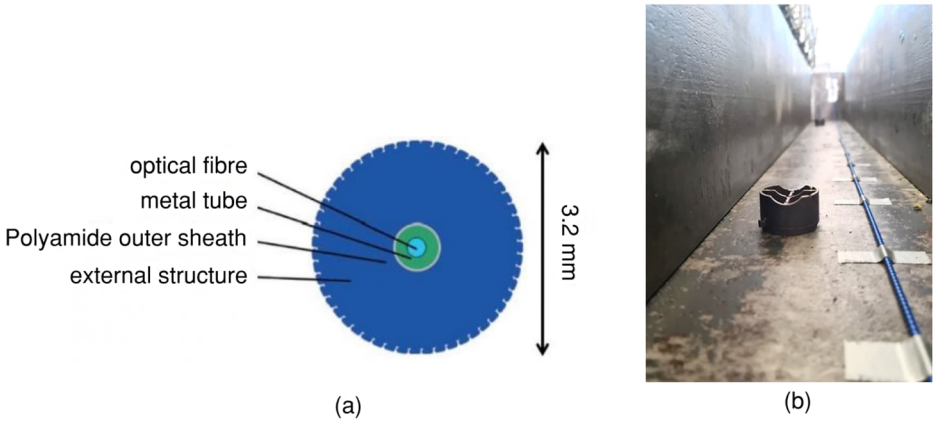

Figure 3-5: BRUsens V9 FO cable: (a) Cable cross-sectional view (Interlab, 2024), and (b) Installation of cable along the bottom of the beam cast mould

Processing and monitoring of the strain measurements along the FO cable loop were accomplished using the fTB 2505 interrogator by fibrisTerre (2024). It operates on fibrisTerre's patented Brillouin Optical Frequency Domain Analysis (BOFDA) technique to obtain highly accurate, reliable, and low-attenuation readings. The technique relies on the Brillouin effect, where the interrogator detects backscattered acoustic waves generated by the interaction between the injected probe light and pump light waves (Figure 3-6). The arrival time of the light waves is utilised to quantify the magnitude of contraction and extension at specific measuring points along FO cable's length. Leveraging this technology, a spatial resolution of one reading every 52 mm was achieved during the load tests.

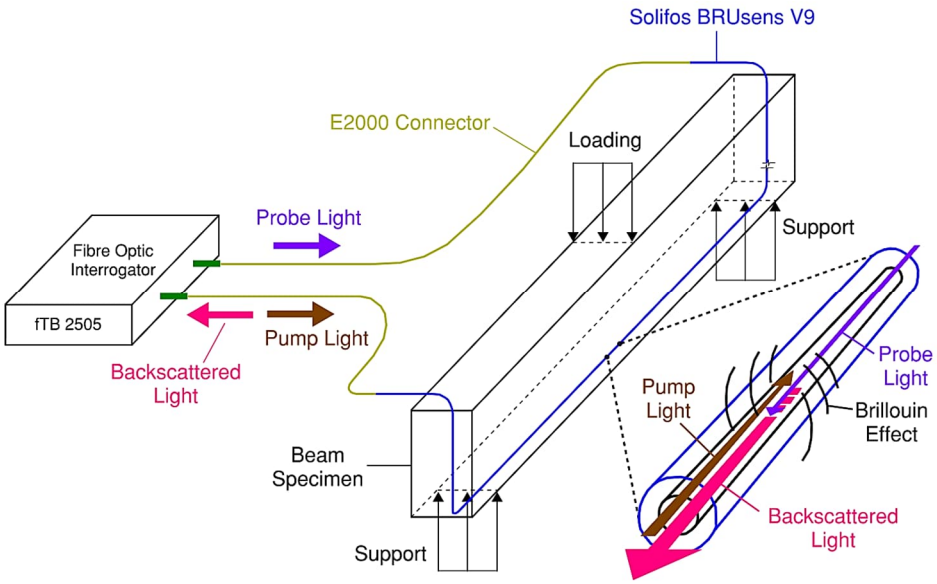

Figure 3-6: DOFS system installation setup and fibre optic working principle

3.3.3 Material and Sample Preparation

All concrete beam specimens were cast using the mix proportions summarised in Table 3-1 with a water-cement ratio of 0.47. The cement comprised Ordinary Portland Cement (OPC) blended with ground-granulated blast-furnace slag and fly ash. A small poker vibrator was operated with great care to adequately consolidate the concrete mix within the beam mould. The demoulded beams, test cubes, and cylinder samples were covered with polyethylene film to minimise moisture evaporation and stored in an indoor environment until the day of testing specified in Table 3-2 (Figure 3-7).

Table 3-1: Concrete mix proportions for all the RC beam samples

Constituent	Mass per Cubic Metre [kg/m^3]	Percentage per Cubic Metre [%]
Coarse aggregate (crushed Dolomite 19 mm)	1202	49.5
Fine aggregate (River sand)	634	26.1
Cement (42.5N OPC CEM II B-M)	404	16.6
Water	190	7.8
Total	2430	100.0

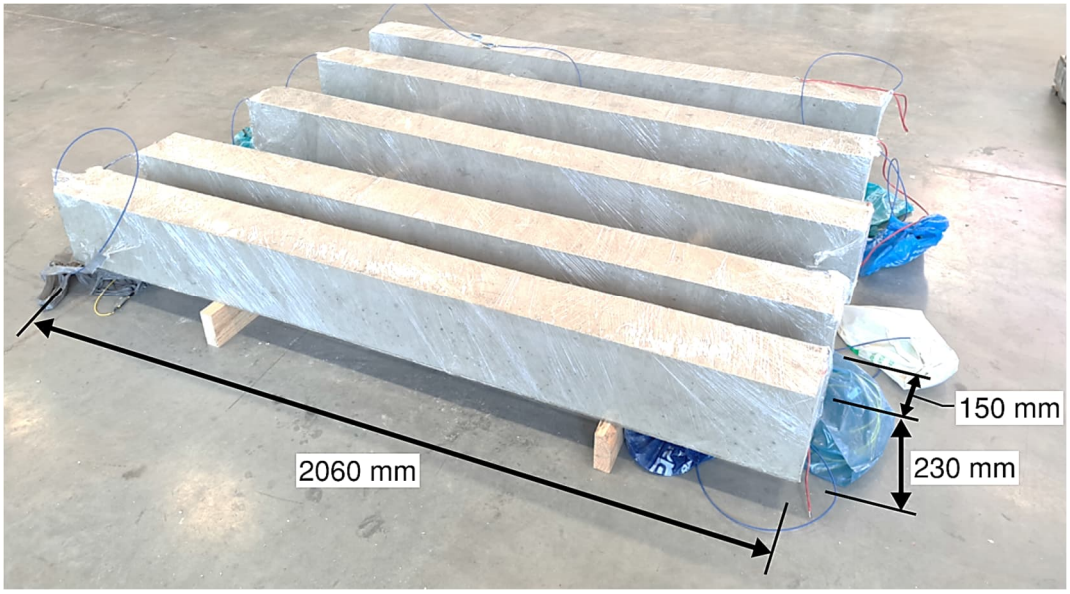

Figure 3-7: Cast and covered RC beam specimens

A total of six 150 mm concrete cube and six 100 mm diameter by 200 mm long concrete cylinder samples were tested. On each respective day of the three-point bending test stage, three concrete cube samples and three concrete cylinder samples, cast concurrently with the same concrete mix as per the beam specimens, were subjected to sample testing. These tests aim to determine the material properties of the concrete, relating to its compressive strength, static modulus of elasticity, and tensile strengths (Figure 3-8). The samples were prepared and tested based on the South African National Standards SANS 5860 (2006), SANS 5861-1 (2006), SANS 5863 (2006), and SANS 6253 (2006), as well as British Standard BS 1881-121 (1983). Detailed test methods for the concrete cube and cylinder samples are outlined in Appendix A.1.

(a) (b) (c)

Figure 3-8: Concrete material properties test: (a) Compressive cube test, (b) Compressive static elasticity modulus test, and (c) Split tensile test

Table 3-2 presents the average test results of the concrete material properties obtained from the cube and cylinder sample groups for the two test stages, along with their respective coefficients of variation. The low values of the calculated coefficients indicate a desired low spread of test results relative to the mean, demonstrating consistent and reliable material properties across the tested samples.

Table 3-2: Average material properties of concrete sample groups

Concrete Sample Group	Average Dry Density [kg/m^3]	Average Compressive Strength [MPa]	Average Modulus of Elasticity [GPa]	Average Tensile Strength [MPa]
Load Test Stage 1 (35 days after cast)	2417 {0.72%}	52.0 {0.88%}	30.5 {6.81%}	3.10 {10.31%}
Load Test Stage 2 (154 days after cast)	2339 {0.14%}	60.5 {2.14%}	34.0 {11.30%}	3.25 {8.33%}

(Note: percentage values in {} denote coefficient of variation)

The material properties of the reinforcement bars were determined through tensile tests conducted on three Ø12 mm and three Ø10 mm bar samples cut from the same high-tensile bars used in the concrete beam specimens. The yield strength for each reinforcement bar sample was determined from the stress-strain graph as the stress at which plastic deformation begins with little or no increase in load. This was identified by the yield point in material with a distinct yield plateau or, in cases without a clear yield point, the 0.2% offset method was used. The ultimate tensile strength was identified as the peak stress before necking. A typical stress-strain graph of one of the Ø10 mm sample is shown in Figure 3-9.

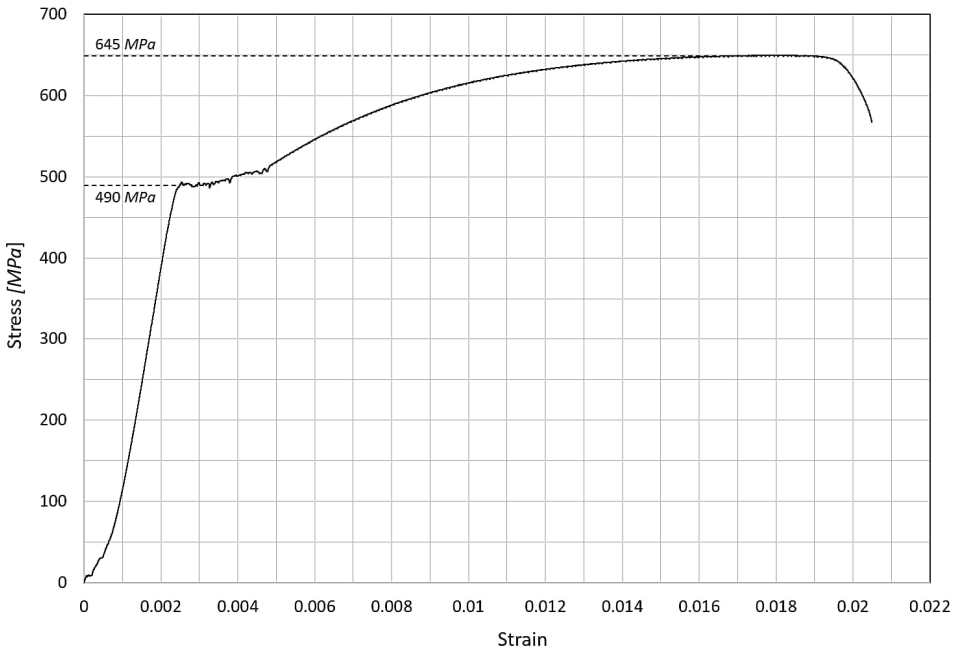

Figure 3-9: Typical stress-strain graph of a Ø10 reinforcement bar sample

The average yield strength and ultimate tensile strength were calculated to be 493 MPa and 650 MPa, respectively. The average modulus of elasticity of the steel was determined to be 200 GPa.

3.4 DISPLACEMENT SENSORS

Driven by rapid technological advancement, sensors are improving in performance while becoming more commercially accessible. These advancements are advantageous for the implementation of a practical and cost-effective DT integrated SHM prototype. In this section, two low-cost electronic sensors, a contact and a non-contact type, dedicated for measuring the vertical displacement of monitored RC beams are proposed. Their working principles and capabilities are discussed below.

3.4.1 Contact Sensor

A potentiometer, often colloquially referred to as a “potmeter” or simply a “pot”, is an analog device widely used in various electrical appliances today. Its name stems from the combination of “Potential Difference” and “Metering”. As the name suggests, this component measures the potential difference within an electrical circuit by comparison to a known voltage. As it operates without requiring an external power source, it is commonly considered as a passive transducer (Todd, 1976). Potentiometers are valued for being cost-effective, durable, and easy to operate, offering precise and versatile control over electrical parameters.

In its simplest form as illustrated in Figure 3-10, a potentiometer comprises three connection terminals: two fixed, and one variable. The fixed terminals are linked to both ends of the resistive track, which possesses intrinsic low-temperature conductivity and serves as the main resistance body. The central variable terminal connects to a wiper that maintains constant electrical contact with the resistive track. Typically, the wiper is attached to an external slider or a rotary shaft. Mechanical adjustment of the slider or shaft causes the wiper to move along the resistive track, thereby altering the resistance within its connected electrical circuit.

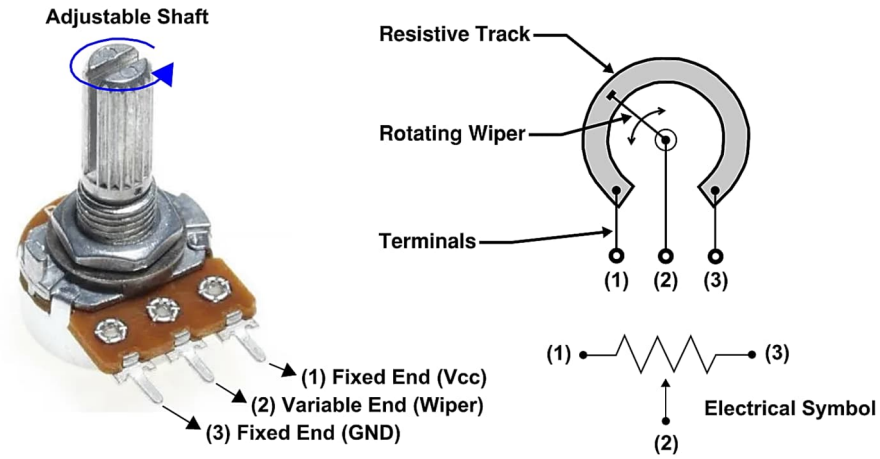

Figure 3-10: Construction of a typical potentiometer

Various electrical configuration of the device serves different applications and use cases. When only one of the fixed end terminals and the variable terminal are used, it functions as a variable resistor, regulating current flow in a circuit (also known as a rheostat). Conversely, a potentiometer utilises all three terminals and serves as a voltage divider (Schweber, 2021). Manufacturers produce a wide range of potentiometer to meet various technical requirements and their operational environments. Amongst them, the logarithmic potentiometer is a complex type designed to adjust potential in logarithmic increments. This type is commonly found in audio equipment, where human perception of volume varies logarithmically nonlinearly (RS, 2023). In contrast, simpler linear or rotary potentiometers with basic control mechanisms and working principles are prevalent in applications like light dimming switches and displacement measurement devices.

A linear potentiometer is commonly utilised as a linear position sensor, converting the linear movement of an object into corresponding electrical signals. It achieves this by proportionally dividing the voltage based on the ratio of the measured resistance to the total resistance relative to the position of the wiper (Figure 3-11). A linear relationship between the change in voltage and the change in wiper displacement can subsequently be achieved. This implies that when the wiper extends halfway from its starting position, the output voltage theoretically corresponds to fifty percent of the input voltage.

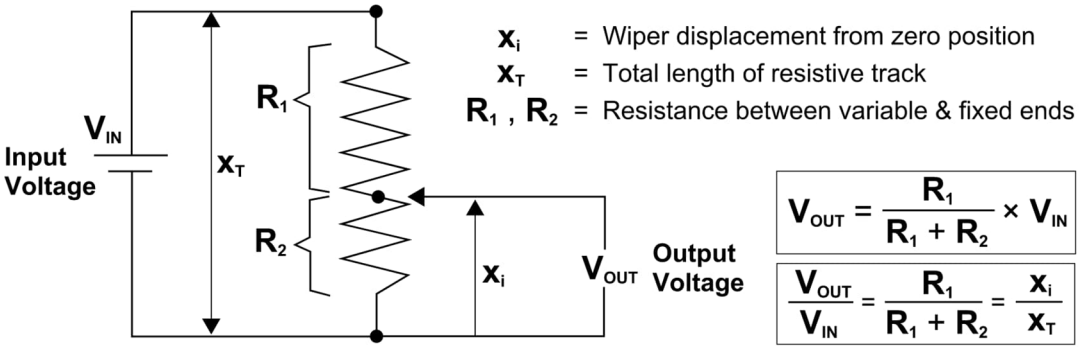

Figure 3-11: Linear potentiometer electrical circuit diagram and input-output relationship

The contact sensor selected for this study is a low-cost linear position sensor ($84 USD) manufactured by Variohm EuroSensor (2024), as shown in Figure 3-12. This sensor provides precise measurement of linear displacement with a maximum extension range of 50 mm, making it ideal for small-scale beam deflection measurements. Its main body is an electrical track consisting of a sealed layer membrane (Figure 3-13), ensuring compactness and minimal maintenance.

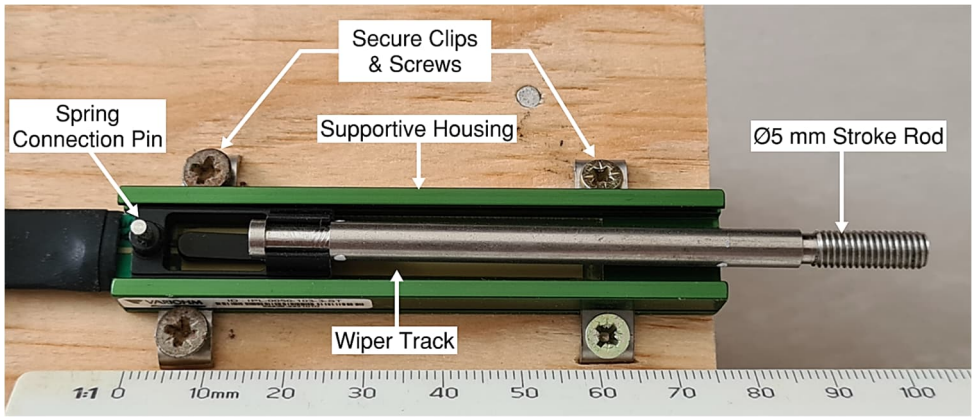

Figure 3-12: Linear potentiometer sensor (serial code: IPL-0050-103-3-ST)

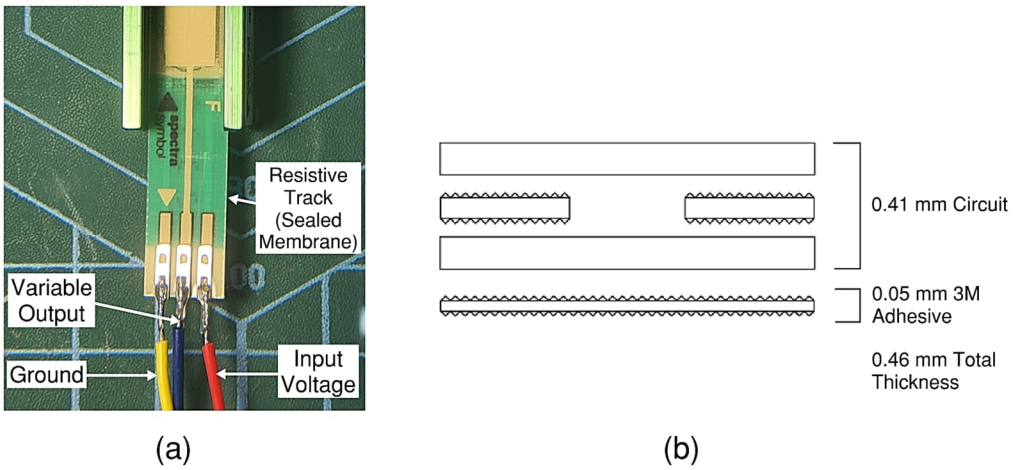

Figure 3-13: Linear potentiometer membrane: (a) Crimplflex solder tab and electrical connection, and (b) Cross-sectional view of the sealed resistive circuit membrane

The body of the potentiometer sensor is contained in a robust support housing with side grooves, allowing for convenient mounting on any surface using secure clips and screws. Other notable features of this linear potentiometer are summarised:

- Total electrical resistance of 10 kΩ
- Independent linearity of 3%
- Crimpflex solder tab connector for ease of soldering connection (Figure 3-12a)
- Ingress Protection (IP) 65 rating (resistant to intense water spray and dust)
- Operating temperature ranges between -40 °C and +85 °C
- Average power draw of 500 mW

To maintain constant contact between the stroke rod and the soffit of the RC beam, an elastic band was secured to the support stand and to the spring connection pin.

3.4.2 Non-Contact Sensor

An Infrared (IR) sensor is a type of non-contact sensor prevalently used for measuring distances. Compared to ultrasonic sensors, they are generally cheaper and possess faster response times, making them popular in various applications such as robotics, proximity sensing, and gesture recognition. The IR light's electromagnetic wavelength is longer than that of visible light, making it invisible to the human eye.

The IR sensor comprises an emitting IR Light-Emitting Diode (LED) and an IR photodiode receiver. Its working principle involves the technique of time-of-flight processing, where the time taken for the emitted IR light pulses to be detected by the receiver after bouncing off an

object's surface is measured, as illustrated in Figure 3-14. This measurement is used to calculate the distance between the sensor and the object. Subsequently, the sensor's performance is negatively impacted by reflective materials, including scattering, reflectivity, and absorption characteristics (Mohammad, 2009).

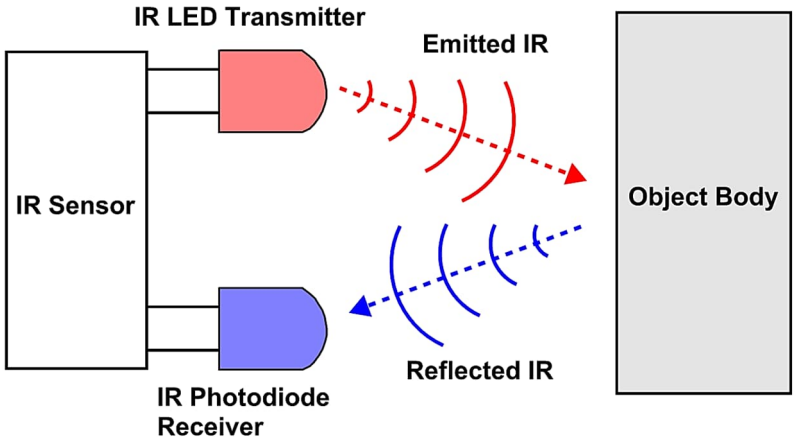

Figure 3-14: Working principle of an IR distance sensor

The electrical circuit layout of a typical IR distance sensor is shown in Figure 3-15. The circuit consists of numerous electrical components regulating the emission, detection, processing, and output of the IR signals. A LED drive circuit converts electrical signals into IR signals and controls the frequency of IR transmission. Conversely, the signal processing circuit converts detected IR signals into electrical signals. The oscillation circuit and voltage regulator modulate signal amplification and maintain appropriate circuit voltage respectively. Lastly, the output circuit voltage manages the processed voltage output to the connected external microcontroller or microprocessor.

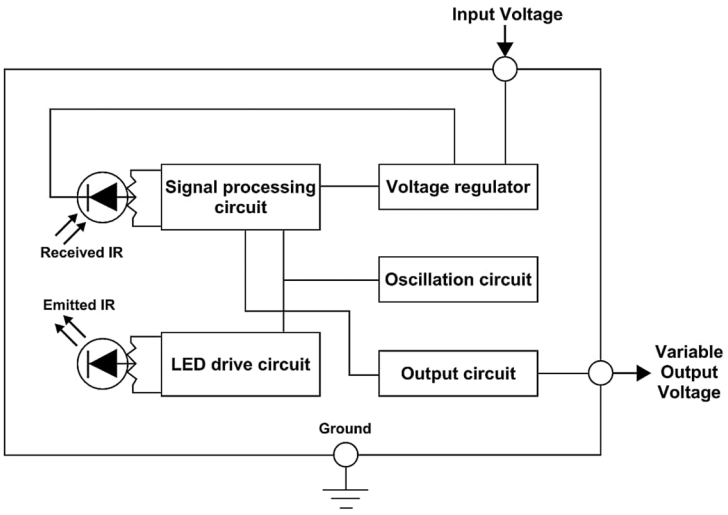

Figure 3-15: Electrical circuit layout of a typical IR distance sensor (Sharp, 2024)

Figure 3-16 illustrates the non-contact sensor selected for this study: a low-cost IR distance sensor ($15 USD) manufactured by Sharp (2024). This sensor integrates a position-sensitive detector, an IR LED, and signal processing circuits. It utilises a triangulation detection method, which minimises measurement variations as a function of the object reflectivity, temperature variations, and extended operating duration. This sensor specifications allow for a measurement range of 4 cm to 30 cm and is well-suited for use as a proximity sensor. The lenses of the emitter and receiver are housed within the lens casing. Other notable features of this IR distance sensor include:

- Operating voltage: between 4.5 V and 5.5 V
- Supply current of 22 mA
- Sample time of 16.5 ms / 60 Hz
- Mass of 5 mg
- Operating temperature ranges between -10 °C to +60 °C

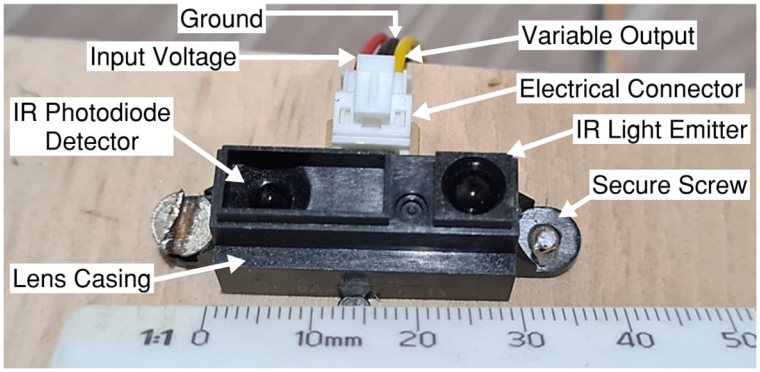

Figure 3-16: Infrared light analog distance sensor

3.5 WIRELESS COMMUNICATION SENSOR

Supported by rapid technological advancement, MEMS technologies have seen significant improvements in performance and cost reduction, making them increasingly accessible commercially over the past decade. The Arduino (2024) ecosystem is one such electronic platform benefitting from this trend, gaining popularity amongst hobbyists, students, and professionals for creating a wide array of robotics and IoT application projects. Arduino complements its hardware with an open-source software platform known as the Integrated Development Environment (IDE). The IDE offers users an intuitive interface for creating, compiling, and uploading code to Arduino microcontrollers. This modern code editor simplifies the programming process, making it easily adoptable even for individuals without advanced technical expertise. Additionally, the Arduino IoT Cloud application supports the management of Arduino-based projects, providing tools for remote data visualisation, storage, device

management and updates. Although the free version of the plan offers only 100 MB of storage for sketches and libraries, paid plans offer unlimited sketch storage and extended cloud data retention periods, enhancing the platform's capabilities and utility for more complex and data-intensive projects.

The Arduino Nano 33 IoT, shown in Figure 3-17, is a robust microcontroller equipped with wireless communication capabilities. It was selected to enhance both contact and non-contact displacement sensors with IoT capabilities in realising the DT-SHM framework in this research work. Its compact dimensions (45 mm × 18 mm × 5 mm), affordable price ($25 USD), and versatile digital Input/Output (I/O) pins made it an ideal choice as a wireless communication sensor that could seamlessly integrate with the displacement sensors. Its key hardware features (Arduino, 2024) are summarised as follows:

- Microcontroller: SAMD21G 32-bit, 48 MHz, built-in RTC (Real Time Clock)
- Operating voltage: maximum input voltage of 21 V, regulated pin voltage output of 3.3 V (DC current per I/O pin = 7 mA)
- Wireless connectivity: Wi-Fi 802.11b/g/n 2.4 GHz, Bluetooth Low Energy (BLE) 4.2
- Peripheral connection: Micro-USB port
- Security: a built-in crypto chip securely stores up to 16 keys, certificates, or data
- Inertial Measurement Unit (IMU): LSM6DSL 3-axis accelerometer and 3-axis gyroscope
- Operating temperature ranges between -40 °C and +85 °C

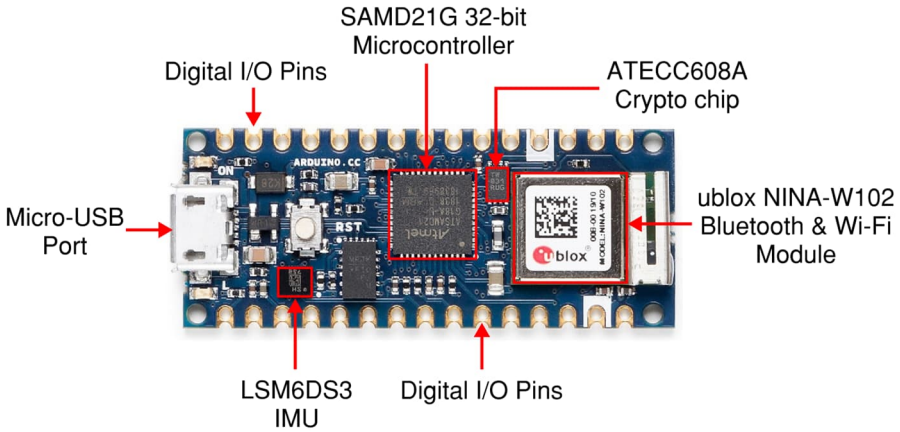

Figure 3-17: Arduino Nano 33 IoT and key components (Arduino, 2024)

3.6 HARDWARE SYSTEM ASSEMBLY

The two displacement sensors and the wireless Arduino communication sensor are essential core components forming part of the hardware system of the DT-based SHM framework with IoT capabilities. An overview of the proposed assembled hardware system, illustrating its components and their connectivity relationships, is shown in Figure 3-18.

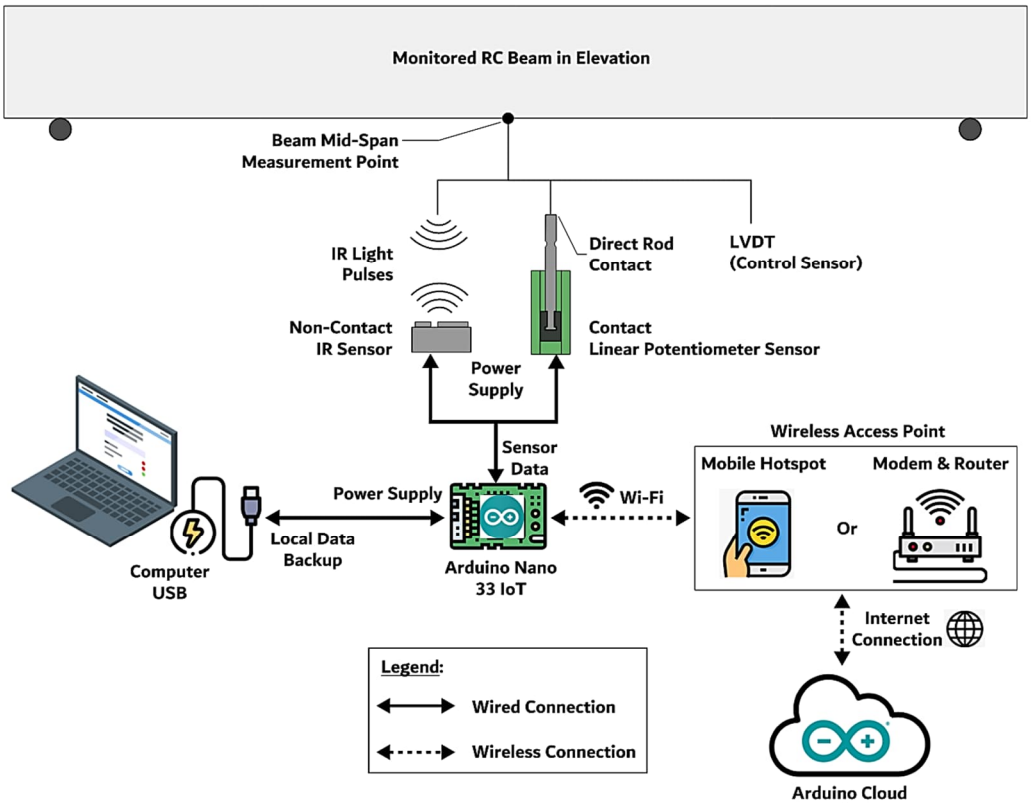

Figure 3-18: Proposed hardware system overview

During the experiment, both contact and non-contact displacement sensors were securely mounted on a platform constructed from plywood and were elevated to the appropriate level within their displacement sensing range (Figure 3-19a). These sensors, along with the LVDT (control measurement sensor), were strategically positioned to measure the beam soffit deflection at the same mid-span location beneath the RC beam specimen. The IR sensor was positioned to operate within a detection range of 50 mm to 70 mm below the beam, corresponding to its maximum and minimum vertical displacements, respectively. This range was selected based on the findings of Trojaniello *et al*. (2014), which indicated that the same IR sensor achieves optimal accuracy at detection distances of less than 70mm. The displacement sensors were interfaced with the Arduino Nano 33 IoT microcontroller through

its digital I/O pins, with the detailed electrical circuit configuration illustrated in Appendix A.2. To simplify electrical wiring connections to the digital pins, a compatible terminal adapter board was utilised as an intermediary interface (Figure 3-19b). The Arduino was housed in a robust 2 mm thick cuboidal Acrylonitrile Butadiene Styrene (ABS) plastic enclosure, measuring 112 mm × 62 mm × 40 mm. The enclosure provided mounting rigidity for all connected wiring components and offered an IP 54 rating, indicating moderate protection against dust ingress and water splashes.

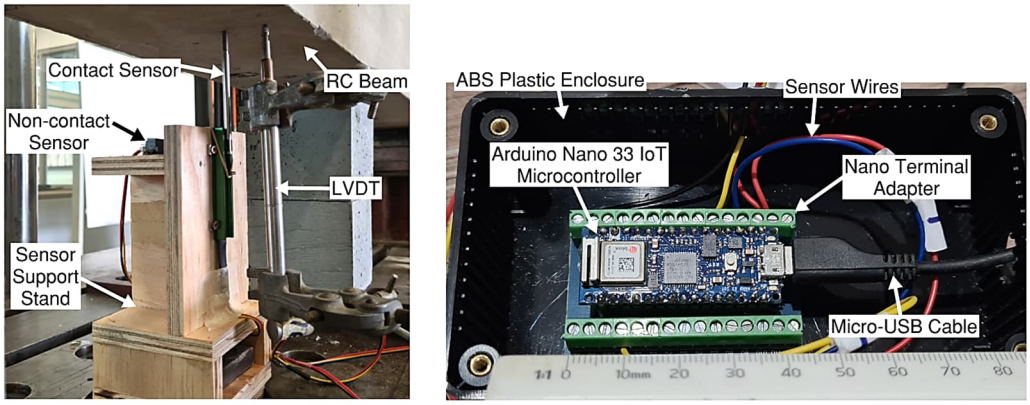

Figure 3-19: Sensor assembly: (a) Displacement sensor support stand, and (b) Arduino microcontroller connection within the enclosure

Given the low power consumption of the Arduino microcontroller and the displacement sensors, both power and communications were supplied via a micro-USB cable (5 V) connected to a laptop computer. The Arduino microcontroller's regulated power supply provided 3.3 V for the displacement sensors and received the displacement measurements from the monitored RC beam as analog voltage signals. These analog signals were digitised by the Arduino's internal ADC. During testing, the connected computer also served as a secondary backup device, locally recording the signal data.

Equipped with a built-in Wi-Fi module, the microcontroller could establish versatile wireless connectivity with a Wi-Fi wireless access point, whether through a mobile device's hotspot, or a conventional modem-router system. The module supports a connection range of 30 m to 100 m, depending on obstacles or signal interference present. This connection enabled the transmission and storage of the measurements to the Arduino IoT Cloud, a free-to-use cloud-based platform designed for monitoring, controlling, and automating IoT devices. Users could access this signal data remotely in real-time via an internet connection using a computer

browser or smartphone application. Additionally, the encrypted data transfer ensured secure communication for all connected devices.

3.7 SENSORS CALIBRATION

The integration of the sensors to the Arduino microcontroller facilitated the conversion of analog signals, generated from the detected physical displacements, into digital signals that could be processed by the electrical system (Figure 3-20). The Arduino Nano 33 IoT is equipped with a 10-bit ADC, which converts continuous analog voltage signals into a finite set of digital values ranging from 0 to 1023 ($2^{10} - 1$).

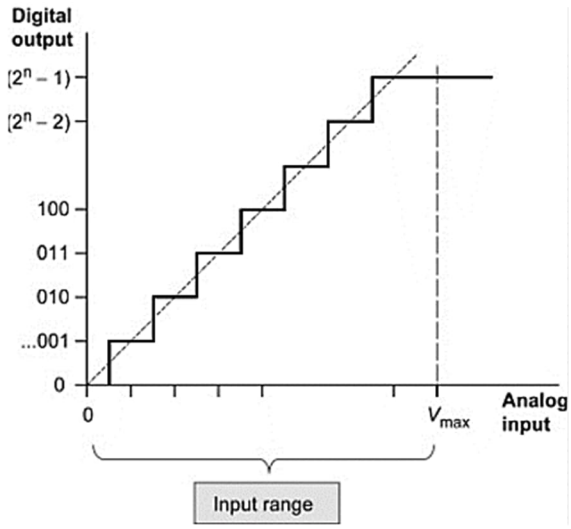

Figure 3-20: Relationship between continuous analog input signal and resulting output digital signal in discrete steps (Wilmshurst, 2010)

Due to the discrete nature of digital output steps, the resulting displacement values derived from these measurements exhibit a limited resolution. This characteristic, related to the resolution or sensitivity of the ADC, could be determined through the calibration of the sensors. Through calibration, the relationship between the analog input and the digital output could be established, allowing for the direct conversion of ADC digits into comprehensible displacement values.

Another important aspect of sensor calibration is ensuring their accuracy, reliability, and performance during operation. Various factors, including environmental conditions (temperature, humidity, lighting), surface characteristics of the monitored object (reflectivity,

colour, texture), electromagnetic interference, intrinsic noise and hysteresis can cause inaccuracies in distance sensing. In relation of the noise characteristic of the sensor, particular attention was placed on the IR sensor, which can be highly influenced by environmental effects related to the reflectance properties of the object's surface. This section discusses the calibration procedure, as well as the accuracy, hysteresis and noise characteristics of the contact and non-contact sensors.

3.7.1 Sampling Frequency

The Arduino microcontroller is programmed by creating a program, also referred to as a sketch, on Arduino's online IDE cloud platform. The sketch, written in Arduino's programming language (a modified C/C++ suite of development tools), specifies a set of instructions on how and when to measure signals connected to the Arduino's ADC, perform internal calculations and conversions, manage outputs, and communicate with other devices (computer or network). The sketch created for this study's application is presented in Appendix A.3. For each measurement of the sensors, 250 samples were recorded and averaged to substantially reduce the noise associated with the raw measurements. These averaged measurements for both the contact and non-contact sensors were transmitted to the connected computer via the USB communication port for local storage as a secondary backup. Ultimately, the combination of displacement measurements, code execution, and wireless transmission resulted in an average sample time of 2.6 seconds for both sensors, equivalent to a sampling frequency of 0.39 Hz. Given the temporal nature of the progressive three-point bending static load tests conducted, this sampling frequency was found to be adequate.

3.7.2 Displacement and ADC Digit

The calibration of the displacement sensors involved comparing the sensors' measurements against a calibrated control. The control displacements were applied using the digital height gauge manufactured by INSIZE (model 1151-300), which offers a resolution of 0.01 mm (10 μm). The height gauge features a driving wheel that allows for precise adjustments across various reference heights.

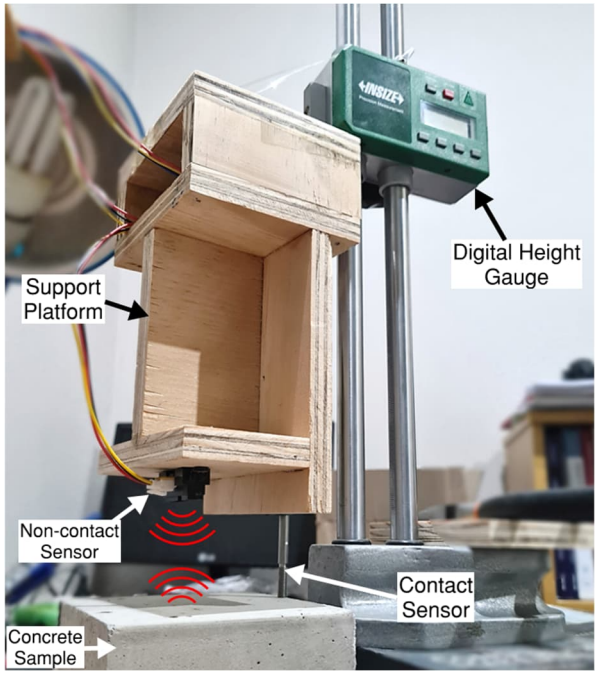

Figure 3-21: Contact and non-contact displacement sensor calibration setup

The mounting platform supporting the displacement sensors was attached to the arm of the height gauge. Beneath the suspended support platform, a concrete cube sample was positioned within the sensing area of both the potentiometer and IR sensors. As the arm shifted vertically, the sensors moved concurrently, simulating the vertical movement of the beam soffit during load testing. Both sensors were calibrated to the potentiometer's maximum extension range of 50 mm at an increment of 0.50 mm (50 µm). For each calibration increment, the corresponding output ADC digit was determined using an averaged value of 100 measurements.

The calibration results of the potentiometer contact sensor, illustrating the relationship between the displacement of the stroke rod from its fully-retracted position and the corresponding ADC digit output, are shown in Figure 3-22.

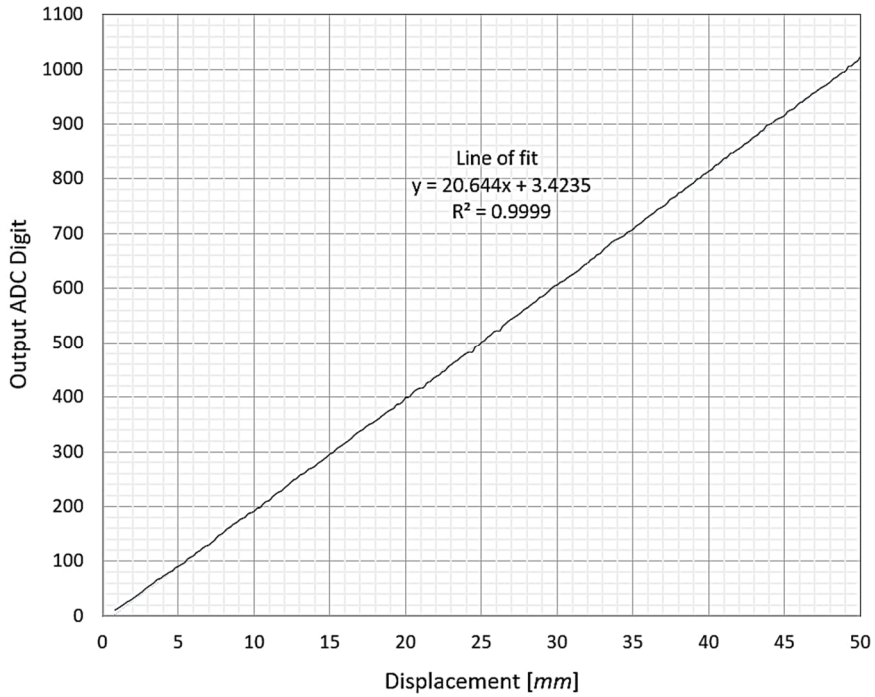

Figure 3-22: Calibration of the potentiometer contact sensor between displacement and output ADC digit

The plotted data illustrates a linear relationship between the applied displacement and the ADC digit output, demonstrating a high degree of linearity across the entire measurement range of the sensor. This relationship aligns with the working principle of a linear potentiometer and conforms to the manufacturer's specifications. The gradient of the line of fit is calculated to be 20.644 ADC digits per mm, which represents the resolution of the potentiometer. This resolution signifies the smallest discernible change quantifiable by an ADC digit, measured at 48.4 μm per ADC digit.

On the contrary, the IR non-contact sensor displayed a nonlinear correlation between the extended detection distance and the ADC digit output, as depicted in Figure 3-23. The nonlinearity can be represented by a line of fit resembling a quadratic polynomial function, which exhibits a steeper slope at shorter object detection distances and a shallower slope at greater distances.

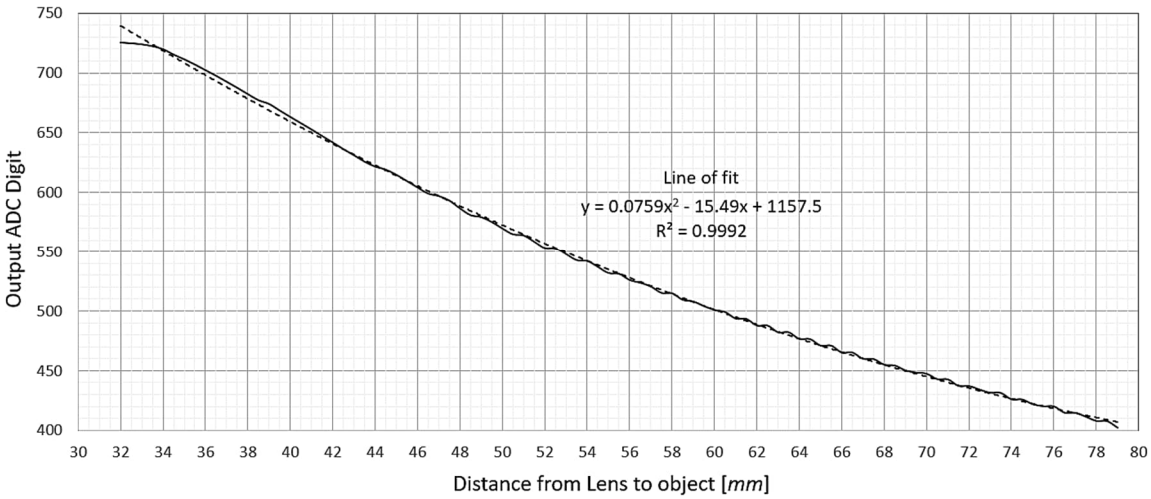

Figure 3-23: Calibration of the IR non-contact sensor between detection distance and output ADC digit

The nonlinear behaviour signifies a variation in resolution across the calibration range, as illustrated in Figure 3-24. Higher resolution (94.1 µm per ADC digit) was attained at closer ranges, while a lower resolution (285.9 µm per ADC digit) was observed for an increased separation distance.

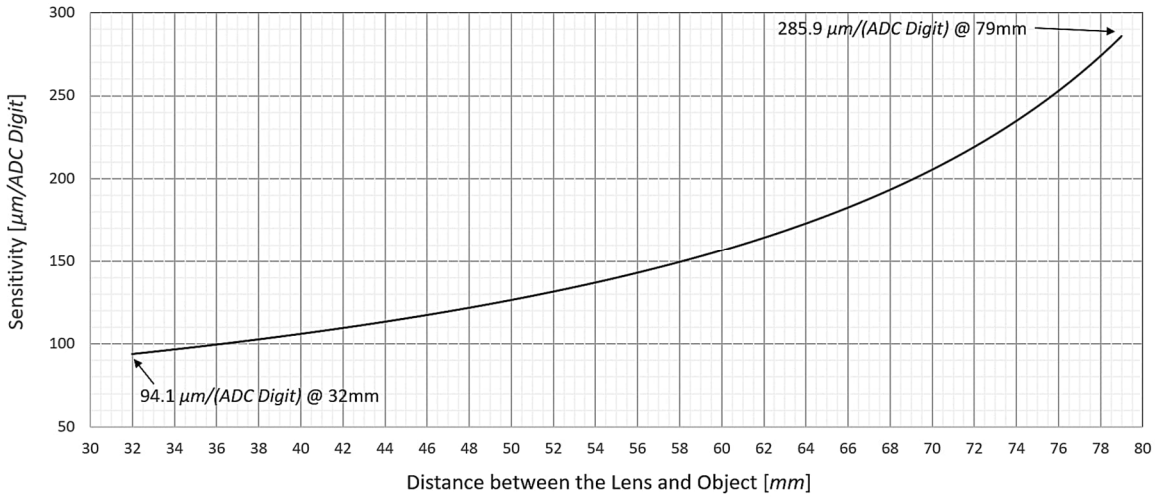

Figure 3-24: Calibration of the IR non-contact sensor between detection distance and sensitivity (resolution)

3.7.3 Accuracy and Hysteresis

The accuracy of both contact and non-contact sensors was preliminary estimated by repeatedly sampling sensor displacements at four distinct reference measurement points using the height gauge through a series of increasing and decreasing distance cycles. At each reference displacement point, three sensor displacement values were recorded (Appendix A.4). Due to inherent errors, these values exhibited some scattering around the reference value. To quantify accuracy, a linear regression line was fitted through the scattered data while ensuring the deviation between the two most extreme points above and below the regression line was equal. By applying this approximated method, the averaged accuracies were quantified to be ±80 μm for the potentiometer sensor, corresponding to 0.26% of the reference value, and ±363 μm for the IR sensor, equivalent to 1.63% of the reference value. The calibration results indicated that the potentiometer sensor demonstrated better performance in terms of resolution and accuracy compared to the IR sensor. This difference in performance is also reflected in the cost, as the potentiometer is more expensive than the IR sensor.

Using the same measurement data obtained to determine the sensor accuracy, the hysteresis of the potentiometer contact sensor was quantified. A simplified approach was followed, wherein hysteresis was calculated by determining the maximum absolute differences between the increasing and decreasing distance measurements at each applied reference displacement point. With this method, the average absolute measurement difference was estimated to be ±33 μm, with a hysteresis of 0.11% relative to the total sampling extension length for the potentiometer (Appendix A.5). The hysteresis result signifies a minor nonlinearity in the potentiometer's response, which influences its measurement accuracy. Due to the highly complex and variable nature in the IR sensor's measurement, its hysteresis behaviour was not investigated in this study.

3.7.4 Noise Characteristics

The operation of the sensor devices can produce fluctuating ADC digit outputs, even when no physical changes are applied to the displacement sensors. This phenomenon is primarily attributed to noise, which can arise from several sources. Electrical noise in the system, including electromagnetic interference, power supply voltage fluctuations, and thermal noise, can cause minor variations in the analog signal. The magnitude of the noise can influence the attainable degree of accuracy. To assess the noise characteristics of both contact and non-contact sensors, a calibration test was conducted. This involved sampling of 1000 ADC

digits at a rate of 0.39 Hz at various reference displacement points for each respective displacement sensor.

In the calibration of the contact sensor, ADC digit samples were measured at three reference extension lengths of the potentiometer, as graphically shown in Appendix A.6.1. The calculated statistical parameters are summarised in Table 3-3. The low standard deviation and coefficient of variance values across all extensions indicate high precision and reliability in the measurements. Consequently, the potentiometer sensor produces highly consistent readings with minimal noise characteristics.

Table 3-3: Statistical results of potentiometer's output ADC digit at various reference extension lengths (1000 samples)

Parameters	Reference Potentiometer Extension Length		
	Short Extension	Middle Extension	Long Extension
Target ADC Digit	300.00	600.00	900.00
Minimum Value	299.00	599.00	899.00
Maximum Value	301.00	601.00	901.00
Mode	300.00	600.00	900.00
Mean	300.010	600.019	899.997
Standard Deviation	209.6×10^{-3}	157.0×10^{-3}	164.4×10^{-3}
Coefficient of Variance	0.699×10^{-3}	0.262×10^{-3}	0.183×10^{-3}

The noise calibration of the non-contact sensor involved sampling the ADC digits under various test conditions at four reference measurement distances. The test conditions simulated different reflectivity, absorption, and interference characteristics to demonstrate their influence on the IR sensor's performance in surface monitoring. The monitoring conditions include:

- A normal concrete surface in a well-lit room
- A concrete surface painted with acrylic white paint in a well-lit room
- A concrete surface painted with matte black paint in a well-lit room
- A normal concrete surface in a dark room without light

The comprehensive statistical results are presented in Appendix A.6.2. The resulting standard deviations for the various monitoring conditions are graphically provided in Figure 3-25.

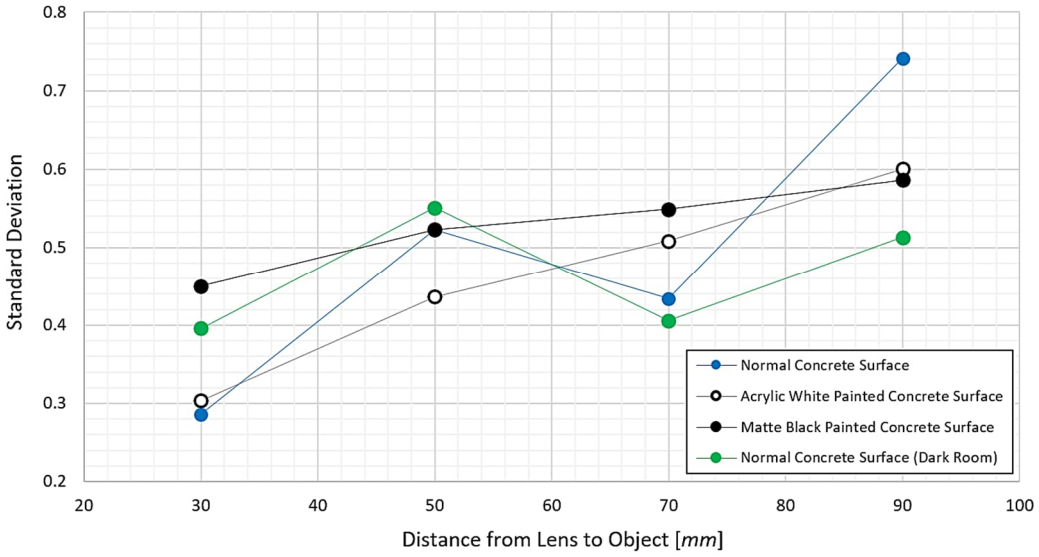

Figure 3-25: Standard deviations of IR sensor ADC digits under various test conditions and reference distances

Measuring the concrete surface coated with acrylic white paint yielded a lower standard deviation, particularly at closer object distances of 30 mm to 50 mm from the IR sensor. This reduction in data dispersion can be attributed to the higher reflectance nature of the white paint, leading to stronger infrared light reflection back to the sensor, thereby reducing the level of noise. Conversely, the matte black paint finish on the concrete surface exhibited a higher level of IR signal dispersion, notably at closer detection distances. Due to the paint's lower reflectivity and higher absorption of IR light, increased noise levels were noted. However, this effect was less prominent at longer measuring distances from the IR sensor. These reflectivity characteristics are corroborated by observations from a comprehensive spectroscopy experimental study performed on a LiDAR sensor by Hawley & Gräbe (2021). In this controlled laboratory test, detection targets with varying colours, and surface textures were scanned. The results showed that white-coloured targets exhibited the highest reflectivity due to their dominant high reflectance component, while black-coloured targets absorbed more light, i.e. reflected less. Furthermore, across various colours, rough surfaces were found to scatter incident light more evenly, thereby reducing the magnitude of backscattered energy compared to smooth surfaces.

Under the monitoring condition of a normal concrete surface in a dark room without light, the dispersion of infrared light signals was notably lower compared to tests conducted in well-lit environments, particularly at distances between 70 mm and 90 mm. The absence of ambient light reduced interference, enhancing the IR sensor's sensitivity to reflected IR signals from the

surface. This effect was less significant at shorter detection distances, where the shorter travel path of IR light reduced the impact of interference. Across all test conditions, there was a common trend of increased dispersion of IR light signals with greater object distances from the lens.

Overall, the noise calibration experiment demonstrated that the potentiometer exhibited higher precision and accuracy compared to the IR sensor. The potentiometer consistently provided accurate displacement measurements throughout its entire extendable range and showed minimal susceptibility to noise. Conversely, the inherent noise characteristics of the IR sensor may limit its accuracy at greater detection distances, indicating a higher probability of inaccuracies in measuring minor vertical displacements of the RC beam under smaller point loads. Nevertheless, as the RC beam further displaces vertically downward, reducing the detection distance to the IR sensor, noise levels are expected to diminish, resulting in more accurate and reliable measurements.

3.8 PROPOSED SOFTWARE SYSTEM

The software system, in conjunction with the hardware system, plays a pivotal role in realising the DT-enhanced SHM framework proposed in this research study. Serving as an integrated element, it establishes a synchronised loop between the physical asset and the digitally twined model. Utilising the retrieved sensor displacement data, the software system dynamically replicates the mechanical behaviour of the monitored beam and conducts structural analysis to predict its mechanical response. These post-processed data are then employed for damage diagnosis, providing early warnings and preventive actions to the user in an interactive and timely manner. This enables asset managers to make well-informed decisions regarding their structural assets, promoting an automated and intelligent SHM strategy.

To achieve the objective of implementing an adaptable DT-based SHM system suitable for small-scale applications that is more accessible, practical, and cost-effective, the software system was developed with the following objectives:

- Relatively straightforward post-processing procedures comprising uncomplicated model-based FE analysis, eliminating the need for complex setups and computing power, while not compromising the accuracy of the predicted result
- Capability to calibrate the DT model using empirical load test data
- Highly interactive and interpretable user interface
- Ability to provide a damage diagnostic report on possible structural damage sustained

The development of various components of the software system to fulfil these requirements is discussed in detail in Section 3.8.1.

3.8.1 FE-Based Digital Model

The DT aimed to replicate the mechanical response of the mid-span force-displacement relationship under three-point bending of the monitored RC beam. This replication was achieved through a model-based approach, utilising a numerical FE model to simulate the geometry, material properties, boundary conditions, and loading of the experimental RC beam specimen.

As the initial step in creating the DT, a baseline FE model acting as the preliminary, uncalibrated DT was created using *FEMAP* (Siemens, 2023), a simulation FE software program designed for both pre- and post-processing of complex engineering numerical models. *FEMAP* facilitated the replication of essential features of the monitored RC beam, including its geometry, concrete and reinforcing steel properties, supporting conditions, and applied loading or imposed displacements. The data developed for the baseline model was exported to a *FEMAP* neutral file, which can be interpreted by numerical and alphabetical characters that are readable as a text file and compatible with *ReConAn* (Mourlas & Markou, 2020). Following the analysis in *ReConAn*, the built-in post-processing window, *ReConAn Eye* is automatically initialised to visualise and animate concrete beam cracking and deformation in 3D. Additionally, the analysis results could optionally be imported back into *FEMAP* for post-processing visualisations of beam model deformation and contour plotting of stress and strain. Due to *FEMAP*'s limitation of being unable to illustrate cracks at FE nodal points, *ReConAn Eye* was utilised to provide a graphical representation of the estimated 3D cracks for the user.

Structural analysis of the FE model was conducted using *ReConAn* (Mourlas & Markou, 2020), a RC FE analysis software renowned for its ability to handle advanced numerical methods and sophisticated material modelling with complex nonlinear characteristics. Developed with an intelligent, object-oriented programming technique, *ReConAn* operates efficiently on commercial computers with standard CPU performance while delivering precise simulation results of RC structures. Unlike software that requires specific file formats, the software was designed to read FE model input, and export analysis output data in a text file format, significantly enhancing its universality. This format allows the data to be shared by a wide range of software applications on various operating systems, making it highly compatible and accessible. Furthermore, *ReConAn* features *ReConAn Eye*, an extended post-processing user

interface that allows the visualisation and animation of the predicted concrete crack formations, providing further insight into the structural behaviour of the analysed RC members.

The abovementioned FE processing procedures, as well as the related file type and software utilised, are depicted in Figure 3-26.

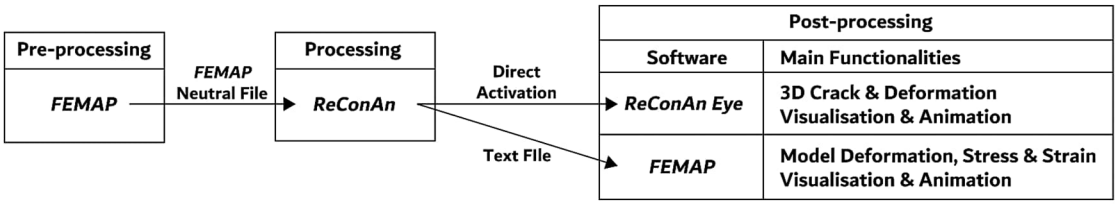

Figure 3-26: FE processing procedures, file type and software employed for the software system's digital twin

The FE baseline model in this study was developed in *FEMAP* and simulated the beam specimen described in Chapter 3.3.1 (Figure 3-27). Necessary components of the FE model were developed, each characterised by specific geometric, material, and loading properties and assumptions outlined below:

- Concrete Beam:
  - Modelled using isoparametric hexahedral 20-noded FE solid elements
  - Material model: smeared crack approach utilising the modified Kotsovos & Pavlovic model as proposed by Markou (2011) and Markou & Papadrakakis (2010).
  - Nonlinearity type: Elasto-Plastic. Hardening parameter was set to 0 GPa
  - Remaining shear factor: assumed at 5% to account for interlocking friction action between aggregates
  - Tensile strength was assumed to be 5% of its uniaxial compressive strength
  - Elastic limit of 50%. This threshold defines the point at which concrete transitions from elastic behaviour, triggering stiffness degradation in the material model.
- Reinforcing Bars (longitudinal and transverse):
  - Represented as rod elements with circular sections
  - Bilinear steel material model
  - Steel failure strain was assumed to be 10%
- Boundary Conditions:
  - Modelled as a metallic plate composed of hexahedral 20-noded FE solid elements

  - Metallic plate nodal points coincide with support roller positions to prevent premature local failure (the end nodes were set to simulate the simply supported condition according to the beam test configuration)

- Loading:
  - Mid-span load was proportionally distributed amongst the 5 central nodes. In imposed-displacement analysis, the same displacement value was assigned to the same 5 nodes
  - Calibration process utilised the displacement-controlled Newton-Raphson method
  - External imposed displacement with 50 increments
  - Number of maximum internal iterations was set to 100

The Kotsovos and Pavlovic (1995) model is a three-dimensional constitutive material model designed to simulate the nonlinear behaviour of concrete under various loading conditions. It effectively captures the complex stress-strain relationships characteristic of concrete, including phenomena such as microcracking and macrocracking. The model considers cracking to occur when shear failure takes place and, simultaneously, at least one of the principal stresses is in tension. In such cases, a crack is introduced, and the tensile strength at that point is immediately reduced to zero, ensuring realistic numerical predictions.

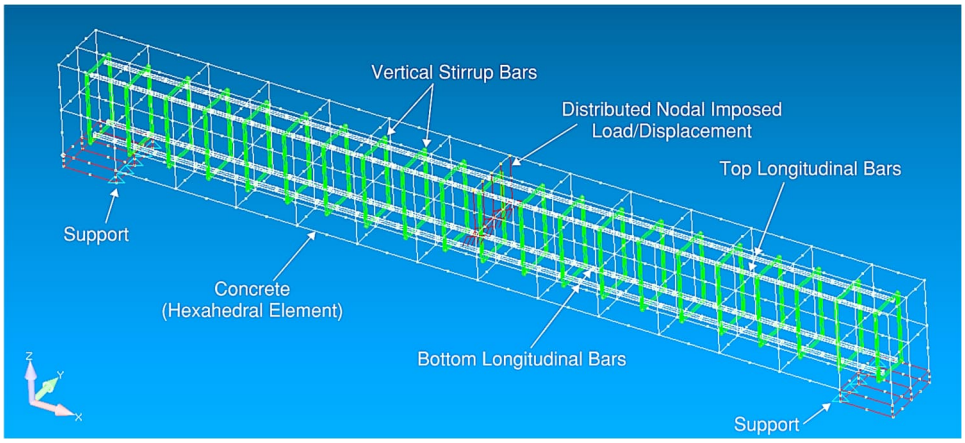

Figure 3-27: FE baseline model developed in *FEMAP*

The FE baseline model was exported to a *FEMAP* neutral file (with a file size of less than 100 KB) for subsequent processing. The numerical model was created to closely resemble the physical beam, aiming to yield an accurate estimation of the mechanical response of the beam specimen. Though the development of the FE model may seem intricate, it is important to note that this is a pre-processing task required only to be performed once in the implementation of the DT-SHM framework. Manual and repetitive updates of the model during the calibration process of the DT are not required.

3.8.2 DT Calibration

Following the creation of the baseline FE model, calibration using the load test results was imperative to achieve a DT with a higher degree of accuracy and reliability in predicting the mid-span force-displacement behaviour of the experimental beam specimen. The calibration of DT is widely recognised by numerous researchers as a critical procedure for validating and updating the FE model in a DT framework.

In a DT-enhanced SHM experiment conducted on a real-life single-span concrete bridge by Jasinkski *et al*. (2023), the bridge span was subjected to non-destructive static and dynamic loadings from loaded trucks with known masses. Mechanical sensors and levelling tools captured the resulting vertical deflections and frequencies, which were then utilised to assess the structure's response. This information served to iteratively calibrate the DT, thereby producing a more accurate representation of the bridge's behaviour.

To meet the requirements of this research study, the DT was calibrated using the results obtained from Load Test Stage 1, as detailed in Chapter 3.3.1. By leveraging the tested, averaged force-displacement mechanical response, the baseline FE numerical model could be iteratively adjusted to mirror the same relationship, with the objective to reproduce a realistic simulation of the RC beam mechanical behaviour. Provided that the beam specimens in both Load Test Stages shared identical geometry, material type, reinforcing, and test configurations, the calibrated DT was utilised to predict the mechanical response of the beam specimen with a high level of confidence in Load Test Stage 2.

Despite efforts to create a baseline FE model replicating all features and characteristics of its physical beam counterpart, the force-displacement relationship would not be identical. The discrepancy could be attributed to several factors, including the material properties of concrete and reinforcement (especially those influenced by environmental conditions and time), construction quality, physical imperfections, and slight variations in experimental setups. However, provided that the RC beam specimens were prepared in a laboratory environment where quality and testing could be readily controlled, the force-displacement behaviour was identified to be primarily influenced by the following three material properties:

- Young's modulus of concrete
- Young's modulus of reinforcing steel
- Yield stress of reinforcing steel

These properties were subsequently selected as the varying parameters in the iterative calibration process of the DT model. The calibration process involved the iterative analysis of

the FE numerical model with all possible combinations of the three concrete and reinforcing material properties, as shown in Figure 3-28. The DT corresponds to the force-displacement response that most closely resembles the load test result. This served as a simplified approach in calibrating the DT, enabling a realistic and reliable simulation of the RC beam behaviour.

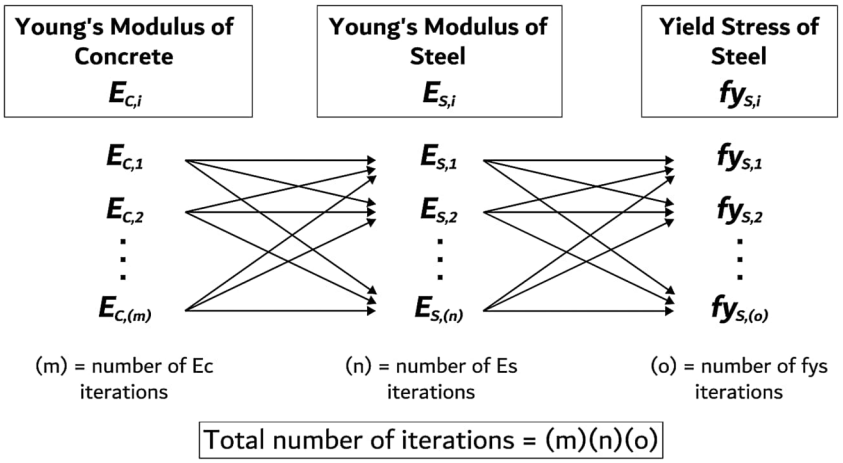

Figure 3-28: Analysis iteration with variations of concrete and reinforcing steel material properties

As each material property possesses its own individual number of iterations specified by the user, the total number of iterations encompassing all possible combinations is the product of all individual iterations. Increasing the total number of iterations would increase the probability of finding a closer matching iteration but would also increase the analysis time. Therefore, the iteration ranges and increments of the material properties specified by the user would have to be within reasonable ranges of assumption based on material sample test results (such as compressive cube strength) and sound judgements.

3.8.3 ReConTwin

To fully realise the DT-incorporated SHM framework in this study, the software program ReConTwin was developed. Featuring automation and user-friendly interfaces, ReConTwin serves as an indispensable component that enhances the functionalities of the software system. These features enable a seamless flow of information and promote high interactivity between the digital model and the asset management team. Achieving these functionalities was made possible through the application of Visual Studio Code (VSC, 2024), a streamlined code editor

that is free for private and commercial applications and tailored for software development. VSC supports a wide array of programming languages and provides a robust platform for editing, debugging, and efficiently managing software codes. Its flexibility allows for ease of code modification, enabling the software to adapt to evolving project requirements in the future.

Utilising Python, a popular and versatile script-based, interpreted programming language, automation was central in ReConTwin's calibration process of the DT to streamline repetitive tasks and manual processes. Python scripts were created for ReConTwin to automate each repetitive aspect of the iterative procedure as illustrated in Figure 3-29:

- In replacement of using *FEMAP* to manually update the selected material property combination of the DT, ReConTwin directly modifies the material property parameters within the baseline FE model neutral file (.NEU).
- Subsequently, ReConTwin autonomously activates *ReConAn* to perform a displacement-controlled FE analysis based on the instructions contained within the neutral file. The desired imposed displacement can be selected by the user based on the recorded live displacement readings according to the input obtained from the Arduino Cloud. Upon completion, the *ReConAn* exports the analysis results to a text file.
- In the next step, the ReConTwin extracts the back-calculated vertical total load and, along with the specified displacement increments, stores this information as a force-displacement iteration entry in a Microsoft (MS) Excel result file. During this step, the relative error of each iteration is calculated and recorded. The aforementioned processes are repeated by the ReConTwin until all iterations are complete.
- After completion of all iterations, ReConTwin determines the most accurate iteration with the smallest error and designates it as the DT model that best simulates the mechanical response of the RC beam.

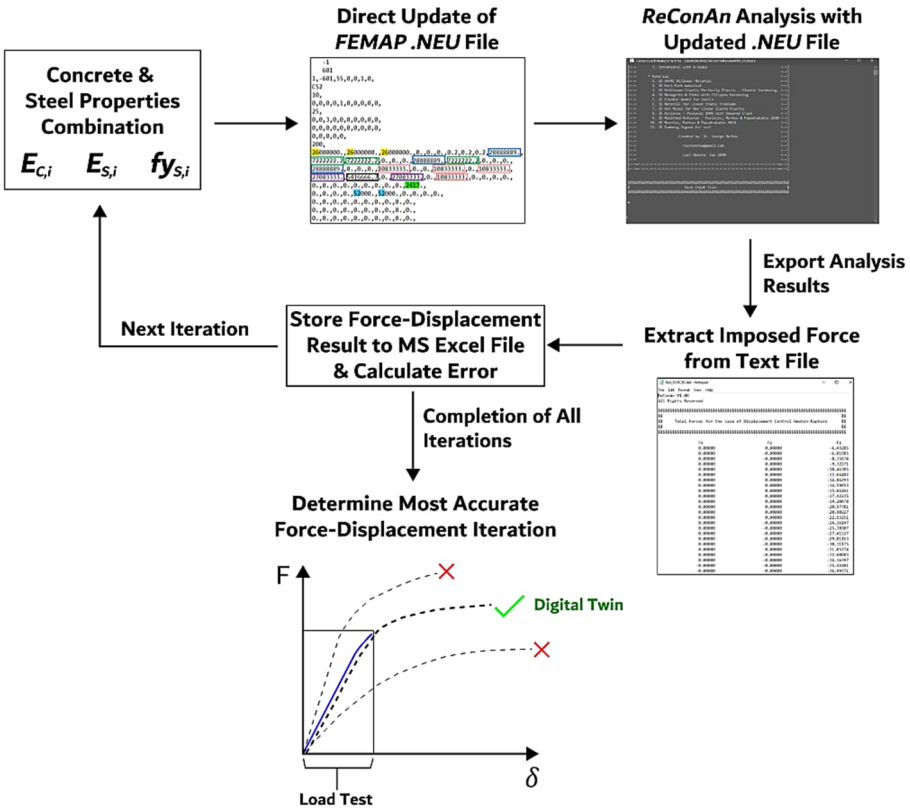

Figure 3-29: ReConTwin's automated calibration process of the DT to the load test results developed using the Python code

In addition to automation, ReConTwin was developed using Python-based scripts to create user-friendly interfaces, facilitating intuitive user interaction with the software system. Tkinter, a popular Python library, was employed to create the Graphical User Interface (GUI) for ReConTwin. Figure 3-30 shows the collection of GUI windows developed for visually and graphically illustrating the input and output data generated by the proposed SHM framework.

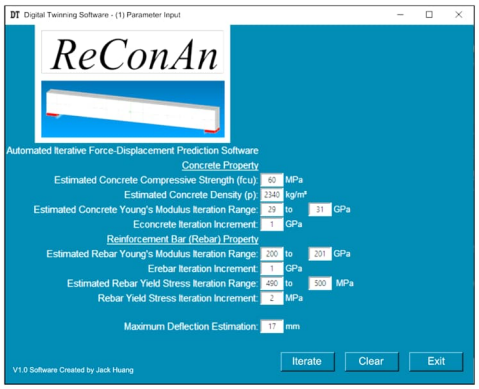

GUI Window 1

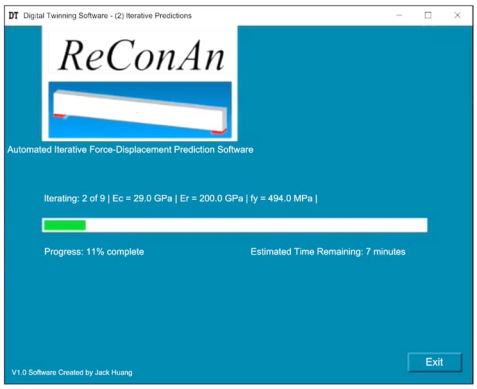

GUI Window 2

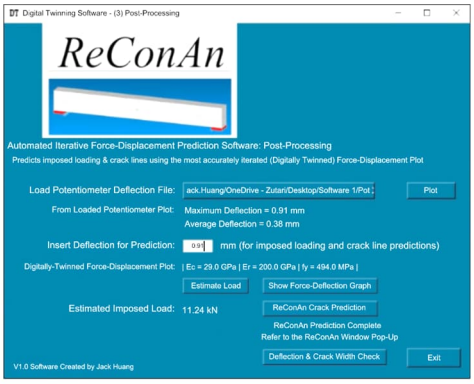

GUI Window 3

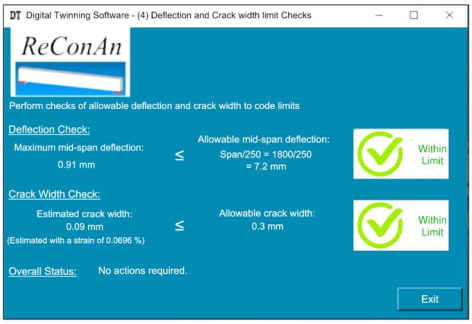

GUI Window 4

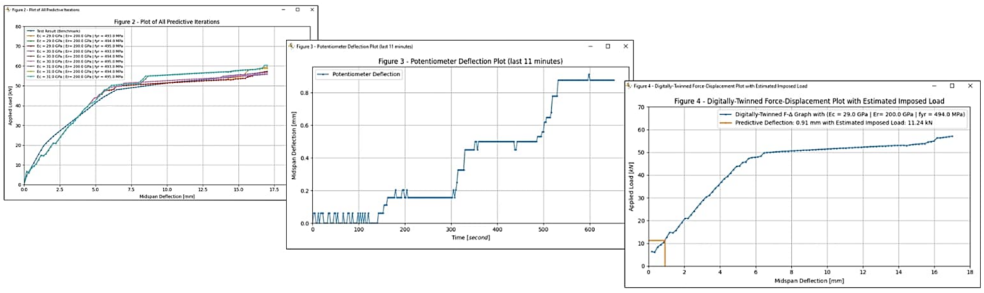

Graphical Plot of GUI Window 3 Output Data

Figure 3-30: Collection of GUI windows and graphical plot of data generated by ReConTwin

Four interdependent GUI windows were designed, enabling the user to specify the preferred input parameters, automate tasks, and navigate through ReConTwin using graphical elements such as input fields, buttons, and display plots (Huang & Markou, 2024). The purpose of each window and their associated features are discussed in detail in Appendix A.7. These four windows include:

- GUI Window 1 – Parameter input window: Allows the user to define input parameters of the DT calibration process, including concrete compressive strength, density, reinforcing and concrete material properties, and deflection limits.

- GUI Window 2 – DT calibration window: Displays the calibration procedure's progress, enabling the user to review prediction results and select the most accurate material property iteration set as the DT.
- GUI Window 3 – Post-processing window: Enables users to incorporate sensor data, predict the force-displacement behaviour of the monitored RC beam, plot sensor displacement data, estimate imposed load, and predict crack formation.
- GUI Window 4 – Damage diagnosis window: Automates damage diagnosis based on structural performance indicators relating to the allowable beam deflection and crack width limits. It then provides the user with a warning for necessary preventive actions.

The integration of ReConTwin's automation feature, streamlines processes and enhances efficiency, while the designed GUI windows offer intuitive interaction. This allows users to navigate seamlessly through a more efficient, transparent, and user-friendly software system, holistically controlling the developed DT-SHM framework.

3.8.4 Damage Diagnosis

In the final stage of completing the automated information synchronisation between the DT model and its physical RC beam counterpart, the proposed ReConTwin incorporates a damage diagnosis functionality (GUI Window 4). This feature assesses the structural condition of the monitored RC beam and provides an early warning to the user in the case that it is not performing within the expected criteria. The damage diagnosis for the proposed DT-SHM framework is achieved by evaluating two key structural performance indicators:

- Mid-span deflection limit – ReConTwin verifies whether the user-specified deflection value, based on imported sensor data in GUI Window 3, is within the code-based limit of beam span to deflection ratio of 250 (or other user-defined limit).
- Crack width limit – The estimated crack width, determined using the estimated beam soffit strain (predicted from the *ReConAn* analysis using the specified deflection value based on live sensor measurements) is compared against the code-based limit of 0.3 mm (or other user-preferred limit value).

If either performance indicator exceeds the specified limit, ReConTwin will generate a warning, indicating the need for preventive actions to be taken by the user. This automated process aids in promptly identifying potential structural issues and the requisite preventive actions, thereby enhancing the reliability and safety of the monitored structure.

It is essential to highlight that the integration of *ReConAn* and 3D detailed modelling facilitates a comprehensive evaluation of the monitored RC structure. This advanced modelling capability allows users to anticipate not only superficial crack formation but also internal damage within the RC domain. Such depth of analysis provides a significant advantage over many SHM systems discussed in most international literature, which often do not offer insights into internal structural integrity.

3.8.5 Proposed Software System Overview

The overview of the developed software system (complimented by ReConTwin) which forms part of the developed DT-SHM framework, detailing its components, processes, and the automated flow of information outlined in Chapter 3.8, is illustrated in Figure 3-31.

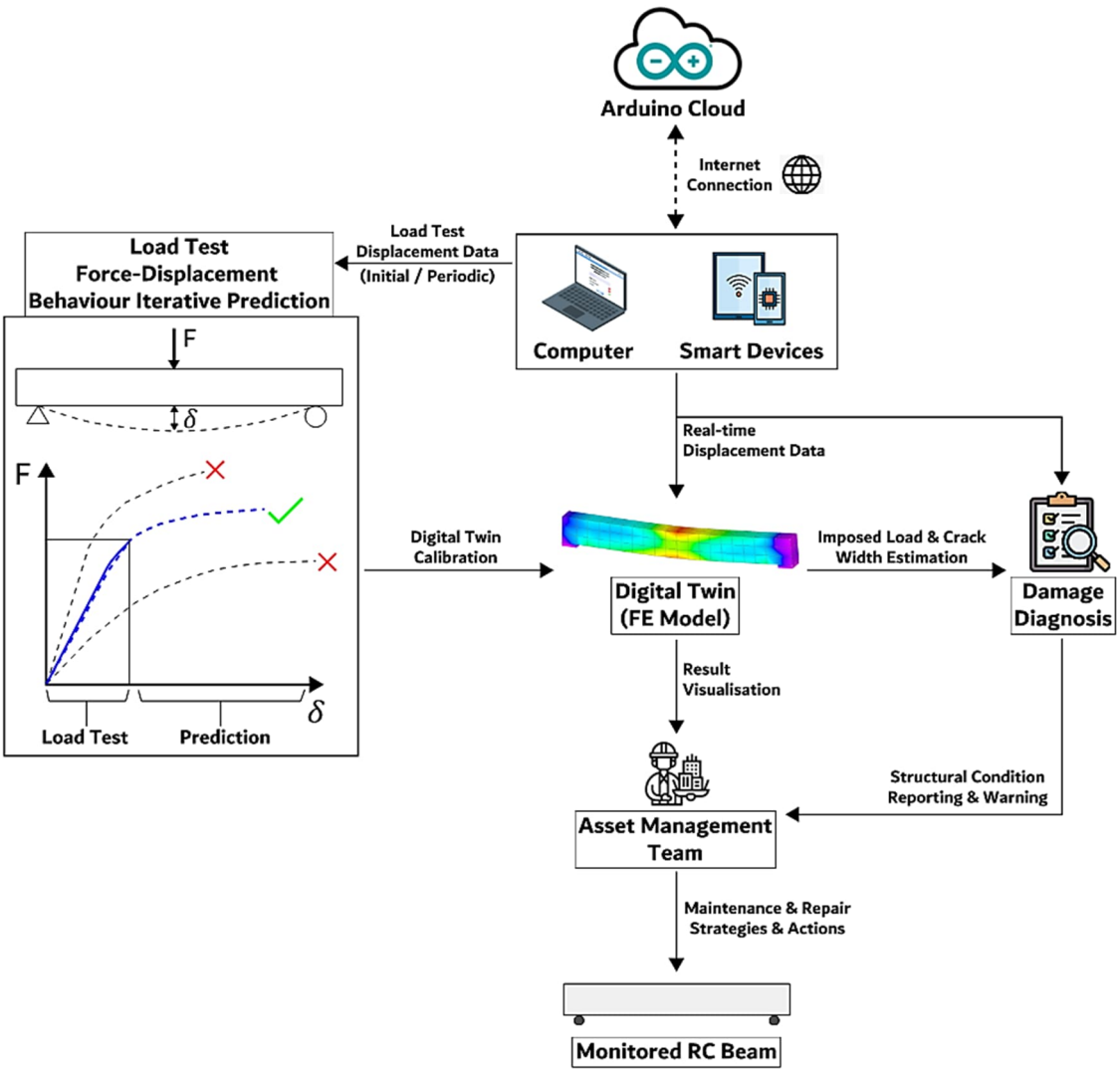

Figure 3-31: Software system overview

Following the transfer of real-time beam displacement sensor data to the Arduino IoT Cloud from the hardware system, as depicted in Figure 3-18, the user can retrieve these data from the cloud via a computer or smart device. The displacement data are then imported into ReConTwin and utilised in the analysis of the FE DT model to predict the vertical load imposed on the RC beam and the beam soffit crack width for damage diagnosis in the case of crack openings.

The software system is equipped with the capability to calibrate the FE numerical model preliminarily or periodically, ensuring the generation of a reliable DT. With the effective integration of the Python script, the repetitive process in the iterative predictive analysis procedure is automated by ReConTwin, simulating the force-displacement behaviour based on the load test results with minimal human intervention. The resulting damage diagnostic report outlines the structural condition and performance of the RC beam, along with the estimated applied load and numerically predicted cracks. These results can then be examined by the asset management team to gain insights into the structural performance and condition of the beam, predict potential damages, and take preventive actions in maintaining the infrastructure asset, thereby fully realising the DT-enhanced SHM framework.

3.9 DISCUSSION

The proposed DT-based SHM framework developed in this study aims to provide a practical and cost-effective solution for health monitoring of civil infrastructure. It comprises the hardware and software core systems that facilitate automated data transfer between the physical entity and its virtual model, enabling smart monitoring of structural behaviour utilising the DT concept. Although the proposed framework is specifically designed for monitoring a RC beam, its underlying principles are versatile and can be easily adapted and implemented for real-scale structures.

By leveraging the affordable IoT-enhanced displacement smart sensors, comprising inexpensive sensors and wireless communication device, real-time beam deflection data is wirelessly transmitted to cloud storage, allowing for remote access. This data is incorporated into the developed software system, which employs a simplified post-processing approach using an FE-based DT numerical model. The developed software system, reinforced with ReConTwin, provides automated and user-intuitive functionalities, enabling near real-time model analysis, calibration, mechanical response estimation, and damage diagnosis without the need for specialised knowledge or demanding computing requirements. The two core systems synergistically complement each other to digitally replicate the mechanical behaviour of a RC beam, demonstrating the feasibility of a practical, adaptable, and efficient DT-based SHM

approach. This empowers the asset managers to make well-informed decisions regarding infrastructure maintenance and safety.

The developed DT-SHM framework was applied and tested in the experimentation of the RC beam specimen conducted under Load Test Stage 2 as described in Chapter 3.3.1, with the derived results presented in Chapter 4.

4 EXPERIMENTAL WORK AND RESULTS

In this chapter, the experimental results of the RC beam specimens under three-point bending Load Tests Stage 1 and 2 are presented and compared to the recorded data derived by the developed smart sensor platform. Additionally, the calibration process and outcomes of the DT FE model, verified using the Load Test Stage 1 results are presented. The accuracy of the calibrated DT in estimating the concrete strain for crack width estimation is evaluated. Overall, the performance of the developed DT-SHM framework is assessed and discussed in this chapter.

4.1 LOAD TEST STAGE 1

In the first stage of the loading test, four RC beam specimens were subjected to a three-point loading test as outlined in Chapter 3.3.1. One of the four RC beam specimens is shown in Figure 4-1. An incremental static load in the order of 4 kN was applied at a rate of 4 kN per minute and maintained for three minutes per load step until beam failure. An averaged displacement measured from the load-maintaining stage for each beam specimen was calculated as the corresponding displacement for each load step.

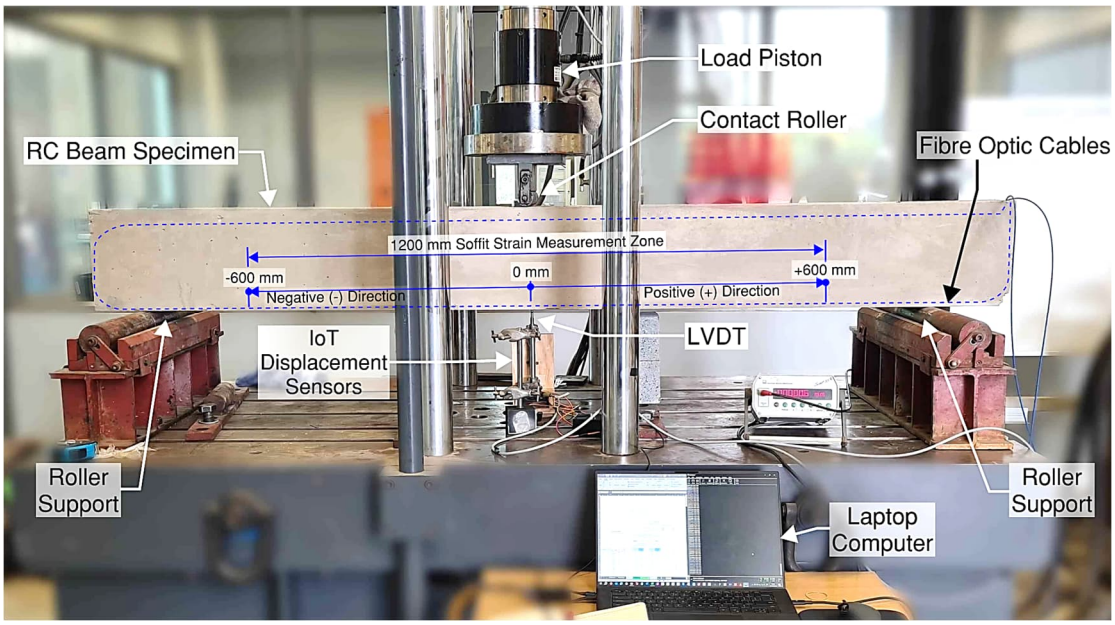

Figure 4-1: Typical three-point bending test of the RC beam specimen (Load Test Stage 1)

Each beam specimen was tested to failure, with the peak load step reaching 52 kN. The force-displacement relationship for each beam obtained from Load Test Stage 1, along with the calculated averaged force-displacement behaviour, are illustrated in Figure 4-2. A summary of the measured displacement statistics for all the beams is provided in Appendix A.8.

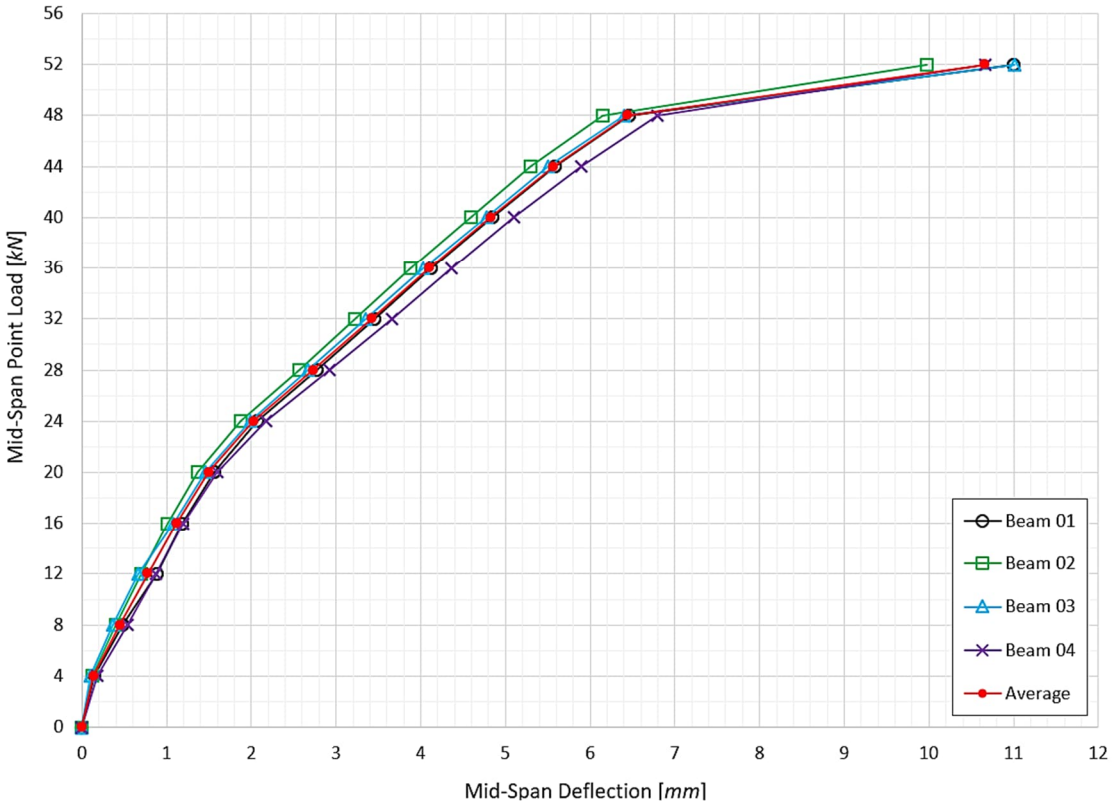

Figure 4-2: Force-displacement results at beam mid-span (Load Test Stage 1)

The standard deviation of the mid-span displacements, describing the measurement variability relative to the mean, increases with higher applied point loads. This suggests a more consistent mechanical response of the beam at lower load magnitudes and decreased consistency at higher load magnitudes are obtained. The measured displacements of the RC beam specimens under various applied point loads exhibit a consistent force-displacement behaviour, serving as reliable control data for calibrating the DT.

During each three-minute load-maintaining phase for each RC beam specimen, the fibre optic interrogator recorded tensile strain readings along the distributed fibre optic cable embedded along the beam's soffit surface. The effective strain reading range was 1200 mm, extending 600 mm on either side relative to the beam mid-span (0 mm reference position), as shown in Figure 4-1 (negative values indicate the left side, positive values the right side of the reference).

Strain readings were captured at 52 mm intervals along the beam length within the effective strain reading range, enabling the creation of a historical plot depicting the progressive strain growth profile along the bottom surface of the beam. Figure 4-3 shows a typical positive strain profile growth during the load test under the increasing applied loads. The distributed optic fibre strain plots for all four RC beam specimens are provided in Appendix A.9.

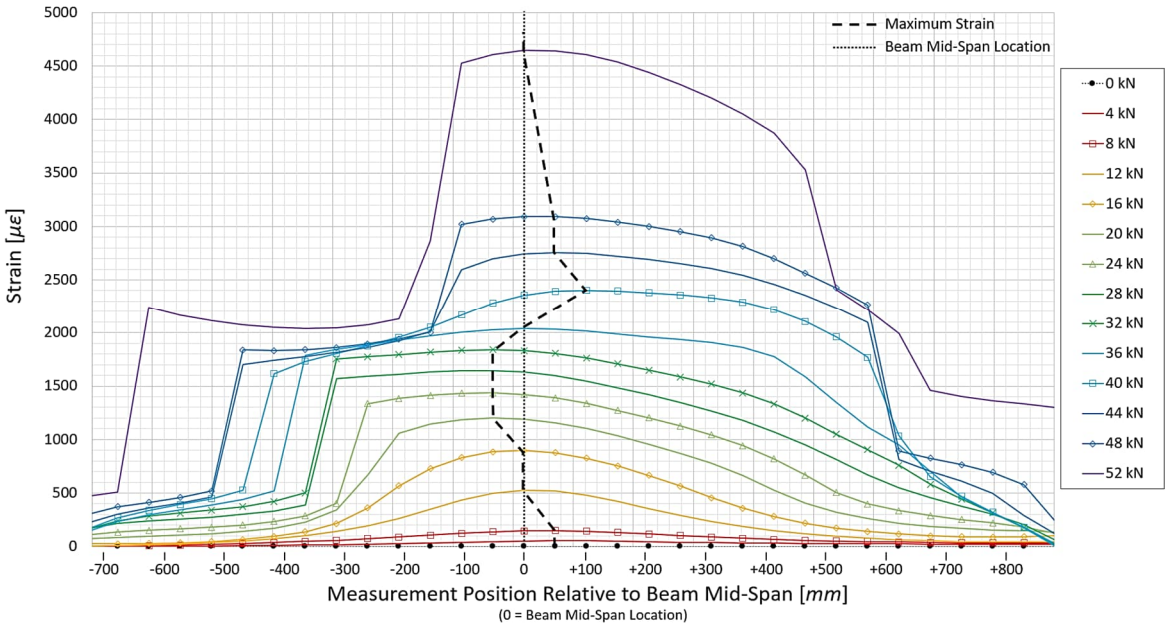

Figure 4-3: Typical distributed optic fibre strain profile along the beam soffit under increasing applied loads of Beam 1 (Load Test Stage 1)

The increase in the applied load led to a progressive rise in the positive tensile strain along the soffit surface of the RC beam specimen. Notably, the position of maximum strain, as shown by the interpolated black dash line in Figure 4-3, did not consistently align with the beam mid-span location. The maximum strain location varied along the beam length at each load increment, resulting in non-uniform distributions. The observed variation of the maximum strain location along the RC beam's soffit surface was attributed by complex nonlinear cracking mechanisms, material inhomogeneity, imperfect loading and support configurations, and construction imperfections. These factors collectively influence strain distribution, causing variations along the beam's length. However, the use of the distributed optic fibre allowed the identification of the largest tensile strain for each beam at every applied load step.

Table 4-1 presents the maximum positive strains measured along the soffit surface of each RC beam at every load step, together with the mean value obtained by averaging the maximum

strains for all beams at each load step. The averaged maximum strains were utilised for comparison with the strains predicted by the DT numerical model.

Table 4-1: Maximum beam soffit strain (Load Test Stage 1)

Applied Point Load	Beam Soffit Maximum Strain Measurement [με]				
	Beam 1	Beam 2	Beam 3	Beam 4	Average
0 kN	0	0	0	0	0
4 kN	54	52	46	47	50
8 kN	148	100	120	113	120
12 kN	525	273	257	284	335
16 kN	898	613	673	728	728
20 kN	1200	930	984	1178	1073
24 kN	1436	1180	1255	1491	1341
28 kN	1644	1434	1508	1722	1577
32 kN	1840	1689	1704	1917	1788
36 kN	2040	1951	1907	2136	2009
40 kN	2403	2202	2298	2374	2319
44 kN	2758	2467	2570	2685	2620
48 kN	3093	2730	2863	3048	2934
52 kN	4644	4308	4524	4603	4520

4.2 DT CALIBRATION

Using the average force-displacement results obtained from Load Test Stage 1 as a control, the FE numerical baseline model was calibrated to create a DT capable of reliably predicting the mechanical response of the beam specimen in Load Test Stage 2. The calibration process involved performing iterative structural analysis of the FE model with varying material properties to identify the combination that most closely resembled the load-displacement test data.

Prior to the calibration process, two primary groups of input vectors were specified: basic property and iterating material property. The basic property consists of non-varying properties that remained constant throughout all iterative FE analyses. Conversely, the iterating material property vector consist of the three main material properties pertaining to concrete and reinforcing steel that varied during the iterative process. These values were specified based on the concrete and reinforcing sample test result values obtained during both load test stages, as well as sound judgement. These vectors and their motivation for their selection are summarised below:

- Basic property input:
  - **Concrete compressive strength**: 56 MPa, calculated by averaging the compressive strengths of the concrete cube samples obtained during both test stages
  - **Concrete density**: 2378 kg/m³, based on the average densities of the cube samples obtained from both test stages
  - **Estimated maximum deflection**: 17 mm, conservatively chosen to capture the full force-displacement behaviour based on the final measurable deflection from Load Test Stage 1, which ranged between 9 mm and 11 mm
- Iterating material property input:
  - **Concrete - Young's Modulus**: Ranges from 26 GPa to 34 GPa with 1 GPa increments. The lower limit of 26 GPa was conservatively assumed, while the upper limit corresponded to the results obtained from Load Test Stage 2
  - **Reinforcing Steel - Young's Modulus**: A constant value of 200 GPa, based on the tested average modulus of elasticity results, and its consistency nature, was set to remain constant for all iterative analyses
  - **Reinforcing Steel - Yield Stress**: Ranges from 493 MPa to 500 MPa with 1 MPa increments. Lower limit was derived from the tensile test of the reinforcing sample, while the upper limit of 500 MPa was estimated based on sound judgement

These values were captured in ReConTwin through GUI Window 1 (the parameter input window, as seen in Figure 4-4). Prior to the iteration procedure, the average force-displacement results obtained from Load Test Stage 1 were stored in the MS Excel file format in which all iteration result and relative error outputs are recorded.

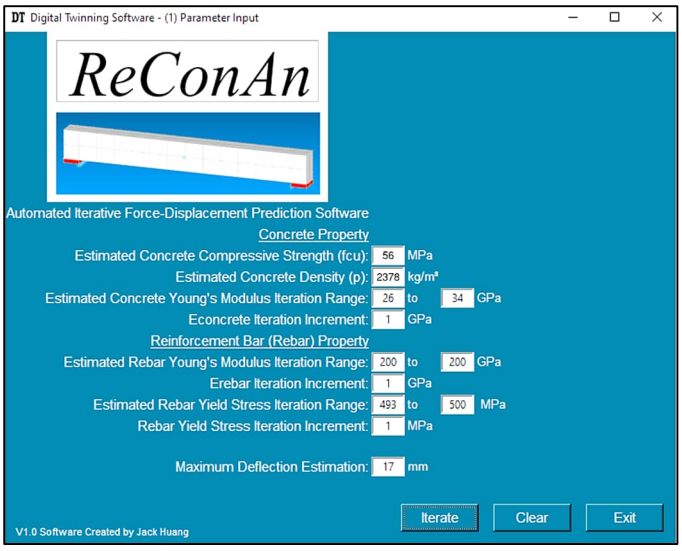

Figure 4-4: ReConTwin – GUI Window 1 – Populated parameter inputs for calibration

In initiating the calibration process by selecting the “Iterate” button, ReConTwin was prompted to commence the DT calibration procedure. This involved the automated and iterative update and analysis of the FE baseline model, covering all possible combinations of the three varying material properties specified. During this procedure, GUI Window 2 was automatically activated to display the iteration progress (Figure 4-5). This window provides feedback on the material property combination being analysed by *ReConAn* and informed the user of the estimated remaining time to complete all iteration processes.

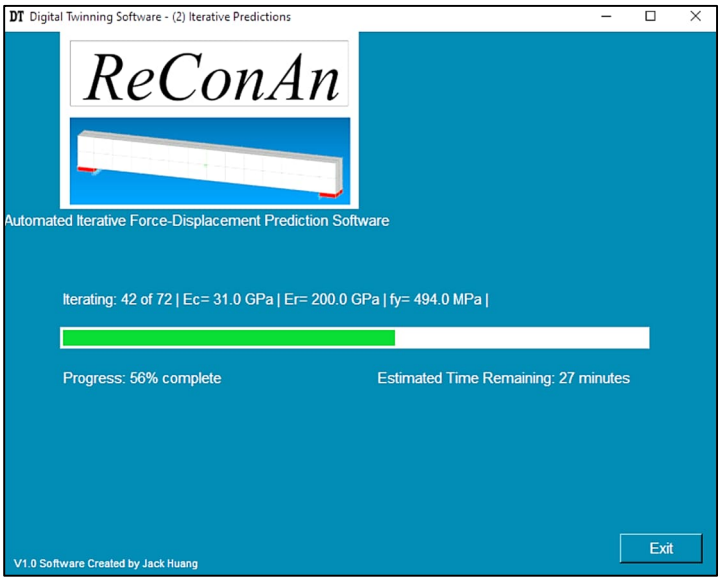

Figure 4-5: ReConTwin – GUI Window 2 – Calibration progress information display

With 9 possible increments for the concrete Young’s Modulus (ranging from 26 GPa to 34 GPa at 1 GPa step), 1 possible increment for the steel Young’s Modulus (set at 200 GPa), and 8 possible increments for the steel yield stress (ranging from 493 MPa to 500 MPa at 1 MPa step), the calibration process comprised a total 72 nonlinear analyses. This total was calculated as the product of all possible number increments. Each iteration required approximately 50 seconds to complete, yielding in a total calibration time of an hour. After each iterative analysis, the corresponding force-displacement results and calculated relative errors were recorded in the MS Excel workbook file. This file was accessible for review upon the completion of the calibration procedure, allowing for an evaluation of the calibration’s accuracy and providing a comprehensive record of the iterative process.

Upon completing the iterative FE analyses of all material property combinations, ReConTwin identified the iteration with the smallest relative error compared to the load test control result.

This iteration was subsequently set as the DT model that could accurately simulate the force-displacement response of the RC beam specimens. The GUI Window 2 display (shown in Figure 4-6) was updated to reflect the calibration outcomes accordingly.

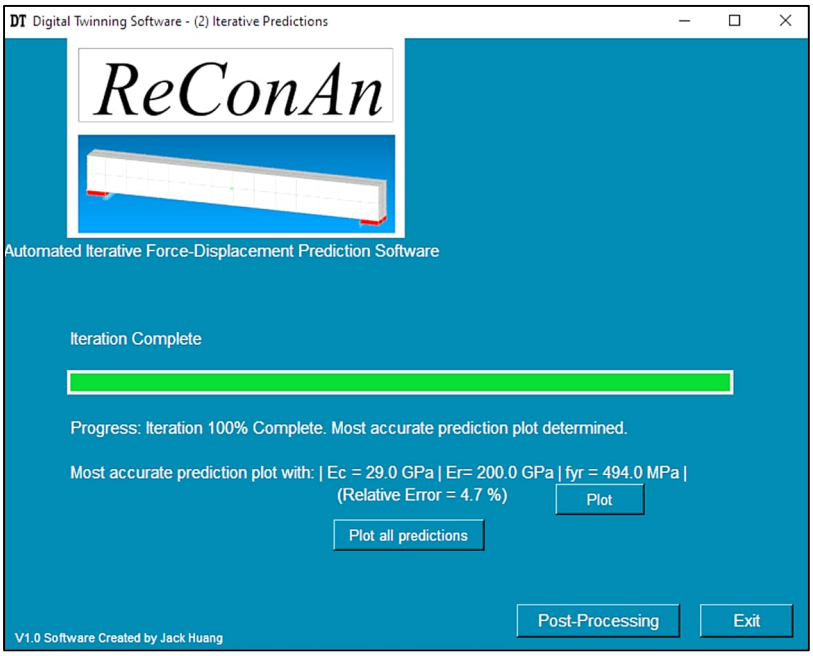

Figure 4-6: ReConTwin – GUI Window 2 – Calibration completion information display and graphical plot buttons for result review

GUI Window 2 was developed to provide post-processing capabilities, allowing users to review the DT calibration outcomes by graphically generating force-displacement plots. These plots can either display the most accurate iteration result independently or all iterations compared to the control load test results. Based on the calibration outcome, users can adjust the input parameters in GUI Window 1 to reperform the DT calibration as many times as required to achieve a DT with an accuracy which falls within the preferred error tolerance relative to the control result. Out of the 72 analysis iterations based on the specified basic and iterative material property input parameters, ReConTwin identified an iteration as the DT with a mean relative error of 4.7% compared to the control result. The material properties for this iteration are as follows:

- Concrete - Young's Modulus: 29 GPa
- Reinforcing - steel Young's Modulus: 200 GPa
- Reinforcing - steel yield stress: 494 MPa

The graphical plots illustrating the force-displacement results of the control sensor compared to all performed iterations and the most accurate iteration (DT) are shown Figure 4-7 and Figure 4-8, respectively.

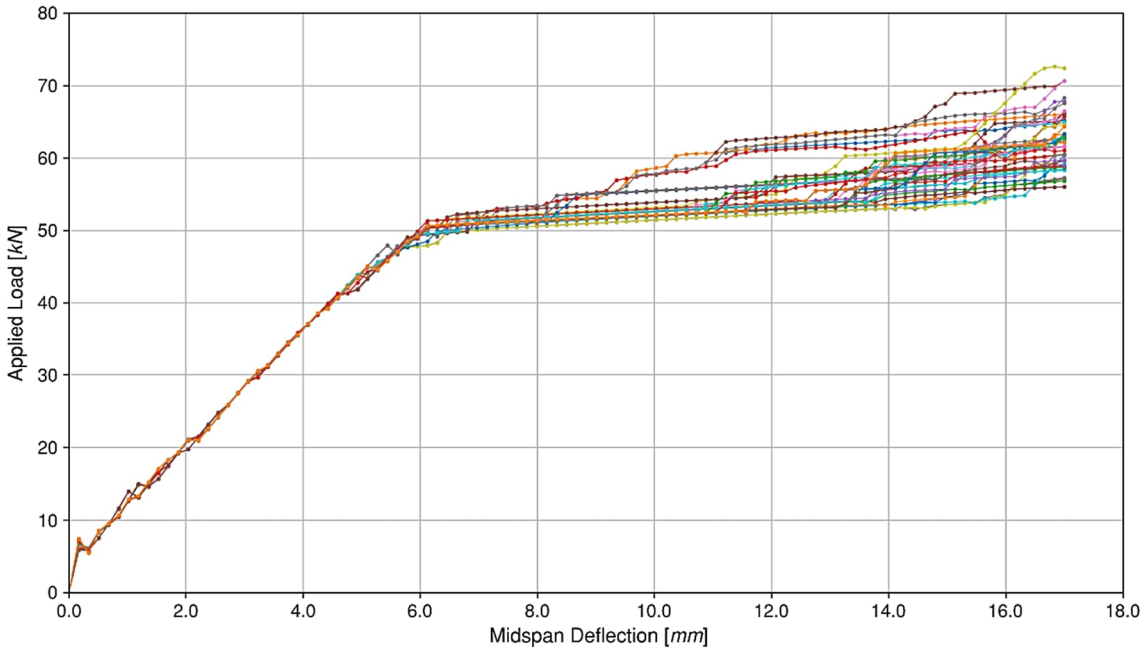

Figure 4-7: ReConTwin – GUI Window 2 – Force-displacement result graphical plot of all 72 performed iterations and control result

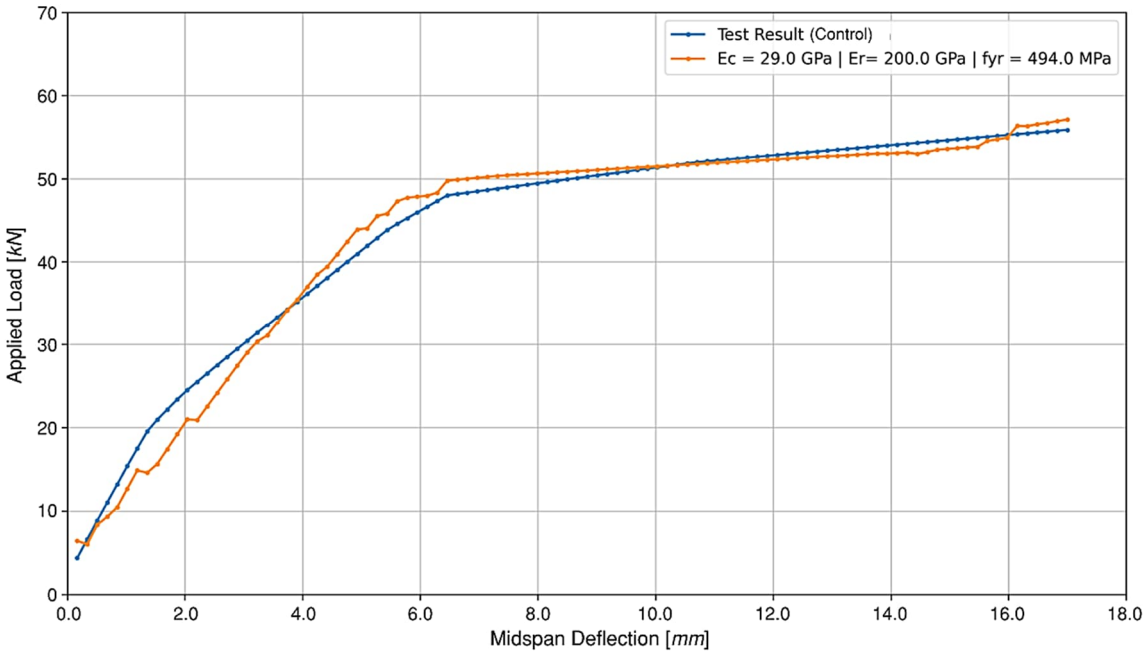

Figure 4-8: ReConTwin – GUI Window 2 – Force-displacement result graphical plot of the most accurate iteration (DT) and control result

The 72 iterations obtained from the calibration process exhibit consistent force-displacement behaviour between the applied loads of 0 kN and 50 kN. In this load range, all iterations displayed a lower bending stiffness compared to the control result from 0 kN to 34 kN, and a higher stiffness from 34 kN upwards. Beyond the theoretically approximated reinforcing steel tensile yield strength of 40 kN, the slope of all iterated curves gradually reduced, accurately reflecting the strain hardening effect of the reinforcing steel, as shown by the numerically obtained graph. Thereafter, the curves rapidly flattened caused by the necking of the tensile steel. This behaviour closely resembles the control test data, where the yielding strength of the steel was reached at approximately 48 kN.

As the imposed load continued to increase from 50 kN, nearly all iterations were observed to extend above the control force-displacement curve, indicating a slight overestimation of the beam's stiffness. Largely influenced by the higher steel yield stresses applied in several iterations, the FE beam models were found to possess a higher degree of residual stress, leading to a steeper rise of the iteration curve prior to failure.

The discrepancies between the control and the iteration results are attributed to numerous factors including the inaccuracies in the assumed strain-hardening behaviour, cracking mechanisms, bond-slip characteristics between concrete and steel, and creep. These complex aspects contribute to the inherent challenges in achieving perfect agreement between the nonlinear analytical FE model and the experimentally derived data. However, the most accurate iteration (as shown in Figure 4-8) closely aligned with the control result, with a relative error of 4.7%. This near congruence indicates an excellent fit and simulation, demonstrating that the DT calibration effectively captured the beam's mechanical response across the entire load spectrum.

The automated, iterative approach employed in this study successfully created a DT that accurately simulates the mechanical response of the RC beam specimen. By utilising a relatively uncomplicated procedure that does not require a highly complex calibration process or intricate FE models, and by making reasonable assumptions within this study's framework, it has proven to be a robust and efficient method to develop reliable DTs capable of accurately predicting the structural behaviour of the monitored structures.

4.3 LOAD TEST STAGE 2 – SMART SENSOR PERFORMANCE

In the second load test stage, the final RC beam specimen underwent two phases of three-point bending load experiments: static-cyclic and static-incremental load tests. The developed IoT-enhanced smart displacement sensors were employed during these experiments, and their performance in monitoring the mechanical response of the RC beam under varying loading conditions was assessed. This stage also aims to validate the reliability and accuracy of the calibrated DT in predicting beam soffit strain using the developed ReConTwin. Additionally, the framework's damage prognosis capabilities, enabled by ReConTwin are demonstrated.

4.3.1 Phase 1 – Static-Cyclic Load Test

In the first phase of the load test, the RC beam specimen was subjected to short-term, static-cyclic loading characterised by a series of repetitive loading and unloading sequences at its mid-span. While remaining in the RC beam specimen's elastic limit, three load cycles, ranging from 0 kN to 4 kN, 4 kN to 12 kN, and 12 kN to 20 kN, were progressively applied. The loading and unloading were carried out at a rate of a minute per load step, with each load step maintained for a period of 2 minutes.

The displacements of the overall static-cyclic test measured by the potentiometer contact sensor, IR non-contact sensor, and the control LVDT sensor at the mid-span of the beam soffit are illustrated in Figure 4-9. Results for each load cycle on a smaller temporal scale are independently provided in Appendix A.10 for clarity.

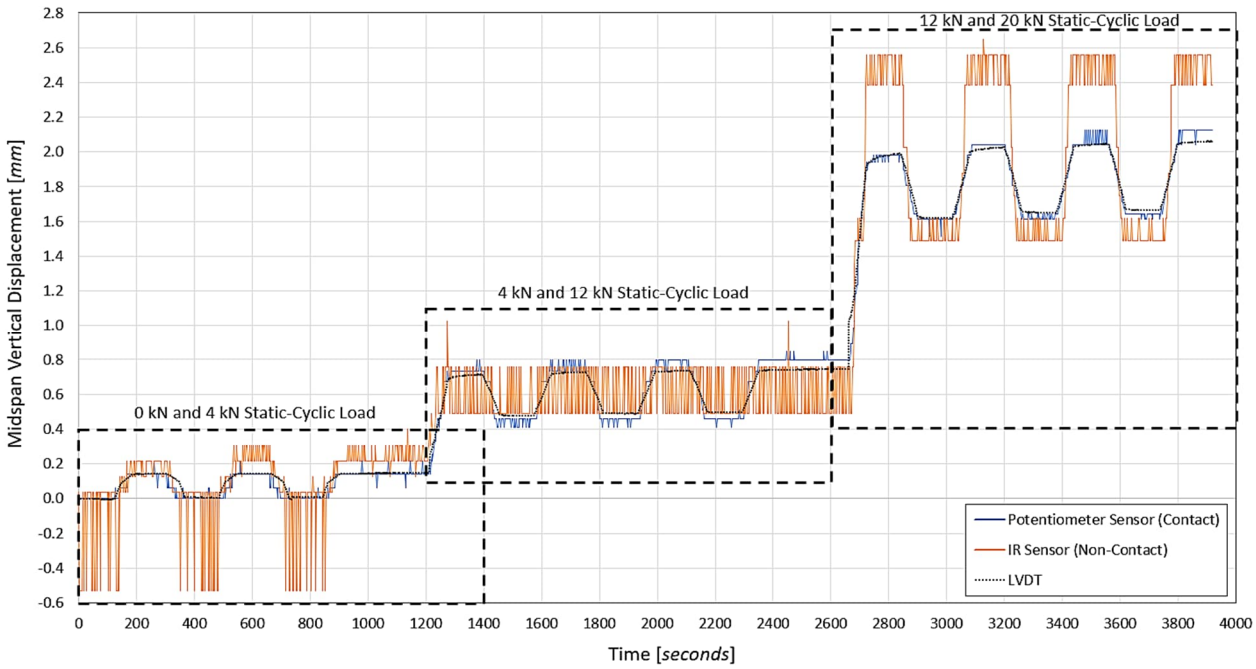

Figure 4-9: Overall static-cyclic test displacement results (Phase 1, Load Test Stage 2)

For each maintained load step, the mean displacements were calculated by averaging all measured displacements during each maintaining period for all three sensors. The summary of the comparative displacement results of the potentiometer, IR sensor, and the LVDT control obtained from the static-cyclic test is summarised in Table 4-2.

Table 4-2: Summary of displacement results of static-cyclic test (Phase 1, Load Test Stage 2)

Applied Point Load Sequence	LVDT	Potentiometer Sensor (Contact)				IR Sensor (Non-Contact)			
	Mean Displacement [mm]	Mean Displacement [mm]	Standard Deviation [µm]	Mean Absolute		Mean Displacement [mm]	Standard Deviation [µm]	Mean Absolute	
				Error [µm]	Percentage Error [%]			Error [µm]	Percentage Error [%]
4 kN	0.142	0.139	15.5	2.7	1.9	0.190	37.1	48.8	34.5
0 kN	0.007	0.002	10.2	4.7	71.3	-0.137	211.7	143.9	2167.1
4 kN	0.144	0.139	16.4	4.6	3.2	0.249	36.2	105.5	73.5
0 kN	0.008	0.002	10.2	6.6	78.8	-0.098	201.3	106.9	1267.6
4 kN	0.146	0.142	13.8	4.3	3.0	0.239	36.8	93.5	64.1
12 kN	0.705	0.733	14.6	28.1	4.0	0.591	120.8	114.6	16.3
4 kN	0.478	0.444	18.9	33.9	7.1	0.549	88.6	71.3	14.9
12 kN	0.724	0.751	21.8	27.7	3.8	0.620	109.6	103.2	14.3
4 kN	0.490	0.455	12.0	35.6	7.3	0.605	111.5	114.8	23.4
12 kN	0.733	0.784	21.1	50.7	6.9	0.623	113.0	109.7	15.0
4 kN	0.496	0.459	10.1	37.7	7.6	0.572	95.8	75.7	15.2
12 kN	0.742	0.798	8.0	55.7	7.5	0.605	109.1	137.3	18.5
20 kN	1.970	1.966	22.5	3.9	0.2	2.470	73.4	500.2	25.4
12 kN	1.621	1.605	19.2	15.5	1.0	1.525	49.8	96.1	5.9
20 kN	2.018	2.039	13.1	20.9	1.0	2.507	68.5	488.8	24.2
12 kN	1.652	1.621	12.2	31.5	1.9	1.520	44.9	132.5	8.0
20 kN	2.041	2.065	28.8	23.7	1.2	2.501	68.4	459.3	22.5
12 kN	1.667	1.641	9.1	26.5	1.6	1.504	35.5	163.3	9.8
20 kN	2.057	2.121	18.7	64.4	3.1	2.502	67.7	445.1	21.6
			Average:	25.2	11.2		**Average:**	184.8	202.2

In comparison to the LVDT, the Mean Absolute Error (MAE) values for the potentiometer sensor remained consistently low, ranging between 2.7 µm and 64.4 µm, with an overall average MAE of 25.2 µm throughout the test, as shown in Figure 4-10. Conversely, the MAE values for the IR sensor were significantly larger, ranging from 48.8 µm to 500.2 µm, with an overall average MAE of 184.8 µm. Notably, the IR sensor produced larger errors at the higher applied load of 20 kN. The Mean Absolute Percentage Error (MAPE) values further highlight the performance differences between the two sensors. The potentiometer sensor shows a MAPE ranging from 0.2% to 78.8%, with an overall average of 11.2%, demonstrating relatively consistent accuracy. In contrast, the IR sensor exhibits a much wider MAPE range of 5.9% to

2167.1%, with a significantly higher overall average of 202.2%, indicating substantial variability and reduced precision. For both sensors, the MAPE values are notably inflated at the 0 kN load sequences, primarily due to the small mean displacement values, which amplify percentage-based error calculations. However, as the comparative LVDT displacement measurements increase, the MAPE values decrease, reflecting improved relative accuracy at higher displacement values.

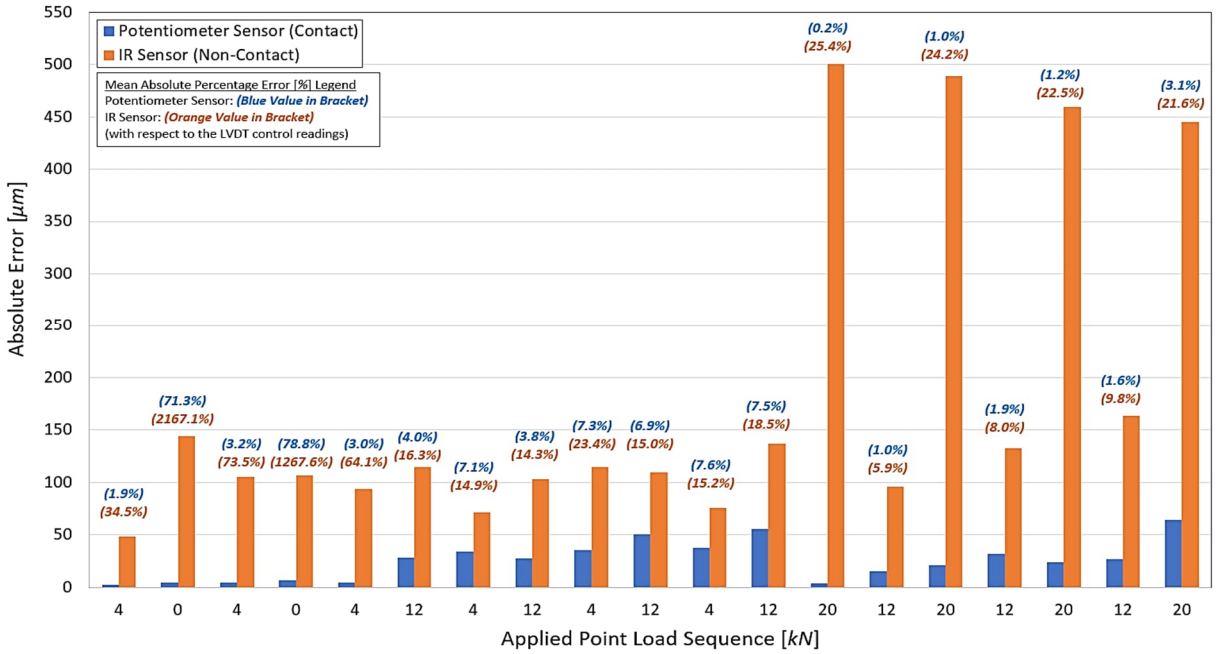

Figure 4-10: Mean absolute error and percentage error of potentiometer and IR sensors displacement results of static-cyclic test (Phase 1, Load Test Stage 2)

As anticipated during the calibration procedure for the contact and non-contact sensors (Chapter 3.7.4), both sensors produced fluctuating measurements due to their inherent noise characteristics. To quantify this variability, the standard deviation (SD) of the measurements during each load-maintaining period was determined. The SD values for the potentiometer remained consistently low, ranging from 8.0 µm to 28.8 µm (as shown in Figure 4-11), indicating an approximately constant trend of small variability across all applied load steps. In contrast, the SD measurements for the IR sensor varied more significantly, ranging from 36.2 µm to 211.7 µm. Due to the IR's larger resolution, small changes in displacement (50 µm to 100 µm) could not be captured as accurately compared to the potentiometer. The variations also substantially limited the achievable accuracy for the IR displacement sensor. However, a general decreasing trend in SD values was observed, attributed to reduced noise levels at shorter measuring distances as discussed in Chapter 3.7.4.

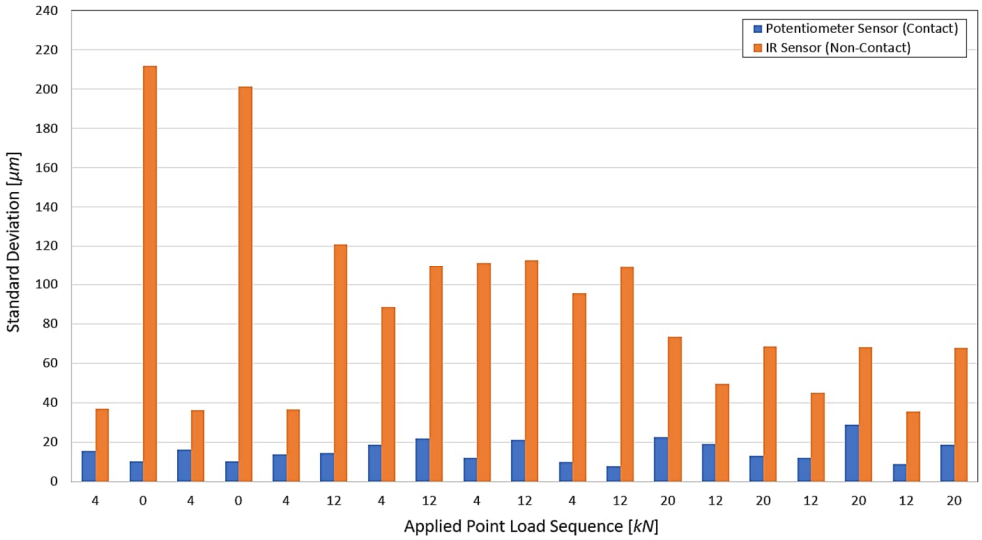

Figure 4-11: Standard deviation of potentiometer and IR sensor displacement results of static-cyclic test (Phase 1, Load Test Stage 2)

4.3.2 Phase 2 – Static-Incremental Load Test

In the second phase of the load test, the RC beam specimen underwent a static-incremental load test, following a procedure similar to the three-point bending test performed in Load Test Stage 1. The beam was subjected to increasing static loads at its mid-span, up to a maximum measurable load step of 52 kN. The load was incrementally applied in 4 kN steps, with each step applied over one minute and maintained for a period of two minutes.

The displacements during the static-incremental test were measured using the potentiometer contact sensor, IR non-contact sensor, and the control LVDT sensor at the mid-span of the beam soffit. These measurements are illustrated in Figure 4-12. For clarity, detailed, graphically magnified results for incremental loading between 0 kN and 20 kN, 20 kN and 40 kN, and 40 kN and 52 kN are provided in Appendix A.11.

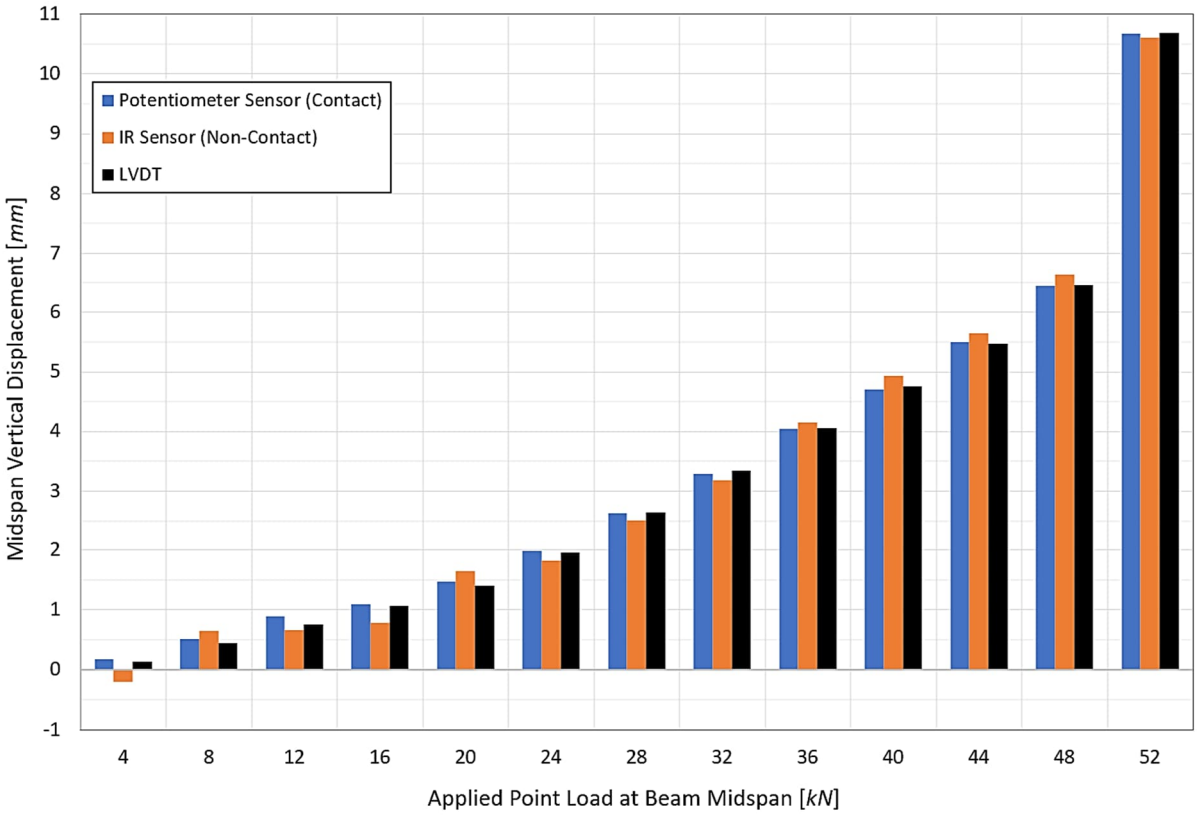

Figure 4-12: Overall static-incremental test displacement results (Phase 2, Load Test Stage 2)

For each maintained load step, the mean displacements were calculated by averaging all measured displacements during each maintaining period for all three sensors. Table 4-3 summarises the comparative displacement results obtained from the potentiometer, IR sensor, and the LVDT control during the static-incremental test. Due to the large deflections resulting from the RC beam exceeding its elastic limit at loads above 40 kN, the SD values were not considered for the load steps between 40 kN and 52 kN.

Table 4-3: Summary of displacement results of static-incremental test (Phase 2, Load Test Stage 2)

Applied Point Load Sequence	LVDT	Potentiometer Sensor (Contact)				IR Sensor (Non-Contact)			
	Mean Displacement [mm]	Mean Displacement [mm]	Standard Deviation [µm]	Mean Absolute		Mean Displacement [mm]	Standard Deviation [µm]	Mean Absolute	
				Error [µm]	Percentage Error [%]			Error [µm]	Percentage Error [%]
4 kN	0.142	0.175	10.8	32.9	23.2	-0.194	94.8	336.4	236.4
8 kN	0.443	0.511	10.7	68.6	15.5	0.642	56.4	199.9	45.2
12 kN	0.757	0.891	3.9	133.9	17.7	0.663	56.1	94.6	12.5
16 kN	1.067	1.095	14.3	28.2	2.6	0.782	54.7	284.9	26.7
20 kN	1.398	1.465	33.7	67.7	4.8	1.650	59.3	252.3	18.1
24 kN	1.957	1.979	18.5	21.3	1.1	1.822	50.7	135.1	6.9
28 kN	2.637	2.628	37.9	8.4	0.3	2.502	141.5	134.6	5.1
32 kN	3.341	3.283	25.9	57.7	1.7	3.180	42.8	160.5	4.8
36 kN	4.056	4.050	19.1	5.7	0.1	4.151	31.4	95.5	2.4
40 kN	4.758	4.706	**	52.1	1.1	4.926	**	168.3	3.5
44 kN	5.469	5.499	**	30.2	0.6	5.642	**	173.1	3.2
48 kN	6.458	6.443	**	14.9	0.2	6.635	**	176.2	2.7
52 kN	10.684	10.670	**	13.9	0.1	10.607	**	77.4	0.7
			Average:	41.2	5.3		**Average:**	176.0	28.3

(Note: ** indicates uncalculated values due to excessive deformation from exceeding steel yield stress)

In the incremental load experiment, the potentiometer's MAE measurements ranged from 5.7 µm to 133.9 µm, with an overall average MAE of 41.2 µm, as shown in Figure 4-13. This indicates that the potentiometer sensor closely follows the LVDT readings, demonstrating high accuracy across all load increments. In contrast, the IR sensor exhibited higher errors, with MAE values ranging from 77.4 µm to 336.4 µm, and an overall average MAE of 176.0 µm. It was observed that the error of the IR sensor gradually decreased at higher load levels as the detecting distance between the sensor and the RC beam soffit reduced. The MAPE values for the static-incremental test reveal clear performance distinctions between the potentiometer and IR sensors. The potentiometer sensor's MAPE ranges from 0.1% to 23.2%, with an overall average of 5.3%. At lower loads, such as 4 kN, the percentage error is higher (23.2%) due to the small LVDT displacement values, but the error significantly decreases as the displacement increases, dropping below 1.0% at 28 kN, 36 kN, 44 kN to 52 kN load sequences. This trend highlights the potentiometer's strong capability to provide precise measurements across a wide range of displacements. In contrast, the IR sensor exhibits a wider MAPE range of 0.7% to 236.4%, with an overall average of 28.3%, reflecting greater variability and reduced precision. The error is particularly inflated at smaller displacements, such as at 4 kN, where the MAPE reaches 236.4%. However, the IR sensor shows noticeable improvement at higher loads, with

MAPE dropping below 3.5% from 36 kN onwards, reaching its lowest value of 0.7% at 52 kN. While the IR sensor performs better under higher loads, its overall accuracy remains inferior to the potentiometer, especially at smaller displacements.

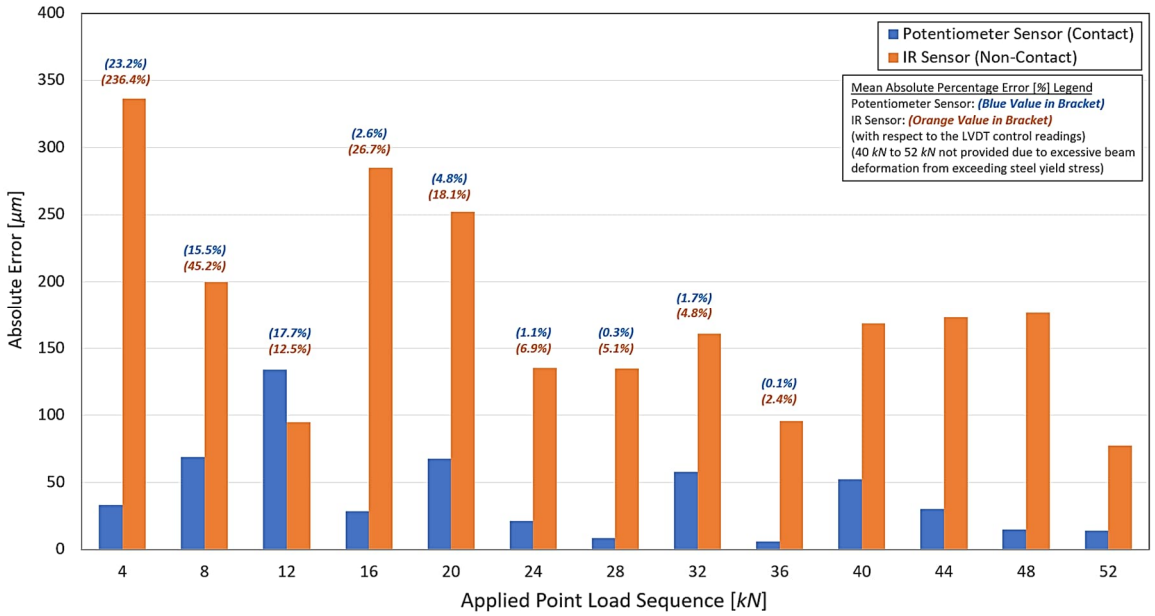

Figure 4-13: Mean absolute error and percentage error of potentiometer and IR sensors displacement results of static-incremental test (Phase 2, Load Test Stage 2)

The static-incremental test results confirmed the potentiometer sensor's reliability and consistency, similar to the outcome from the static-cyclic test. The potentiometer maintained low SD values ranging from 3.9 μm to 37.9 μm as depicted in Figure 4-14, reflecting an approximately constant trend of minimal variability in displacement readings across different applied loads. The IR sensor, however, showed greater fluctuations in displacement readings, with SD values ranging from 31.4 μm to 141.5 μm. Despite an isolated SD at the 28 kN load, a general decreasing trend in SD values with increasing loading was observed, attributed to reduced noise levels at shorter measuring distances.

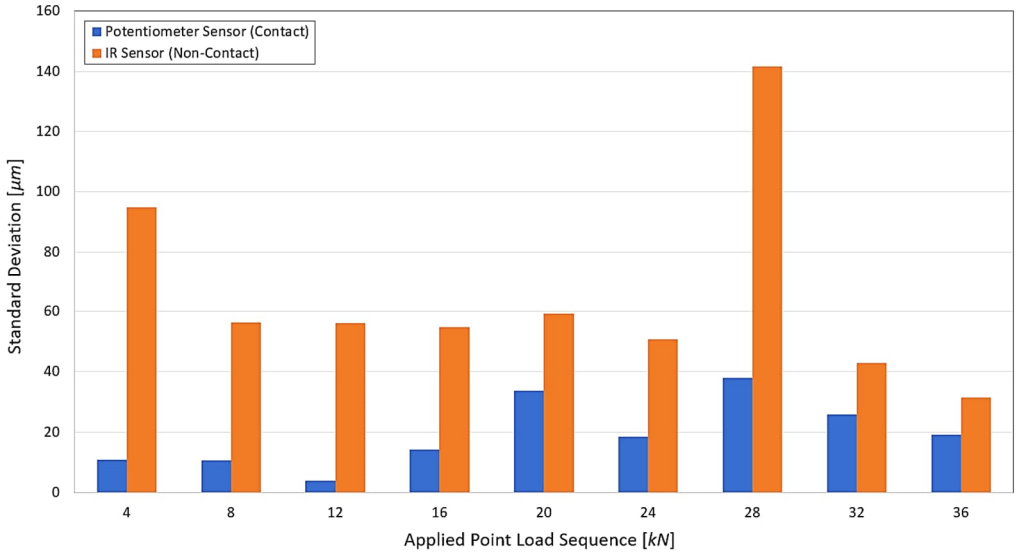

Figure 4-14: Standard deviation of potentiometer and IR sensor displacement results of static-incremental test (Phase 2, Load Test Stage 2)

4.3.3 Displacement Sensor Performance

The static-cyclic, and incremental experiments were conducted to simulate the structural behaviour of the RC beam under typical day-to-day usage condition and overloading circumstances, respectively. During these tests, the potentiometer contact sensor demonstrated excellent accuracy, achieving an average MAE of 25.2 μm in the static-cyclic test and 41.2 μm in the static-incremental test, both well below the initial calibration estimate of ±80 μm. Furthermore, the potentiometer sensor's MAPE values ranged from 0.1% to 78.8%, with an overall average of 11.2% in the cyclic test and 5.3% in the incremental test, showcasing its ability to deliver accurate measurements across various load levels. This minor inaccuracy is partially attributed to hysteresis, estimated to be 0.11% relative to its full extension length during calibration. Similarly, the IR non-contact sensor displayed an average MAE of 184.8 μm in the static-cyclic test and 176.0 μm in the static-incremental test, both aligning with its estimated calibration value of ±363 μm. However, its MAPE values were significantly higher, ranging from 5.9% to 2167.1%, with overall MAPE averages of 202.2% and 28.3% in the cyclic and incremental tests, respectively. These results highlight the IR sensor's greater inaccuracy, particularly at smaller displacement measurements.

Throughout the experiments, the potentiometer sensor demonstrated consistently low SD values, ranging from 8.0 μm to 28.8 μm in the static-cyclic test and 3.9 μm to 37.9 μm in the static-incremental test, reflecting its high precision and measurement stability across different load levels. In contrast, the IR sensor exhibited significantly greater variability, with higher SD

values ranging from 36.2 μm to 211.7 μm in the cyclic test and 31.4 μm to 141.5 μm in the incremental test, highlighting its reduced consistency. This variability is primarily attributed to its intrinsic higher noise levels and lower resolution, with noise arising from factors such as electrical interference, ambient light variations, surface reflectivity, and the surface condition of the detected object, as outlines in Section 3.7.4. During calibration tests, the IR sensor's ADC digits fluctuated by 2 to 3 units, even when measuring a stationary object at a constant distance. During load testing, with a contactless detection range of 50 mm to 70 mm and a corresponding resolution of 125 μm to 210 μm per ADC digit (Figure 3-24), a maximum error of ±630 μm can be expected. This aligns with the MAE observed in Load Test Stage 2, with a maximum of 500.2 μm in the static-cyclic test and 336.4 μm in the static-incremental test. Notably, the latter test showed lower errors due to improved resolution at reduced detection distances. Despite these limitations, the IR sensor's non-contact design, low cost (20% of the proposed potentiometer sensor's cost), and ability to achieve comparable sub-millimetre accuracy make its performance significant.

Overall, both proposed smart sensors have demonstrated significant potential as effective, low-cost displacement measuring devices for monitoring the sub-millimetre mechanical response of structural elements. The potentiometer contact sensor, with its higher accuracy of (MAE of 41.2 μm and overall MAPE of 11.2%) and high reliability (SD of 37.9 μm), is particularly suitable for applications requiring precise measurements. Meanwhile, the IR non-contact sensor, though less precise (SD of 211.7 μm), remains a viable alternative for monitoring applications where slightly higher error margins (MAE of 184.8 μm and overall MAPE of 202.2%) are tolerable and the benefits of non-contact measurements are advantageous. Both sensors can contribute to the implementation of a practical and cost-effective DT-integrated SHM framework.

4.3.4 Sensor IoT Capability

The hardware system of the DT-based SHM framework was enhanced with the integration of the Arduino Nano 33 IoT wireless communication microcontroller. During the three-point bending experiments in Load Test Stage 2, the microcontroller established a wireless internet connection with a Wi-Fi access point by means of a smartphone hotspot. This connectivity enabled communication with the Arduino IoT Cloud, facilitating the real-time transmission and storage of displacement measurements on the platform. These displacement data could be remotely accessed via an internet-connected smartphone application or web browser, as shown in Figure 4-15, and downloaded for further review and processing.

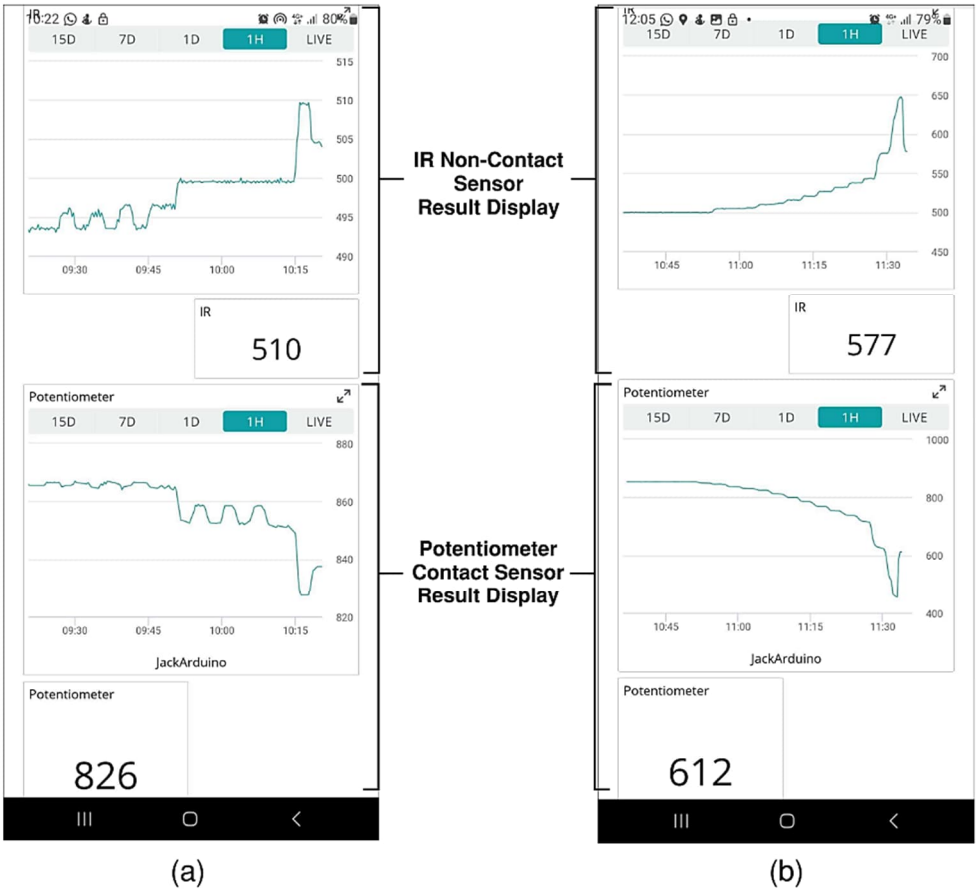

Figure 4-15: Smartphone application Arduino IoT Cloud access and display of ADC digit result for the displacement sensors: (a) Static-cyclic test, and (b) Static-incremental test

The seamless integration of the Arduino with the DT-SHM framework promoted an automated and efficient data transmission from the physical structure to the digital model. This minimised the need for manual intervention, reduced potential errors, and allowed for accelerated post-processing procedures, thereby enhancing the overall efficiency and responsiveness of the SHM process.

4.4 POST-PROCESSING RESULT

Following the calibration of the DT and the acquisition of the sensor displacement data, a comprehensive post-processing procedure was carried out as part of the DT-SHM framework validation. The DT, a numerical FE model simulating the mechanical response of the RC beam specimen, was incorporated with real-time sensor data to estimate the applied loads and predict crack formations and widths of the monitored RC beam specimen.

The GUI Window 3 of ReConTwin facilitated an intuitive and streamlined post-processing procedure, as seen in Figure 4-16. For each maintained load step during the static-incremental test (Load Test Stage 2, Phase 2), displacement data retrieved from the potentiometer sensor were downloaded from the Arduino Cloud platform and locally saved on the computer for processing. The file directory containing the displacement files was specified through the user interface and imported into ReConTwin.

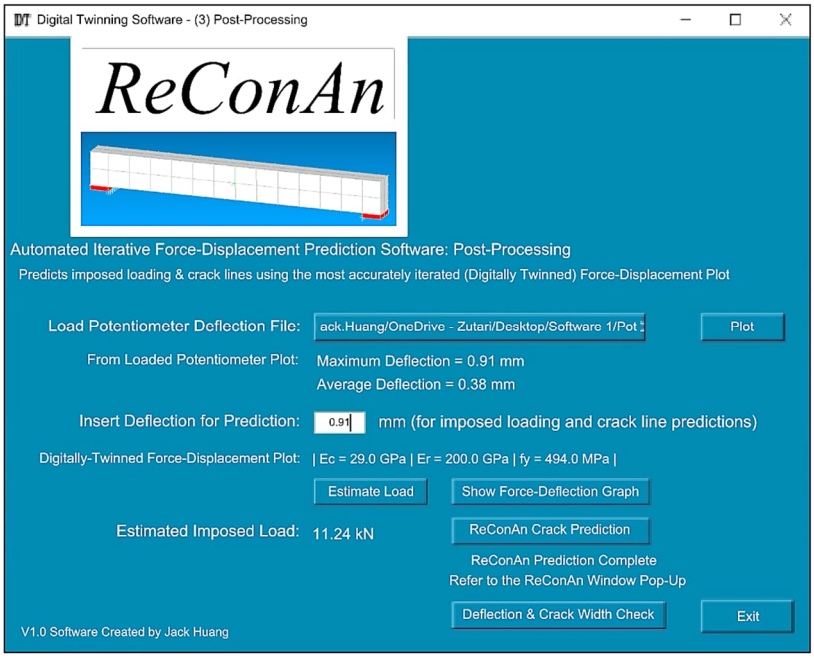

Figure 4-16: ReConTwin – GUI Window 3 – Post-processing

After activating the “Plot” button, the imported displacement data from the potentiometer over the selected detection period was graphically displayed for review, as shown in Figure 4-17. This plot graphically illustrates the time-dependent displacement readings, providing users with a comprehensive record of the beam’s deflection history. It enables users to analyse the magnitude of deflection and its corresponding timing, facilitating the selection of an appropriate displacement value for input into the software for damage diagnostics. The “Plot” functionality also activated ReConTwin to perform an automated analysis on the imported displacement file, determining the maximum and average beam deflection values during the recording period. This information was reflected on the user interface. The corresponding deflection value for each load step was inserted into the prompt field, which ReConTwin applied in the back-calculation of the applied load.

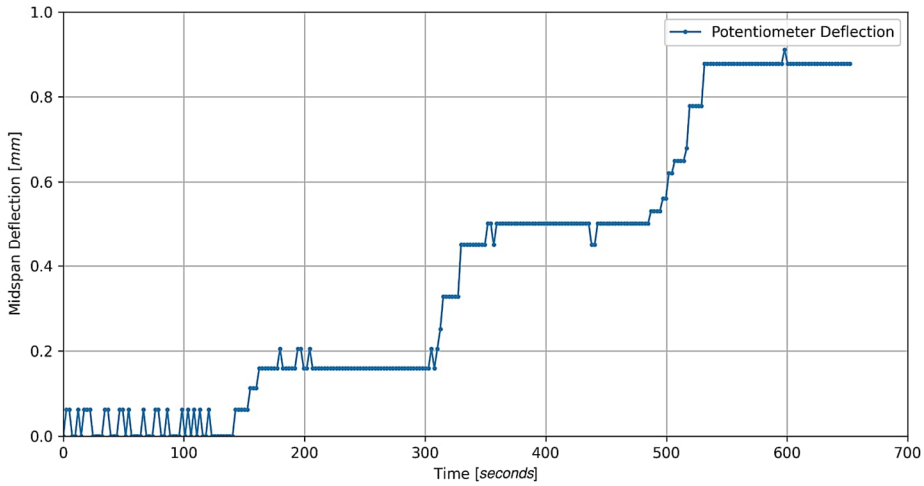

Figure 4-17: GUI Window 3 – Typical potentiometer displacement graphical plot over the measured period from 4 kN to 12 kN

By selecting the “Estimate Load” button, ReConTwin estimates the imposed beam mid-span point load using a back-calculation procedure. The force is interpolated from the force-displacement graph based on the specified displacement parameter, and this estimated load is reported back to the user interface. Additionally, the “Show Force-Deflection Graph” button can be executed to graphically illustrate this process against the DT force-displacement plot, as shown in Figure 4-18, providing a visual representation of the estimated load in relation to the DT model.

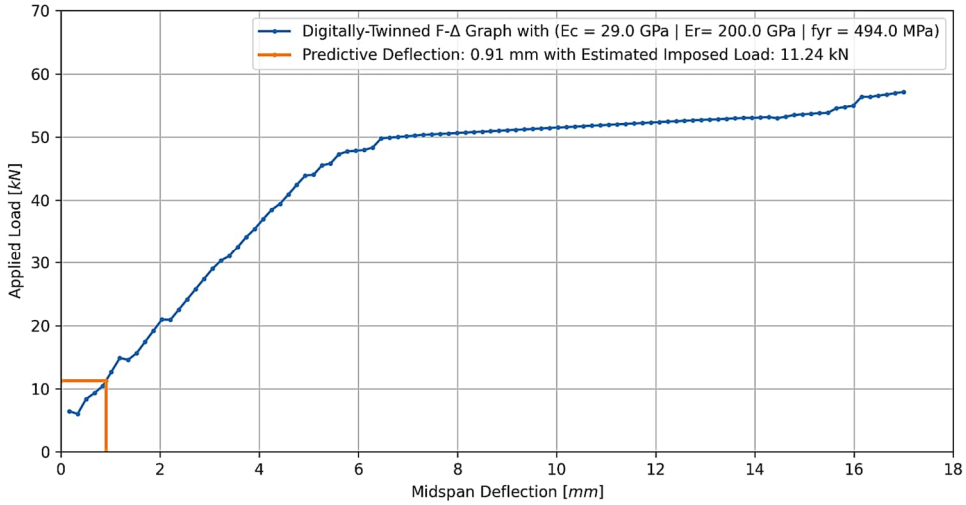

Figure 4-18: GUI Window 3 - Typical graphical plot of back-calculated imposed point load on beam on the DT force-displacement graph

By utilising this post-processing workflow, the mid-span beam deflection for each applied 4 kN incremental load step was inserted into ReConTwin to estimate the corresponding imposed loads using the DT. The comparison between the experimental and the DT-estimated imposed point loads is presented in Table 4-4. The final prediction was performed at 52 kN, the maximum stable measurable load prior to excessive deformation that led to failure.

Table 4-4: Comparison of the experimental and DT-estimated imposed load

Inserted Mid-span Deflection [mm]	Experimental Imposed Load [kN]	DT-Estimated Imposed Load [kN]	Absolute Error [kN]	Relative Error [%]
0.142	4.00	5.37	1.38	34.6
0.443	8.00	7.44	0.57	7.1
0.757	12.00	9.84	2.16	18.0
1.067	16.00	13.27	2.73	17.0
1.398	20.00	14.83	5.18	25.9
1.957	24.00	20.11	3.89	16.2
2.636	28.00	24.98	3.01	10.8
3.34	32.00	30.79	1.20	3.8
4.055	34.00	36.77	0.77	2.1
4.758	40.00	42.43	2.43	6.1
5.47	44.00	46.08	2.07	4.7
6.46	48.00	49.78	1.78	3.7
10.69	52.00	51.78	0.22	0.4
		Average:	2.11	11.6

The analysis of the imposed load data reveals a consistent estimation by the DT model for applied loads between 8 kN and 32 kN, conservatively in favour of safety. The DT showed a peak underestimation of 5.18 kN at the 20 kN load step, with errors ranging from 0.57 kN to 3.89 kN. At higher load levels exceeding the 36 kN load step, the DT model tended to overestimate the imposed loads, with errors ranging from 0.77 kN to 2.43 kN. This behaviour aligns with the force-displacement relationship depicted in Figure 4-8.

Overall, the DT model achieved an average absolute error of 2.11 kN and an overall relative error of 11.6% across all applied load step levels. This indicates that the DT model provides a highly accurate representation of the beam's mechanical response under varying load magnitudes.

In the final stage of the post-processing procedure, the displacement values obtained from the imported potentiometer data for each incremental load step were utilised to predict crack

formation of the RC beam specimen. By activating the “ReConAn Crack Prediction” button in GUI Window 3 (Figure 4-16), ReConTwin automatically executed *ReConAn* to perform a displacement-controlled FE analysis. This analysis utilised both the specified basic property inputs and the iterating material property inputs of the DT model. Upon completion, *ReConAn Eye* was activated to provide a 3D graphical visualisation of the predicted crack patterns and animations of crack formation and beam deformation. The crack visualisation results were based on the proportioned applied displacement increment relative to the specified upper deflection limit used in the analysis.

The comparison between the crack patterns predicted by *ReConAn* and the actual crack patterns observed during the static-incremental load experiment in Phase 2 test of Load Test Stage 2 is illustrated in Figure 4-19.

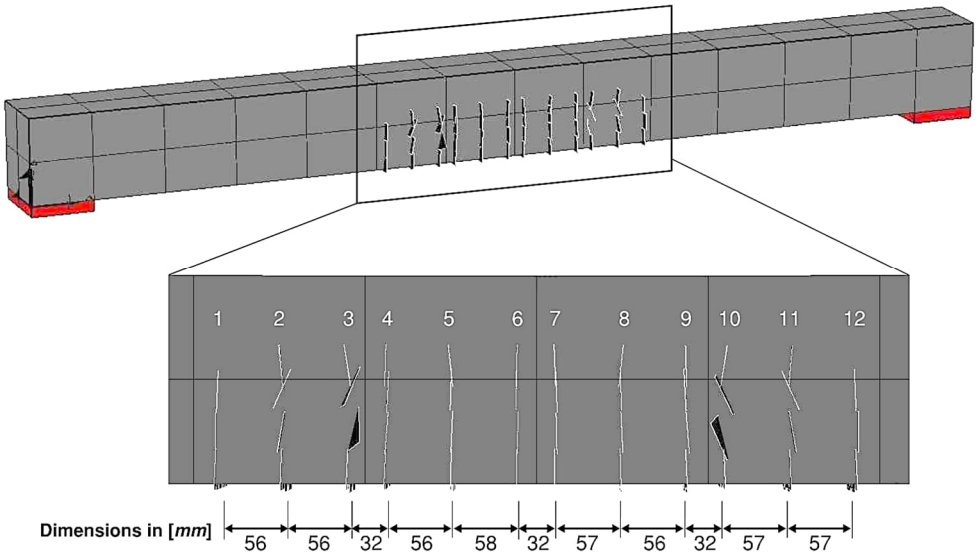

(a)

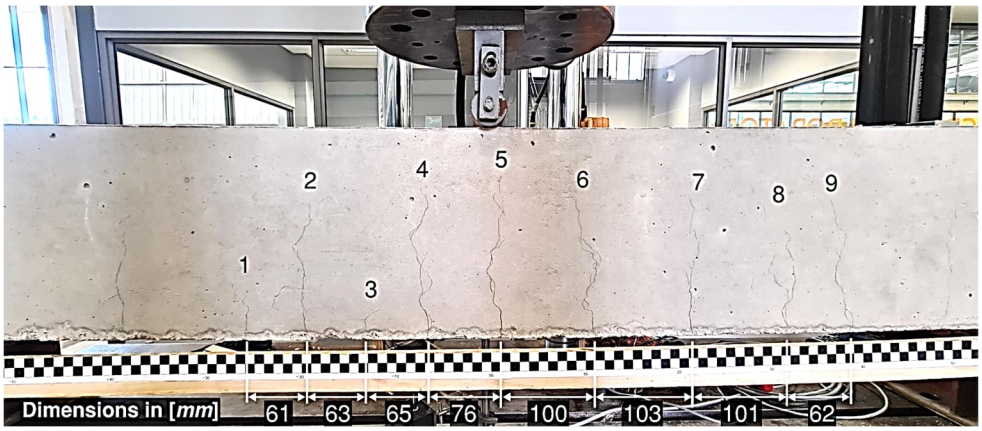

(b)

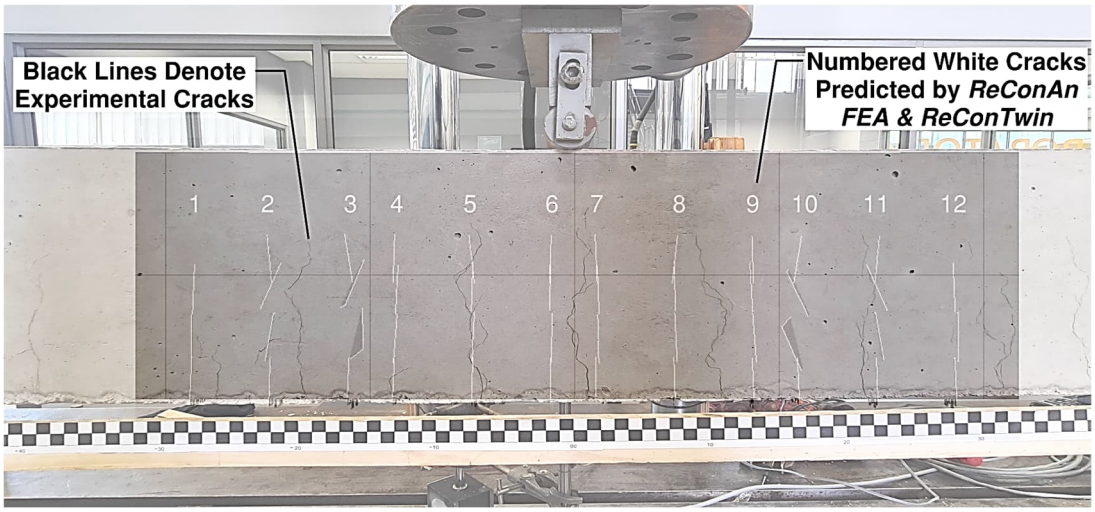

(c)

Figure 4-19: Cracks along the soffit of the RC beam specimen: (a) Predicted 3D crack formation in *ReConAn Eye*, (b) Experimental crack formations, and (c) Overlay of predicted and experimental crack patterns

The predicted mid-span RC beam soffit crack patterns generated by *ReConAn Eye*, although not identical to the actual observed patterns, demonstrated significant similarities in terms of general crack formation and spacing. *ReConAn* estimated an average crack spacing of 50 mm, which is slightly smaller than the observed average crack spacing of 79 mm. Overall, the potential damage to the beam was accurately predicted, showcasing the effectiveness of the *ReConAn* software in predicting structural damage.

4.5 BEAM DAMAGE DIAGNOSTIC

As a final step in completing the DT-SHM process, the damage diagnostic of the RC beam was performed to assess its structural conditions and provide automated warnings for preventive actions if the RC beam was not performing within expected limits. During each incremental load step of the Load Test Stage 2 Phase 2 three-point bending test, two key structural performance indicators were monitored: mid-span beam deflection and estimated concrete crack width. This verification was successfully implemented using GUI Window 4, where ReConTwin checked both the mid-span beam displacement and crack width against specified limits of a span-to-deflection ratio of 250 and a crack width limit of 0.3 mm, respectively, as shown in Figure 4-20a. If either criterion exceeded these limits, ReConTwin generated a warning, recommending the need for preventive actions to be taken, as shown in Figure 4-20b.

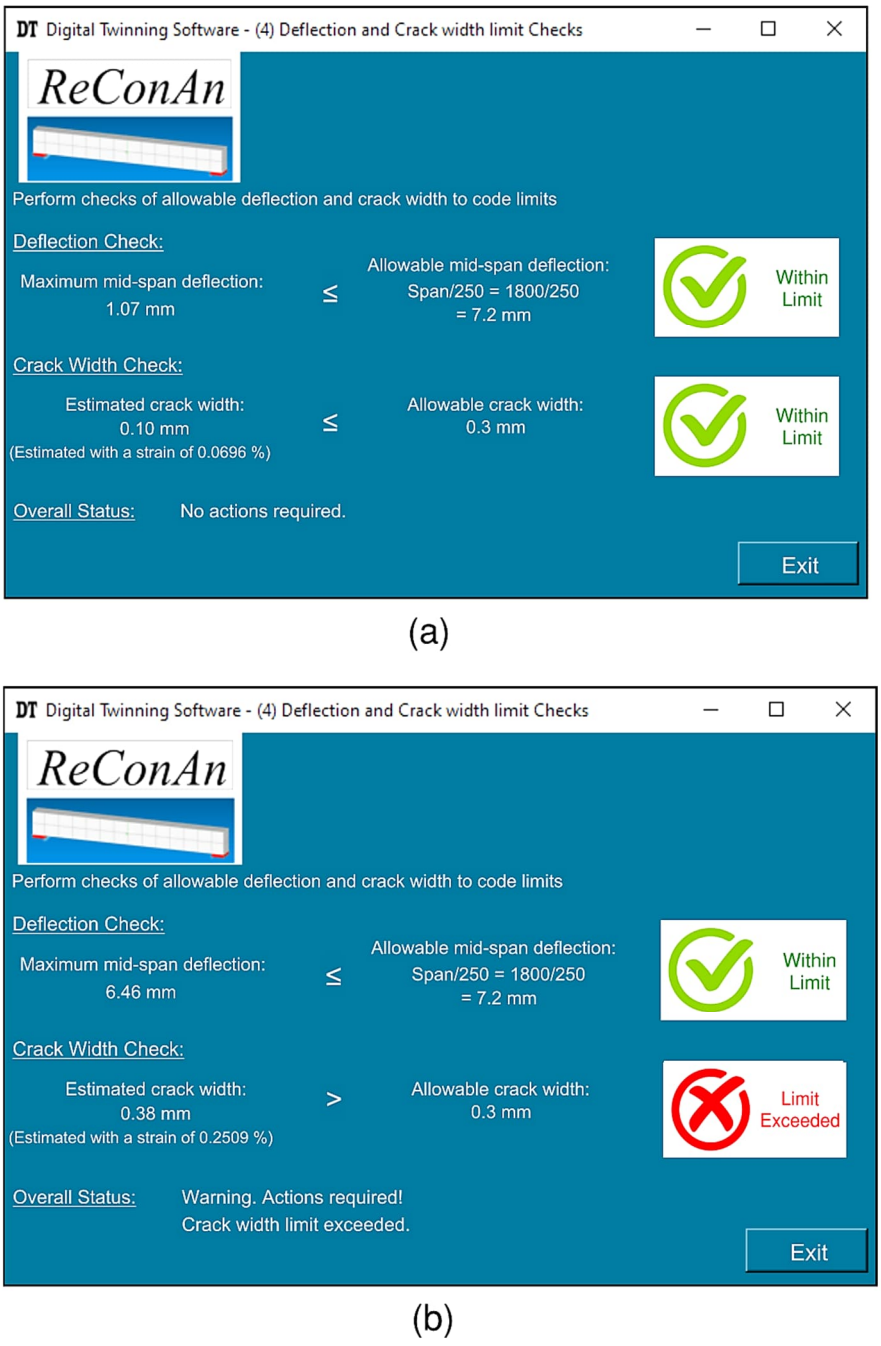

Figure 4-20: ReConTwin – GUI Window 4 - Damage diagnostic procedure with deflection and crack width checks: (a) At applied load of 16 kN (within limit), and (b) At applied load of 48 kN (exceeded limit)

In the estimation of the concrete crack width, ReConTwin obtained the maximum strain value along the soffit of the FE beam corresponding to the specified incremental load step from the *ReConAn* analysis output file. This strain value was subsequently, multiplied by the FE hexahedral element mesh length (150 mm) to determine the crack width. The reliability of the crack width prediction is, therefore, highly dependent on the accuracy of the strain values

determined by the DT model. The comparison of maximum beam soffit strains between the DT, as determined by *ReConAn*, and the mean experimental results of Load Test Stage 1 (Table 4-1) under static 4 kN incremental load steps is graphically illustrated in Figure 4-21. The numerical DT model consistently predicted maximum beam soffit strains at the mid-span for all applied load steps. In contrast, experimental results showed varying maximum strain positions along the beam span, influenced by factors such as nonlinear cracking mechanisms, material inhomogeneity, and construction or loading imperfections. These maximum strain positions, corresponding to the peaks of the strain profiles for the load steps, are highlighted with interpolated black dashed lines in Figures A-17, A-18, A-19 and A-20.

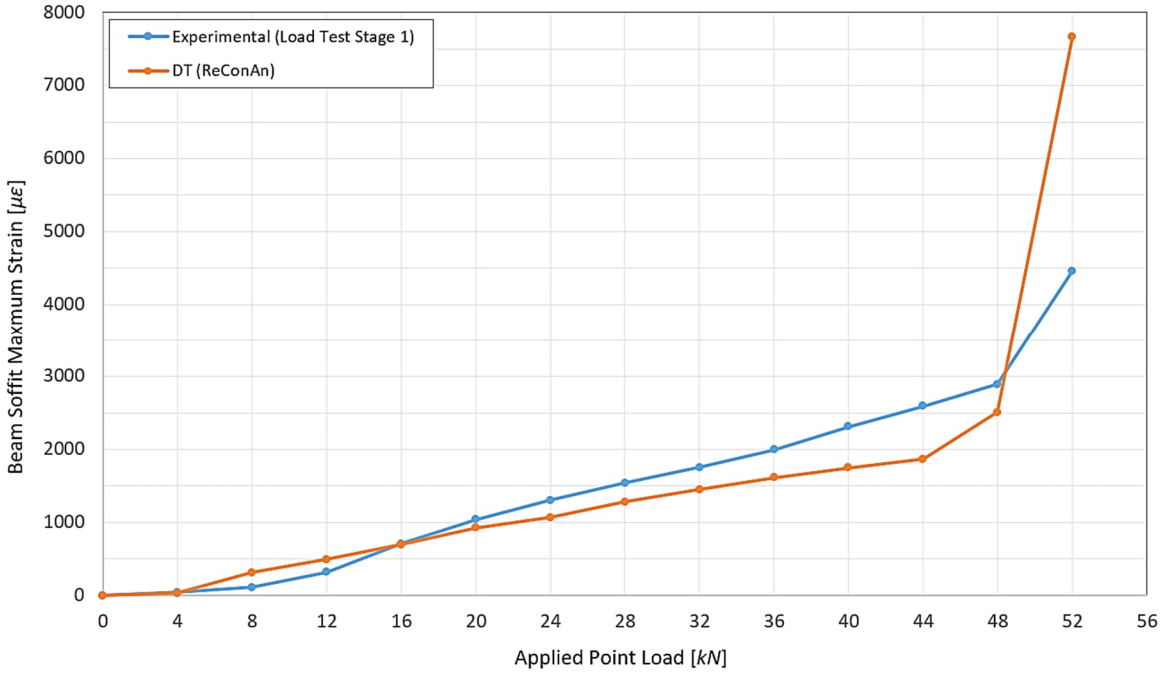

Figure 4-21: Comparison of the experimental and DT-estimated maximum mid-span soffit strains

Between 8 kN and 12 kN, the DT model slightly overestimated the strain. Conversely, for the load range of 16 kN to 48 kN, the DT model tended to slightly underestimate the strain. Despite these deviations, the DT model closely matched the experimental results, with an overall average absolute error of 281 με and an average relative error of 34.3%. Except for the 52 kN load step, where the absolute error significantly increased due to excessive deformation, the DT model demonstrated high accuracy in strain estimation. This accuracy significantly enhances the reliability of the predicted RC beam soffit crack width, especially for the total applied load below half of the ultimate load of the monitored structure. These results underscore the DT model's effectiveness in approximating the mechanical behaviour of the structural element, thereby ensuring the reliability of the damage diagnosis outcomes.

5 CONCLUSIONS AND RECOMMENDATIONS

This research explored novel methodologies for monitoring the structural health of existing civil infrastructures. While numerous DT and SHM methods are available, they are frequently complex, costly, and demand high computing power, rendering their implementation challenging and financially unfeasible particularly for small-scale SHM applications. The accompanying experimental study successfully developed a DT-based SHM prototype framework capable of digitally replicating the mechanical response of a RC beam, suitable for small-scale implementations. The hardware system comprises innovative low-cost contact and non-contact sensors, enhanced with a cost-effective IoT-enabled microcontroller. The software system consists of a practical software programme, ReConTwin, featuring a FE-based digital model with interactive and automated post-processing capabilities for near real-time model updates, analysis, and damage diagnosis. The calibrated DT, incorporated with real-time transmitted sensor data, achieved accurate load estimations, as well as strain and crack width predictions, providing the user with reliable insights into the monitored beam's structural behaviour for predicting its remaining serviceable life. The system's user-friendly design and compatibility with everyday computers significantly enhance its accessibility and feasibility for widespread adoption in civil infrastructure monitoring, ultimately improving the efficiency and responsiveness of SHM processes. In this chapter, the conclusions for each of the objectives outlined in Chapter 1.2 are presented. Recommendations for future improvement and implementation of the framework are also discussed.

5.1 CONCLUSIONS

5.1.1 Proposed Contact and Non-contact Displacement Sensors

This study introduced novel methods for measuring the displacement of structural members using a proposed potentiometer contact sensor and an IR non-contact sensor, neither of which have been traditionally considered as tools for detection mechanical response in past SHM systems. Due to rapid technological advancements, sensor electronics like these are continually improving in performance while becoming more affordable and accessible. In the context of SHM for civil infrastructures, these advancements are beneficial for civil engineers, enabling the implementation of practical and affordable SHM and DT systems.

The potentiometer contact-based sensor demonstrated excellent accuracy and resolution of 48.4 μm per ADC digit, with minimal standard deviation across various load levels, indicating high precision and measurement stability. Its minor inaccuracy, reflected in an overall absolute

error of 41.2 μm and an overall absolute percentage error of 11.2%, is partially attributed to hysteresis, which was estimated during the calibration stage to be 0.11% relative to its full extension length. Despite this slight nonlinear behaviour, the sensor remains highly accurate, with an overall standard deviation of 37.9 μm, making it suitable for applications requiring precise measurements. Conversely, the IR non-contact sensor, tested within a detection range of 50 mm to 70 mm, resulted in a larger resolution, varying between 125 μm to 210 μm per ADC digit, and lower accuracy with an overall absolute error of 184.8 μm and an overall absolute percentage error of 202.2%. The IR sensor also demonstrated greater variability, with an overall standard deviation of 211.7 μm, primarily due to its higher intrinsic noise levels and lower resolution. Nevertheless, it was capable of measuring sub-millimetre displacements, offering a viable option for monitoring applications where slightly higher error margins are acceptable and non-contact measurement is advantageous.

Both sensors have proven to provide precise and reliable results, are compact, easy to operate, and require minimal maintenance. Overall, the proposed contact and non-contact sensors show significant potential as effective, low-cost displacement measuring devices for monitoring the sub-millimetre mechanical response of structural elements, supporting the implementation of practical and cost-effective DT-integrated SHM frameworks.

5.1.2 Cost-Effective IoT Sensors

The Arduino microcontroller employed in this experimental study significantly enhanced the sensors' functionality in the implementation of a DT-based SHM system. With continuous advancements in microcomputing hardware systems, wireless IoT sensors are becoming smaller, more energy-efficient, and cost-effective solutions that can be easily deployed. Compared to other industrial-grade solutions, the Arduino Nano 33 IoT is inexpensive, user-friendly, compact, and versatile with robust I/O capabilities.

During the three-point bending experiments, the Arduino established an internet connection through a wireless access point, transmitting real-time mechanical response data directly from the sensors to the IoT cloud platform. This hardware configuration powered the displacement sensors and enabled the real-time data access remotely via internet-connected devices, facilitating near real-time analysis and post-processing for the framework. This ultimately improved the efficiency and responsiveness of the SHM process.

By leveraging the low-cost solution, with a total cost of $124 (USD) for all electronic components, this study confirmed the feasibility of near real-time wireless data transmission

from the physical structure to the digital model. This integration minimises manual interventions, allowing seamless incorporation of sensor data to update analysis models promptly, predict the structure's realistic performance condition, and accelerates post-processing procedures. The outcomes demonstrate that cost-effective microcomputing hardware with IoT capabilities can effectively support a DT-based SHM framework.

5.1.3 Practical and Simplified DT-SHM Approach

This study demonstrates a practical and simplified approach for developing and post-processing a model-based numerical DT dedicated to predicting the mechanical behaviour of a RC beam. Unlike traditional SHM systems, which are often costly, complex, and require advanced expertise, this research offers a simpler, cost-effective, and more accessible alternative that is scalable for infrastructure asset management. This was achieved through the automated software core system developed in this study, enabling iterative structural analysis and calibration of the DT model. By introducing a simplified calibration process involving various combinations of the critical material properties, the DT accurately simulated the realistic bending stiffness of the monitored RC beam. This approach resulted in a precise representation of the beam's mid-span force-displacement response, achieving a relative error of 4.7%. The post-processing procedure produced a DT model that accurately captured the beam's mechanical response under varying load magnitudes. The model demonstrated high accuracy in imposed load estimation, with an average absolute error of 2.11 kN and an overall relative error of 11.6%. Additionally, it achieved accurate strain estimation, with an overall average absolute error of 281 με and an overall average relative error of 34.3% These results showcase the DT model's effectiveness in simulating structural behaviour and its potential as a reliable tool for structural health monitoring and damage diagnostics.

Developed using the popular Python programming language, the calibration and post-processing of the DT could be automated and streamlined. The designed GUI process flow further supported intuitive interaction, making the software system more transparent and accessible. Additionally, the predicted mid-span RC beam soffit crack patterns, generated by *ReConAn Eye*, showed significant similarities in general crack formation and spacing. This functionality effectively provided users with further insights into the structural behaviour of the monitored RC member, demonstrating ReConTwin's effectiveness in predicting structural damage not only at the superficial level but also internal damage at any 3D point within the RC domain. Furthermore, the FE analysis using *ReConAn* operates efficiently on standard computers, delivering reliable analysis results with a simpler data format compatible with

various software applications and operating systems, enhancing the software's universality and accessibility.

In summary, this study validates the hypothesis that IoT-enabled, affordable, and easily deployable sensors can achieve displacement measurement accuracy comparable to the LVDT control sensor. The contact and non-contact sensors demonstrated overall absolute errors of 41.2 μm and 184.8 μm, respectively, both well below the 1 mm prediction. Additionally, the DT model accurately simulated the beam's force-displacement response, achieving a relative error of 4.7%, below the hypothesised estimation of 10%. Furthermore, the DT model effectively estimated imposed mid-span point loads with an average absolute error of 2.11 kN and maximum strain values along the beam soffit with an overall average absolute error of 281 με, achieving a strong correlation with experimental results. By leveraging cost-effective IoT-enhanced microcontrollers and relatively uncomplicated software solutions, this research demonstrates that the realisation of a practical and efficient DT-based SHM framework is feasible. The findings highlight the potential for widespread adoption of such systems, offering a data-driven, proactive approach to maintenance strategies for civil infrastructure, ultimately enhancing monitoring precision, responsiveness, and decision-making.

5.2 RECOMMENDATIONS

The potentiometer contact sensor demonstrated high levels of accuracy and reliability, making it suitable for advanced applications requiring precise measurements of minor displacements at rapid sample collection rates, such as detecting vibrations and frequency responses of structural elements. The IR non-contact sensor exhibited efficacy in detecting displacement changes within a range of 50 mm to 70 mm (from the IR lens) in this study's experiments, achieving resolutions of 125 μm to 210 μm per ADC digit, an overall absolute error of 184.8 μm, and an overall standard deviation of 211.7 μm, all within the sub-millimetre domain. However, this sensor can operate over a broader range from 30 mm to 300 mm, with a higher degree of accuracy and reliability expected between 30 mm and 40 mm. The reading range of 70 mm to 300 mm, while expected to slightly reduce in performance, remains promising for detecting displacements with acceptable error margins and reliability tolerances, warranting further investigation. In the context of real-life civil infrastructure monitoring, these sensors offer significant potential for measuring relative movements between adjacent structures and monitor local crack widths, similar to the functionality of the LVDT sensor implemented by Wang & Yim (2010). Additionally, for global bridge displacement measurement, these sensors could

potentially be installed on fixed supporting piers or columns to quantify bridge deflection near the support, which can then be proportionally extrapolated to predict the mid-span deflection.

The wireless communication sensor technologies embedded with IoT capabilities, validated in this experimental study, and corroborated by numerous other researchers, have emerged as highly effective tools for developing next-generation SHM systems. These technologies offer significant advantages over traditional wired monitoring systems, including low-power consumption, cost-effectiveness, versatile incorporation and installation. This justifies the feasibility of their practical implementation in monitoring real-life civil structures. Several critical considerations must be addressed to ensure long-term viability and stability. Ensuring a reliable and stable wireless connection to access points with internet connectivity is imperative. Additionally, the power supply for both IoT smart sensors and wireless access point devices must be considered to guarantee continuous operation. An emerging and promising solution is the application of LoRaWAN, a type of wide area network with minimal power usage and a longer wireless range than Wi-Fi, making it suitable for applications in remote areas (Polonelli *et al*., 2018).

Although the DT development and calibration approaches undertaken in this study are specifically suited for uncomplicated SHM systems with simpler geometries, materials, and loading arrangements, their principles remain relevant for monitoring real-life civil infrastructures, which are often characterised by more complex geometries, material behaviours, environmental influences, physical imperfections, and varied load configurations. Simplifications can be employed to estimate the mechanical responses of these civil structures. A promising approach, as highlighted by Jasinski *et al*. (2023), involves conducting non-destructive load tests on real-life structures within their elastic limits. Sensor data obtained from these tests, combined with known applied loadings, can be used to calibrate the DT, accurately simulating the structural response. In conclusion, these methodologies provide a foundation for practical, cost-effective DT-based SHM frameworks that can be adapted and applied to more complex real-world infrastructures, ultimately enhancing infrastructure monitoring and management.

6 REFERENCES

Agdas, D., Rice, J. A., Martinez, J. R. & Lasa, I. R. 2015. Comparison Of Visual Inspection and Structural-Health Monitoring as Bridge Condition Assessment Methods. *Journal of Performance of Constructed Facilities*, Vol 30, No 3.

Amezquita-Sanchez, J. P., Valtierra-Rodriguez, M. & Adeli, H. 2018. Wireless Smart Sensors for Monitoring the Health Condition of Civil Infrastructure. *Scientia Iranica*, Vol 25, No 6, pp 2913-2925.

Annamdas, V. G. M., Bhalla, S. & Soh, C. K. 2017. Applications of Structural Health Monitoring Technology in Asia. *Structural Health Monitoring*, Vol 16, No 3.

Arduino. 2024. Arduino Nano 33 IoT Product Reference Manual. Accessed 26 March 2024, < https://docs.arduino.cc/resources/datasheets/ABX00027-datasheet.pdf >.

Barrias, A., Casas, J. R. & Villalba, S. 2016. A Review of Distributed Optical Fiber Sensors for Civil Engineering Applications. *Sensors*, Vol 16, No 5.

Berrocal, C. G., Fernandez, I., Bado M. F., Casas, J. R. & Rempling, R. 2021. Assessment and Visualization of Performance Indicators of Reinforced Concrete Beams by Distributed Optical Fibre Sensing. *Structural Health Monitoring*, Vol 20, No 6.

Boller, C., Chang, F.-K. & Fujino, Y. 2009. Encyclopaedia of Structural Health Monitoring. 1st ed. John Wiley and Sons, Chichester, UK.

BS (British Standard) 1881-121: 1983. *Testing Concrete Part 121. Method for Determination of Static Modulus of Elasticity In Compression*. 1 ed. Pretoria: British Standards Institution.

Cawley, P. 2001. Non-Destructive Testing – Current Capacities and Future Directions. *Proceedings of the Institution of Mechanical Engineers, Part L: Journal of Materials: Design and Applications*, Vol 215, No 4, pp 213-223.

Cha, G., Park, S. & Oh, T. 2019. A Terrestrial LiDAR-Based Detection of Shape Deformation for Maintenance of Bridge Structures. *Journal of Construction Engineering and Management*, Vol 145, No 12, pp 213-223.

Chacón, R., Casas, J. R., Ramonell, C., Posada, H. Stipanovic, I. & Skaric, S. 2023. Requirements and Challenges for Infusion of SHM Systems within Digital Twin Platforms. *Structure and Infrastructure Engineering*, pp 1-17.

Chen, Y. & Xue, X. 2018. Advances in the Structural Health Monitoring of Bridges using Piezoelectric Transducers. *Sensors*, Vol 18, No 12.

de Battista, N., Brownjohn, J. M. W., Tan, H. P. & Koo, K. Y. 2014. Measuring and Modelling the Thermal Performance of the Tamar Suspension Bridge using a Wireless Sensor Network. *Structure and Infrastructure Engineering*, Vol 11, No 2, pp 176-193.

de Castro, B. A., Baptista, F. G. & Ciampa, F. 2019. Comparative Analysis of Signal Processing Techniques for Impedance-Based SHM Applications in Noisy Environments. *Mechanical Systems and Signal Processing*, Vol 126, No 1, pp 326-340.

DoT (Department of Transport). 2017. *National Rail Policy Draft White Paper*. Pretoria: Department of Transport. Pretoria.

EFBElektronik. 2024. Simplex Fiber Optic Patch Cable E2000, Accessed 16 March 2024, < https://www.efb-elektronik.de/en/download/datasheet/?productNumber=O0834.10 >.

Elfick, J. 2024. School Science Lessons. *School of Education, University of Queensland*, Accessed 26 January 2024, < https://johnelfick.github.io/school-science-lessons >.

Erdélyi, J., Kopáčik, A. & Kyrinovič, P. 2020. Spatial Data Analysis for Deformation Monitoring of Bridge Structures. *Applied Sciences*, Vol 10, No 23.

Errandonea, I., Beltrán, S. & Arrizabalaga, S. 2020. Digital Twin for Maintenance: A Literature Review. *Computers in Industry*, Vol 123, No 1.

ETI Systems. 2024. Linear Potentiometers: Unlocking Precision Measurement and Control. Accessed 06 February 2025, < https://etisystems.com/linearpotentiometers/ >.

Feng, D. & Feng, M. Q. 2020. Computer Vision for SHM of Civil Infrastructure: From Dynamic Response Measurement to Damage Detection – A Review. *Engineering Structures*, Vol 156, No 1, pp 105-117.

fibrisTerre. 2024. fTB 2505 Fiber-Optic Sensing System for Distributed Strain and Temperature Monitoring, Accessed 16 March 2024, < https://d3pcsg2wjq9izr.cloudfront.net/files/48898/download/348831/1-fibrisTerre_flyer.pdf >.

Garetti, M., Rosa, P. & Terzi, S. 2012. Life Cycle Simulation for the Design of Product-Service Systems. *Computers in Industry*, Vol 63, No 4, pp 361-369.

Gentile, C. & Bernardini, G. 2008. An Interferometric Radar for Non-Contact Measurement of Deflections on Civil Engineering Structures: Laboratory and Full-Scale Tests. *Structure and Infrastructure Engineering*, Vol 6, No 5, pp 521-534.

Giurgiutiu, V. & Soutis, C. 2012. Enhanced Composites Integrity Through Structural Health Monitoring. *Applied Composite Materials*, Vol 19, No 1, pp 813-829.

Graybeal, B. A., Phares, B. M., Rolander, D. D., Moore, M. & Washer, G. 2002. Visual Inspection of Highway Bridges. *Journal of Nondestructive Evaluation*, Vol 21, No 1, pp 67-83.

Guan, S., Bridge, J. A., Li, C. & DeMello, N. J. 2018. Smart Radar Sensor Network for Bridge Displacement Monitoring. *Journal of Bridge Engineering*, Vol 24, No 1.

Guan, S., Rice, J., Li, C. & Wang, G. 2014. Bridge Deflection Monitoring Using Small, Low-Cost Radar Sensors. *Proceedings of the Structures Congress (American Society of Civil Engineers)*, Boston, Massachusetts, USA.

Guerriero, L., Guerriero, G., Grelle, G., Guadagno, F. M. & Revellino, P. 2017. Brief Communication: A Low Cost Arduino®-Based Wire Extensometer for Earth Flow Monitoring. *Natural Hazards and Earth System Sciences Discussions*, Vol 1, pp 1-8.

Gupta, B. D. 2006. Fiber Optic Sensors: Principles and Applications. 1st ed. New India Publishing Agency, Pitampura, New Delhi.

Hassani, S. & Dackermann, U. 2023. A Systematic Review of Advanced Sensor Technologies for Non-Destructive Testing and Structural Health Monitoring. *Sensors*, Vol 23, No 4.

Hawley, C. J. & Gräbe, P. J. 2021. *Water Leakage Mapping in Concrete Railway Tunnels Using LiDAR Generated Point Clouds*. Master of Engineering dissertation, Department of Civil Engineering, University of Pretoria, South Africa.

Hemdan, E. E.-D., El-Shafai, W. & Sayed, A. 2023. Integrating Digital Twins with IoT-Based Block Chain: Concept, Architecture, Challenges, and Future Scope. *Wireless Personal Communications*, Vol 131, No 1, pp 2193-2216.

Huang, J. & Markou, G. 2024. SMART Monitoring of Structures (Digital Twin, Live Data and Assessment). Accessed 22 March 2024, < https://www.youtube.com/watch?v=SFZJZcM0xr4 >.

Hung, S. L., Ding, J. T. & Lu, Y. C. 2019. Developing an Energy-Efficient and Low-Delay Wake-Up Wireless Sensor Network-Based Structural Health Monitoring System Using On-Site

Earthquake Early Warning System and Wake-On Radio. *Journal of Civil Structural Health Monitoring*, Vol 9, No 1, pp 103-115.

Interlab. 2024. Solifos BRUsens V9, Accessed 13 March 2024, < https://www.interlab.pl/en/product/solifos-brusens-v9.html#opis >.

Jasinski, M., Lazinski, P. & Piotrowski, D. 2023. The Concept of Creating Digital Twins of Bridges Using Load Tests. *Sensors*, Vol 23, No 17.

Joshi, S. & Harle, S. M. 2017. Linear Variable Differential Transducer (LVDT) & Its Applications in Civil Engineering. *International Journal of Transportation Engineering and Technology*, Vol 3, No 4.

Joynt, H. 2019. Some Reflections on Transport Infrastructure Delivery in South Africa. *Journal of Transport and Supply Chain Management*, Vol 13, No 0.

Ju, M., Dou, Z., Li, J.-W., Qiu, X., Shen, B., Zhang, D., Yao, F.-Z., Gong, W. & Wang, K. 2023. Piezoelectric Materials and Sensors for Structural Health Monitoring: Fundamental Aspects, Current Status, and Future Perspectives. *Sensors*, Vol 23, No 1.

Kaartinen, E., Dunphy, K. & Sadhu, A. 2022. LiDAR-Based Structural Health Monitoring: Applications in Civil Infrastructure Systems. *Sensors*, Vol 22, No 12.

Karbhari, V. M. & Ansari, F. 2009. Structural Health Monitoring of Civil Infrastructure Systems. 1st ed. Woodhead Publishing Limited, Cambridge, UK.

Kee, S.-H. & Zhu, J. 2013. Using Piezoelectric Sensors for Ultrasonic Pulse Velocity Measurements in Concrete. *Smart Materials and Structures*, Vol 22, No 11.

Kim, I.-H., Jeon, H., Baek, S.-C., Hong, W.-H. & Jung, H.-J. 2018. Application of Crack Identification Techniques for an Aging Concrete Bridge Inspection Using an Unmanned Aerial Vehicle. *Sensors*, Vol 18, No 6, pp 587-608.

Kinet, D., Mégret, P., Goossen, K. W., Qiu, L., Heider, D., & Caucheteur, C. 2014. Fiber Bragg Grating Sensors toward Structural Health Monitoring in Composite Materials: Challenges and Solutions. *Sensors*, Vol 14, No 4, pp 7394-7419.

Kotsovos, M. D. & Pavlovic, M. N. 1995. *Structural Concrete. Finite Element Analysis for Limit State Design*. London.

Lopez-Higuera, J. M., Cobo, L. R., Incera, A. Q. & Cobo, A. 2011. Fiber Optic Sensors in Structural Health Monitoring. *Journal of Lightwave Technology*, Vol 29, No 4, pp 587-608.

Liu, P., Hu, Y., Chen, Y., Geng, B. & Xu, D. 2020. Investigation of Novel Embedded Piezoelectric Ultrasonic Transducers on Crack and Corrosion Monitoring of Steel Bar. *Construction and Building Materials*, Vol 235, No 1.

Liu, C., Zhang, P. & Xu, X. 2023. Literature Review of Digital Twin Technologies for Civil Infrastructure. *Journal of Infrastructure Intelligence and Resilience*, Vol 2, No 3.

Lynch, J. P. 2007. An Overview of Wireless Structural Health Monitoring for Civil Structures. *Mathematical, Physical and Engineering Sciences*, Vol 365, No 1851, pp 345-372.

Ma, Z., Choi, J. & Sohn, H. 2023. Structural Displacement Sensing Techniques for Civil Infrastructure: A review. *Journal of Infrastructure Intelligence and Resilience*, Vol 2, No 3.

Mahmoodian, M., Shahrivar, F., Setunge, S. & Mazaheri, S. 2022. Development of Digital Twin for Intelligent Maintenance of Civil Infrastructure. *Sustainability*, Vol 14, No 14.

Majumder, M., Gangopadhyay, T. K., Chakraborty, A. K., Dasgupta, K. & Bhattacharya, D. K. 2008. Review Fibre Bragg Gratings in Structural Health Monitoring – Present Status and Applications. *Sensors and Actuators*, Vol 147, No 1, pp 150-164.

Markou, G. 2011. *Detailed Three-Dimensional Nonlinear Hybrid Simulation for the Analysis of Full-Scale Reinforced Concrete Structures*. PhD thesis, Institute of Structural Analysis and Seismic Research, National Technical University of Athens.

Markou, G. & Papadrakakis, M. 2010. Detailed Three-Dimensional Modelling of Reinforced Concrete Structures. *9th HSTAM International Congress on Mechanics*, Limassol, Cyprus.

Matta, F., Bastianini, F., Galati, N., Casadei, P. & Nanni, A. 2008. Distributed Strain Measurement in Steel Bridge With Fiber Optic Sensors: Validation Through Diagnostic Load Test. *Journal of Performance of Constructed Facilities*, Vol 22, No 4.

Mayunga, S. D. & Bakaone, M. 2021. Dynamic Deformation Monitoring of Lotsane Bridge Using Global Positioning Systems (GPS) and Linear Variable Differential Transducers (LVDT). *Journal of Data Analysis and Information Processing*, Vol 9, No 1, pp 30-50.

McCormick, N. & Lord, J. 2010. Digital Image Correlation. *Materials Today*, Vol 13, No 12, pp 52-54.

McEnteggart, I. (2008). *Springer Handbook of Experimental Solid Mechanics*. Boston, Massachusetts.

Mohammad, T. 2009. Using Ultrasonic and Infrared Sensors for Distance Measurement. *World Academy of Science, Engineering and Technology Conference*, Hong Kong, China.

Mourlas, C. & Markou, G. 2020. ReConAn V2.00 Finite Element Analysis Software User's Manual. Accessed 24 April 2023, < https://www.researchgate.net/publication/342361609_ReConAn_v200_Finite_Element_Analysis_Software_User's_Manual >.

Mustapha, S., Lu, Y., Ng, C.-T. & Malinowski, P. 2021. Sensor Networks for Structures Health Monitoring: Placement, Implementations, and Challenges – A Review. *Vibration*, Vol 4, No 3.

Nagarajaiah, S. & Erazo, K. 2016. Structural Monitoring and Identification of Civil Infrastructure in the United States. *Structural Monitoring and Maintenance*, Vol 3, No 1, pp 51-69.

Nhung, N. T. C., Vu, L. V., Nguen, H. Q., Huyen, D. T., Nguyen, D. B. & Quang, M. T. 2023. Development and Application of Linear Variable Differential Transformer (LVDT) Sensors for the Structural Health Monitoring of an Urban Railway Bridge in Vietnam. *Engineering, Technology & Applied Science Research*, Vol 13, No 5, pp 11622-11627.

Nonis, C., Niezrecki, C., Yu, T.-Y., Ahmed, S., Su, C.-F. & Schmidt, T. 2013. Structural Health Monitoring of Bridges Using Digital Image Correlation. *SPIE Health Monitoring of Structural and Biological Systems (Proc. SPIE 8695)*, San Diego, California, USA.

Nurmi, S., Hoult, N. A. & Howell, S. D. 2016. Distributed Strain Monitoring of Two-Way Slabs. *Engineering Structures*, Vol 189, No 1, pp 580-588.

Pan, B. & Tian, L. 2016. Advanced Video Extensometer for Non-Contact, Real-Time, High-Accuracy Strain Measurement. *Optics Express*, Vol 24, No 17, pp 19082-19093.

Pineau, C., Barré, F., Chatzigogos, C. T., Courtois, A., Contrafatto, M., Sampic, L., Simon, C. & Galan, M. 2024. In-situ Behaviour of Nuclear Reactor Building Rafts on Soft Soils – Review of Available Monitoring Data and Comparative Analysis with Original Design Assumptions. *European Journal of Environmental and Civil Engineering*, Vol 28, No 13, pp 3035-3053.

Polonelli, T., Brunelli, D., Guermandi, M. & Benini, L. 2018. An Accurate Low-Cost Crack meter with LoRaWAN Communication and Energy Harvesting Capability. *IEEE 23rd International Conference on Emerging Technologies and Factory Automation (ETFA)*, Turin, Italy.

Raj, T., Hashim, F. H., Huddin, A. B., Ibrahim, M. F. & Hussain, A. 2020. A Survey on LiDAR Scanning Mechanisms. *Electronics*, Vol 9, No 5.

Rashidi, M., Mohammadi, M., Kivi, S. S., Abdolvand, M. M., Linh, T.-H. & Samali, B. 2020. A Decade of Modern Bridge Monitoring Using Terrestrial Laser Scanning: Review and Future Directions. *Remote Sensing*, Vol 12, No 22.

Rehman, S. K. U., Ibrahim, Z., Memon, S. A. & Jameel, M. 2015. Non-Destructive Test Methods for Concrete Bridges: A review. *Construction and Building Materials*, Vol 107, pp 58-86.

Reagan, D., Sabato, A. & Niezrecki, C. 2017. Unmanned Aerial Vehicle Acquisition of Three-Dimensional Digital Image Correlation Measurements for Structural Health Monitoring of Bridges. *Nondestructive Characterization and Monitoring of Advanced Materials, Aerospace, and Civil Infrastructure (Proc. SPIE 10169)*. Portland, Oregon, USA.

Ribeiro, D., Calçada, R., Ferreira, J. & Martins, T. 2014. Non-Contact Measurement of the Dynamic Displacement of Railway Bridges Using an Advanced Video-Based System. *Engineering Structures*, Vol 75, No 1, pp 164-180.

Richards, M. A., Scheer, J. A. & Holm, W. A. 2010. Principles of Modern Radar. Volume I – Basic Principles. 1st ed. SciTech Publishing Inc., Raleigh, USA.

Ritto, T. & Rochinha, F. 2021. Digital Twin, Physics-Based Model, and Machine Learning Applied to Damage Detection in Structures. *Mechanical Systems and Signal Processing*, Vol 155, No 1.

RS. 2023. A Complete Guide to Potentiometers. Accessed 01 October 2023, < https://uk.rs-online.com/web/content/discovery/ideas-and-advice/potentiometers-guide#related-guides >.

Rupitsch, S. J. 2019. Piezoelectric Sensors and Actuators. 1st ed. Springer Berlin, Heidelberg.

Sabri, N., Aljunid, S. A., Salim, M. S., Ahmad, R. B. & Kamaruddin, R. 2013. Toward Optical Sensors: Review and Applications. *Journal of Physics: Conference Series*, Vol 423, No 1.

SAICE (South African Institution of Civil Engineering). 2017. *SAICE Infrastructure Report Card for South Africa*: 2017. Issue 3. Midrand.

SAICE. 2022. *SAICE Infrastructure Report Card for South Africa*: 2022. Issue 4. Midrand.

SANS (South African National Standard) 5860: 2006. *Concrete Tests – Dimensions, Tolerances and Uses of Cast Test Specimens*. 1.1 ed. Pretoria: South African Bureau of Standards.

SANS 5861-1: 2006. *Concrete Tests Part 1: Mixing Fresh Concrete in the Laboratory*. 2.1 ed. Pretoria: South African Bureau of Standards.

SANS 5863: 2006. *Concrete Tests – Compressive Strength of Hardened Concrete*. 2.1 ed. Pretoria: South African Bureau of Standards.

SANS 6253: 2006. *Concrete Tests – Tensile Splitting Strength of Concrete*. 1.1 ed. Pretoria: South African Bureau of Standards.

Schwab, K. 2017. The Fourth Industrial Revolution. 1st ed. World Economic Forum, Switzerland.

Schweber, B. 2021. The Fundamentals of Digital Potentiometers and How to Use Them, Accessed 17 March 2024, < https://www.digikey.com/en/articles/the-fundamentals-of-digital-potentiometers >.

Sharp. 2024. Distance Measuring Sensor Unit GP2Y0A41SK0F. Accessed 23 March 2024, < https://global.sharp/products/device/lineup/data/pdf/datasheet/gp2y0a41sk_e.pdf >.

Shim, C.-S., Dang, N.-S., Lon, S. & Jeon, C.-H. 2019. Development of a Bridge Maintenance System for Prestressed Concrete Bridges Using 3D Digital Twin Model. *Structure and Infrastructure Engineering*, Vol 15, No 10, pp 1319-1332.

Siemens. 2023. Simcenter Femap Software. Accessed 25 April 2023, < https://plm.sw.siemens.com/en-US/simcenter/mechanical-simulation/femap/ >.

Sikandar, H., Vaicondam, Y., Khan, N., Qureshi, M. I. & Ullah, A. & 2021. Scientific Mapping of Industry 4.0 Research: A Bibliometric Analysis. *International Journal of Interactive Mobile Technologies*, Vol 15, No 18, pp 129-147.

Song, S., Hou, Y., Guo, M., Wang, L., Tong, X. & Wu, J. 2017. An Investigation on the Aggregate-Shape Embedded Piezoelectric Sensor for Civil Infrastructure Health Monitoring. *Construction and Building Materials*, Vol 131, pp 57-65.

Sony, S., Laventure, S. & Sadhu, A. 2019. A Literature Review of Next-Generation Smart Sensing Technology in Structural Health Monitoring. *Structural Control Health Monitoring*, Vol 26, No 3.

Spencer, B. F., Park, J.-W., Mechitov, K. A., Jo, H. & Agha, G. 2017. Next Generation Wireless Smart Sensors Toward Sustainable Civil Infrastructure. *Procedia Engineering*, Vol 171, No 1, pp 5-13.

Sun, M., Staszewski, W. J. & Swamy, R. N. 2010. Smart Sensing Technologies for Structural Health Monitoring of Civil Engineering Structures. *Advances in Civil Engineering*, Vol 2010, No 1.

Tekinerdogan, B. & Verdouw, C. 2020. Systems Architecture Design Pattern Catalogue for Developing Digital Twins. *Sensors*, Vol 20, No 18.

Todd, C.D. 1976. *The Potentiometer Handbook*. 1st ed. McGraw-Hill. New York.

Trojaniello, D., Cereatti, A., Bourke, A. K., Aminian, K. & Croce, U. D. 2014. A Wearable System for the Measurement of the Inter-Foot Distance During Gait. *IMEKO TC-4 International Symposium*, Benevento, Italy.

Tseng, K. K.-H., Soh, C. K., Gupta, A. & Bhalla, S. 2000. Health Monitoring of Civil Infrastructure Using Smart Piezoceramic Transducer Patches. *Computational Methods for Smart Structures and Materials II*, Vol 46, No 1, pp 153-162.

Valença, J., Puente, I., Júlio, E., González-Jorge, H. & Arias-Sánchez, P. 2017. Assessment of Cracks on Concrete Bridges Using Image Processing Supported by Laser Scanning Survey. *Construction and Building Materials*, Vol 146, No 1, pp 668-678.

Variohm Eurosensor. 2024. IPL Linear Position Sensor. Accessed 17 March 2024, < https://www.farnell.com/datasheets/1833199.pdf >.

Visual Studio Code. 2024. Learn to Code with Visual Studio Code. Accessed 02 May 2024, < https://code.visualstudio.com/learn >.

Voutetaki, M. E., Naoum, M. C., Papadopoulos, N. A. & Chalioris, C. E. 2022. Cracking Diagnosis in Fiber-Reinforced Concrete with Synthetic Fibers Using Piezoelectric Transducers. *Fibers*, Vol 10, No 1.

Wang, M. L. & Yim, J. 2010. Monitoring of the I-39 Kishwaukee Bridge. *Civil Engineering Studies, Illinois Centre for Transportation Series (10-061)*.

Webb, G. T., Vardanega, P. J., Hoult, N. A., Fidler, P. R. A., Bennett, P. J. & Middleton, C. R. 2017. Analysis of Fiber-Optic Strain-Monitoring Data from a Prestressed Concrete Bridge. *Journal of Bridge Engineering*, Vol 22, No 5.

Wilmshurst, T. 2010. *Designing Embedded Systems with PIC Microcontrollers Principles and Applications*. 2nd ed. Elsevier, India.

Wu, S.-T., Mo, S.-C. & Wu, B.-S. 2008. An LVDT-Based Self-Actuating Displacement Transducer. *Sensors and Actuators A: Physical*, Vol 141, No 2.

Wu, T., Liu, G., Fu, S. & Xing, F. 2020. Recent Progress of Fiber-Optic Sensors for the Structural Health of Civil Infrastructure. *Sensors*, Vol 20, No 16.

Wu, Q., Okabe, Y. & Yu, F. 2018. Ultrasonic Structural Health Monitoring Using Fiber Bragg Grating. *Sensors*, Vol 18, No 10.

Ye, C., Butler, L. J., Elshafie, M. Z. E. B. & Middleton, C. R. 2020. Evaluating Prestress Losses in a Prestressed Concrete Girder Railway Bridge Using Distributed and Discrete Fibre Optic Sensors. *Construction and Building Materials*, Vol 247, No 1.

Yu, L., Santoni-Bottai, G., Xu, B., Liu, W. & Giurgiutiu, V. 2008. Piezoelectric Wafer Active Sensors for In Situ Ultrasonic-Guided Wave SHM. *Fatigue & Fracture of Engineering Materials & Structures*, Vol 31, No 8, pp 611-628.

Yu, S., Li, D. & Ou, J. 2022. Digital Twin-Based Structural Hybrid Monitoring and Fatigue Evaluation of Orthotropic Steel Deck in Cable-Stayed Bridge. *Structural Control Health Monitoring*, Vol 29, No 8.

Zhang, G., Wu, Y., Zhao, W. & Zhang, J. 2020. Radar-Based Multipoint Displacement Measurements of a 1200-m-Long Suspension Bridge. *ISPRS Journal of Photogrammetry and Remote Sensing*, Vol 167, No 1, pp 71-84.

Zhang, W., Zhang, M., Lan, Y., Zhao, Y., & Dai, W. 2020. Detection of Crack Locations in Aluminum Alloy Structures Using FBG Sensors. *Sensors*, Vol 20 No 2.

Zhang, Z. & Sun, C. 2021. Structural Damage Identification Via Physics-Guided Machine Learning: A Methodology Integrating Pattern Recognition with Finite Element Model Updating. *Structural Health Monitoring*, Vol 20, No 4, pp 1675-1688.

A APPENDIX

This appendix serves to provide supplementary data and referencing information where required. It is organised into sections to offer further substantiation and detail for the methods, procedures, and results discussed in the main chapters of this thesis.

A.1 CONCRETE CUBE AND CYLINDER SAMPLE TEST

The following subsections outline the test methods employed on the concrete cube and cylinder samples to determine the concrete characteristic compressive strength, elastic modulus, and tensile strength based on the relevant clauses of the South African National Standards (SANS) and British Standards (BS).

A.1.1 Compressive Strength of Concrete Cube based on SANS 5863: 2006

The compressive strength of the concrete is determined by conducting a compressive test on the concrete cube samples. During testing, an increasing compression load is gradually applied to the 150 mm × 150 mm × 150 mm concrete cube samples at a normal rate of 0.3 MPa/s ±0.1 MPa/s until the specimen fails.

The following equation was used in calculating the compressive strength of the concrete cube sample:

$$f_{cc} = \frac{F}{A_c} \qquad \text{(Eq. A.1)}$$

Where:

f_{cc} = Compressive cube strength (MPa)

F = Maximum recorded load at failure (N)

A_C = Cross-sectional area of the cube which the compressive force acts (mm^2)

The average compressive strength of the cube samples is recorded to the nearest 0.5 MPa.

A.1.2 Compressive Static Modulus of Elasticity of Concrete Cylinder based on BS 1881-121: 1983

The modulus of elasticity in compression (also known as the secant modulus) is determined by applying a compressive, elastic force to the concrete cylinder samples. During testing, the differences in stresses Δ_σ and strains Δ_ε of the cylinder sample between the lower and upper loading levels are determined and used in the calculation of the static modulus of elasticity.

In this study, 100 mm diameter × 200 mm long concrete cylinder samples were tested. The lower loading stress level of 1.27 MPa (equivalent to 10 kN), and an upper loading stress level of one-third of the compressive cylindrical strength were applied. The reference displacement at each loading level was subsequently recorded and used to determine the mean strains (ε_U and ε_L).

Prior to the compressive cylinder test, all cylinder samples were initially subjected to three loading and un-loading cycles in a range between the lower and upper loading levels.

The following equation was used in calculating the static modulus of elasticity in compression of the concrete cylinder sample:

$$E_c = \frac{\Delta_\sigma}{\Delta_\varepsilon} = \frac{\sigma_U - \sigma_L}{\varepsilon_U - \varepsilon_L} \qquad \text{(Eq. A.2)}$$

Where:

E_c = Compressive static modulus of elasticity (MPa)

σ_U = Upper loading stress (MPa), estimated by (0.8 × f_{cc})/3

σ_L = Lower loading stress (1.27 MPa)

ε_U = Mean strain under upper loading stress

ε_L = Mean strain under lower loading stress

The average static modulus of elasticity of the cylinder samples is recorded to the nearest 500 MPa for values exceeding 10 000 MPa.

A.1.3 Tensile Splitting Strength of Concrete Cylinder based on SANS 6253: 2006

The tensile splitting strength of the concrete is determined by conducting a compressive test on the concrete cylinder samples. During testing, an increasing compression load is gradually applied to the 100 mm diameter × 100 mm (approximately) long concrete cylinder samples at a normal rate of 0.03 MPa/s ±0.01 MPa/s until the specimen fails.

The following equation was used in calculating the tensile splitting strength of the concrete cylinder sample:

$$f_{ct} = \frac{2F}{\pi \times L_c \times d_c} \quad \text{(Eq. A.3)}$$

Where:

f_{ct} = Tensile splitting cylinder strength (MPa)

F = Maximum recorded load at failure (N)

L_c = Length of the cylinder specimen (mm)

d_c = Cross-sectional dimension of the cylinder specimen (mm)

The average tensile splitting strength of the cylinder samples is recorded to the nearest 0.05 MPa.

A.2 ELECTRICAL CIRCUIT CONFIGURATION

Figure A-1 illustrates the detailed electrical circuit connection configuration between the Arduino Nano 33 IoT microcontroller and the contact and non-contact sensors.

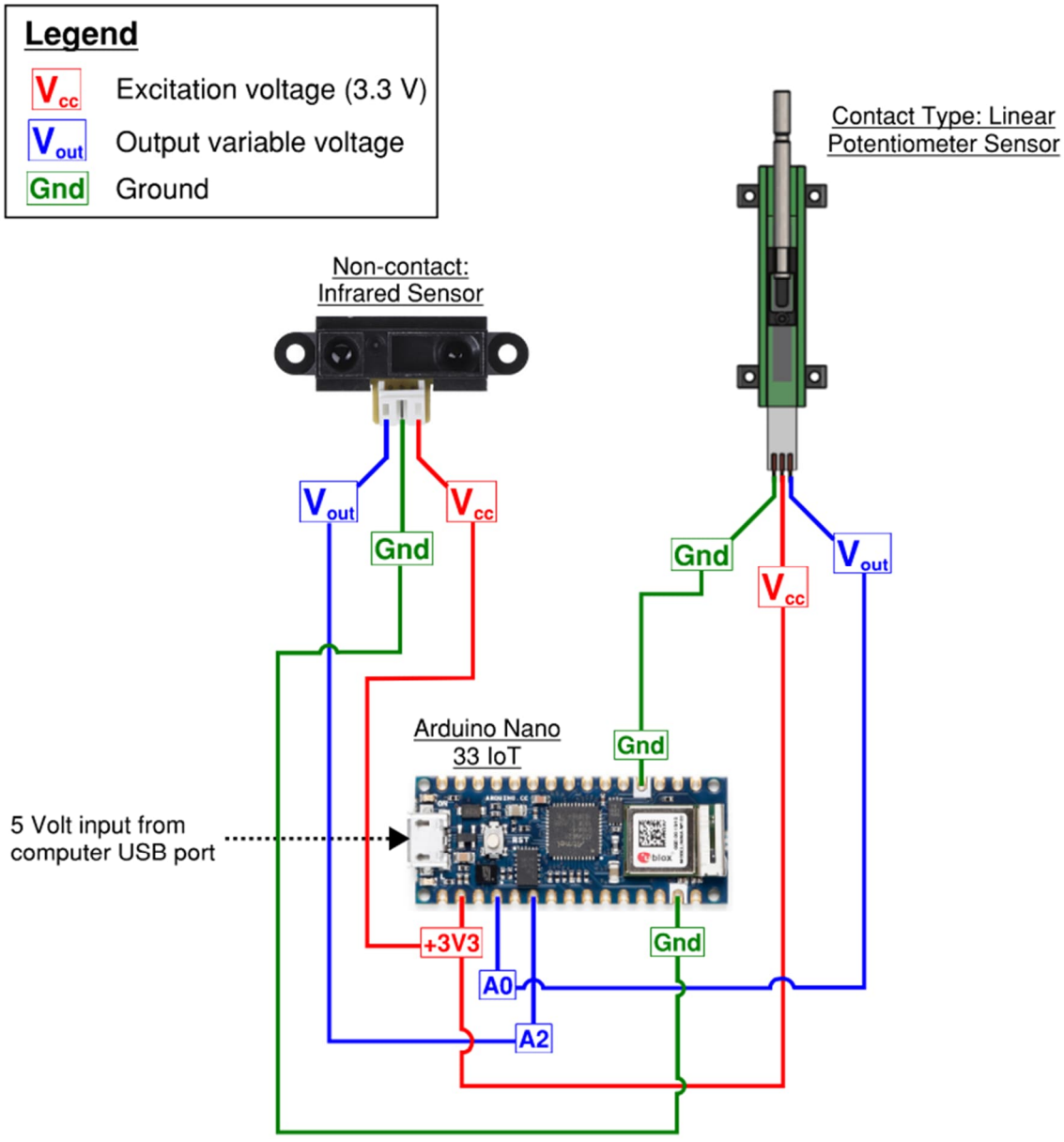

Figure A-1: Electrical circuit connection configuration between the Arduino and displacement sensors

A.3 ARDUINO CLOUD SKETCH

The sketch (programming code), assigned to the Arduino Nano 33 IoT microcontroller edited in Arduino's online IDE cloud platform is shown below.

```
void setup() {
  // Initialize serial and wait for port to open:
  Serial.begin(9600);
  // This delay gives the chance to wait for a Serial Monitor without blocking if none is found
  delay(1500);
  // Defined in thingProperties.h
  initProperties();
  // Connect to Arduino IoT Cloud
  ArduinoCloud.begin(ArduinoIoTPreferredConnection);
  /*
     The following function allows you to obtain more information
     related to the state of network and IoT Cloud connection and errors
  */
  setDebugMessageLevel(2);
  ArduinoCloud.printDebugInfo();
}
// The loop function runs repeatedly
void loop() {
  ArduinoCloud.update();
  // Initialise containers
  potentiometer = 0;
  ir = 0;
  uint sensorValue = 0;
  // Potentiometer - Averaged ADC Digit reading of 250 samples
  sensorValue = 0;
  for (int i = 0; i <= 250; i++) {
    sensorValue = sensorValue + analogRead(A0);
    delay(4);     //wait 4 ms
  }
  potentiometer = sensorValue / 250;
  // IR sensor - Averaged ADC Digit reading of 250 samples
  sensorValue = 0;
```

```
  for (int i = 0; i <= 250; i++) {
    sensorValue = sensorValue + analogRead(A2);
    delay(4);     //wait 4 ms
  }
  ir = sensorValue / 250;
  // Print out the ADC digits for Pot and IR to computer via the COM port
  Serial.print(millis());
  Serial.print(",");
  Serial.print(potentiometer);
  Serial.print(",");
  Serial.println(ir);
}
```

The code is separated into two main sections, the setup and loop. The setup function is associated with the configuration and initialisation of the Arduino and only runs once when powering-on the board or when the reset button is pressed. The loop function is the main body of the code and runs repeatedly.

A.4 SENSOR CALIBRATION – ACCURACY

The data obtained from the accuracy calibration test of the potentiometer sensor is summarised in Table A-1 and Figure A-2.

Table A-1: Accuracy calibration test data of potentiometer

Applied Reference Displacement [mm]	Potentiometer Sensor	
	Reading	Measured Displacement [mm]
15.210	First	15.256
	Second	15.126
	Third	15.178
25.210	First	25.229
	Second	25.247
	Third	25.145
35.210	First	35.109
	Second	35.069
	Third	35.165
45.210	First	45.067
	Second	45.128
	Third	45.078

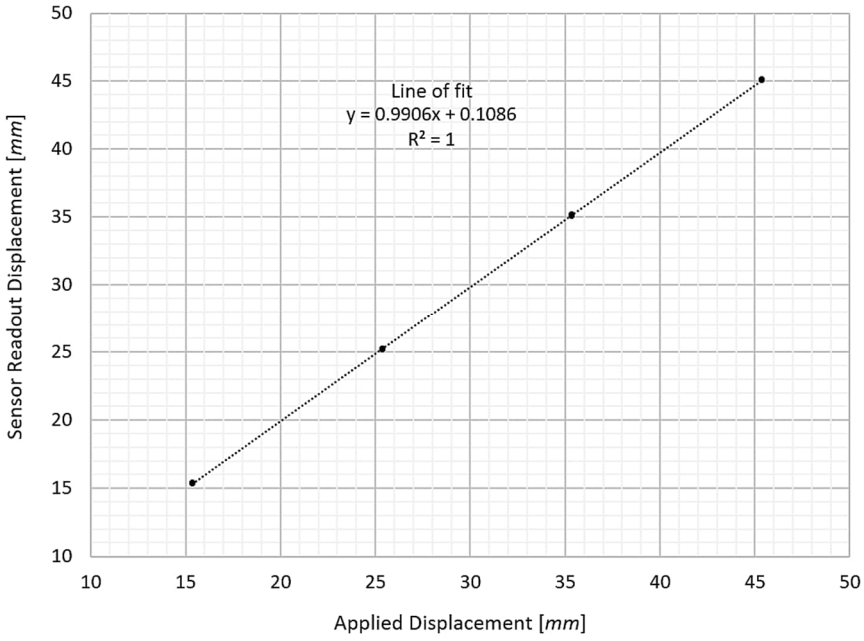

Figure A-2: Applied and measured displacement of potentiometer (accuracy calibration test)

The data obtained from the accuracy calibration test of the IR sensor is summarised in Table A-2 and Figure A-3.

Table A-2: Accuracy calibration test data of IR

Applied Reference Displacement [mm]	IR Sensor	
	Reading	Measured Displacement [mm]
15.870	First	16.431
	Second	16.460
	Third	16.488
25.870	First	26.194
	Second	26.205
	Third	26.184
35.870	First	36.391
	Second	36.322
	Third	36.423
45.870	First	45.916
	Second	45.925
	Third	45.973

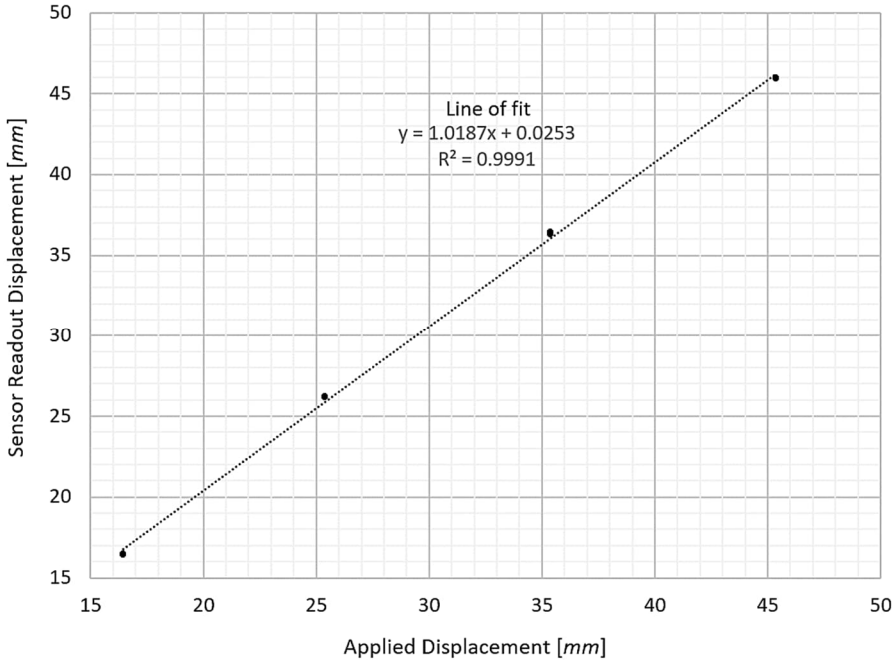

Figure A-3: Applied and measured displacement of IR sensor (accuracy calibration test)

A.5 SENSOR CALIBRATION – HYSTERESIS OF POTENTIOMETER

The hysteresis was determined using the same data obtained from the accuracy calibration test of the potentiometer sensor and is summarised in Table A-3. Hysteresis was calculated by comparing the maximum absolute difference between the loading and unloading measurements at each applied reference displacement point, relative to the total extension length of the potentiometer.

Table A-3: Hysteresis calibration test data of potentiometer

Load and Unload Cycle	Reference Displacement [mm]	Maximum Absolute Measurement Difference [µm]	Average Absolute Difference [µm]	Hysteresis (relative to total extension length) [%]	Average Hysteresis [%]
1	25.388	39.623	34.697	0.13	0.12
	35.388	23.982		0.08	
	45.388	40.486		0.14	
2	25.388	41.195	35.699	0.14	0.12
	35.388	23.049		0.08	
	45.388	42.854		0.14	
3	25.388	41.195	28.397	0.14	0.10
	35.388	12.204		0.04	
	45.388	31.791		0.11	
		Average Absolute Difference:	32.931 µm	**Average Hysteresis:**	0.11%

A.6 SENSOR CALIBRATION – NOISE

The data obtained from the calibration test of the potentiometer and IR sensors for noise is summarised in this appendix.

A.6.1 Potentiometer Sensor

The graphical representation of the measured ADC digit output for 1000 samples at three reference displacement points (at different rod extension lengths) are shown in Figure A-4, Figure A-5, and Figure A-6.

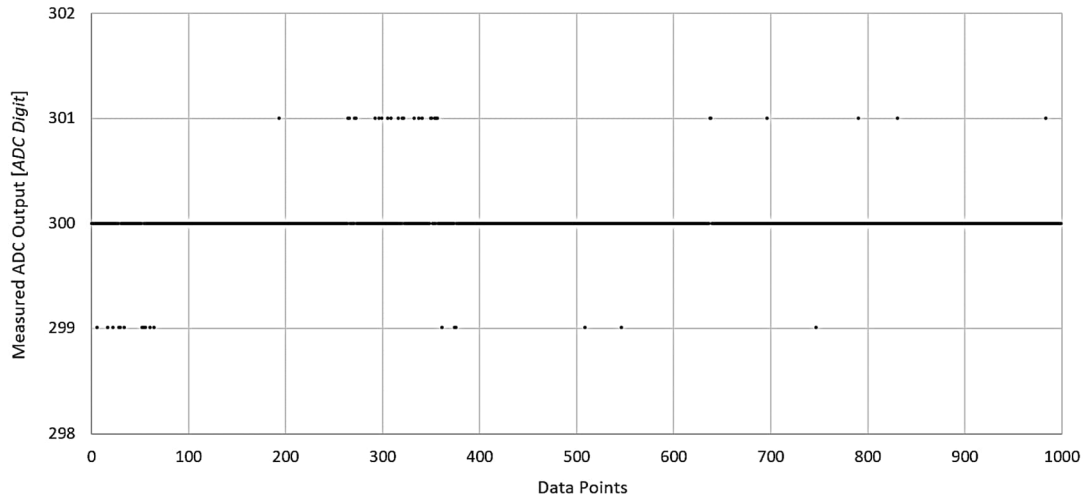

Figure A-4: Potentiometer sensor output ADC of 1000 samples at short rod extension at 300 ADC Digit (noise calibration test)

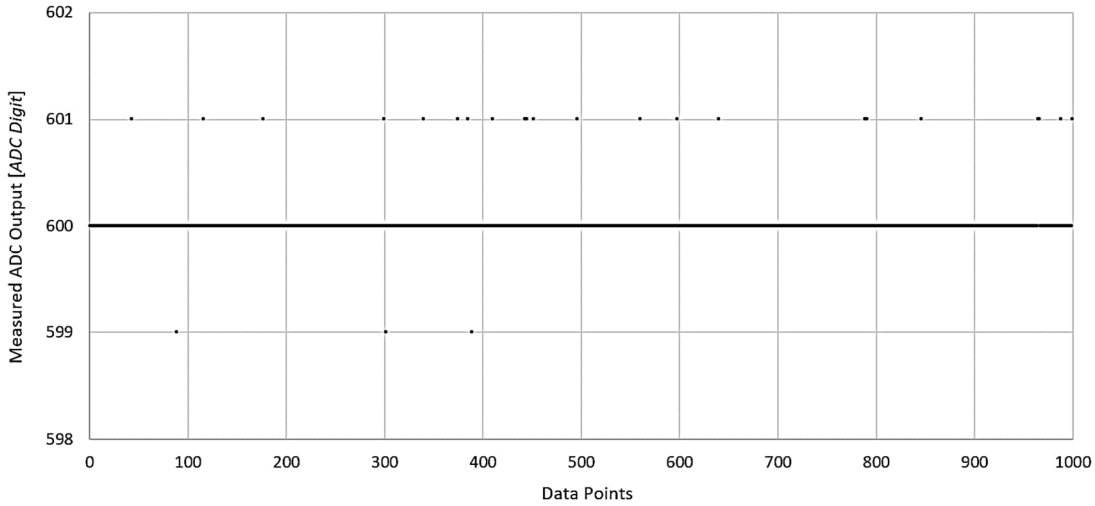

Figure A-5: Potentiometer sensor output ADC of 1000 samples at middle rod extension at 600 ADC Digit (noise calibration test)

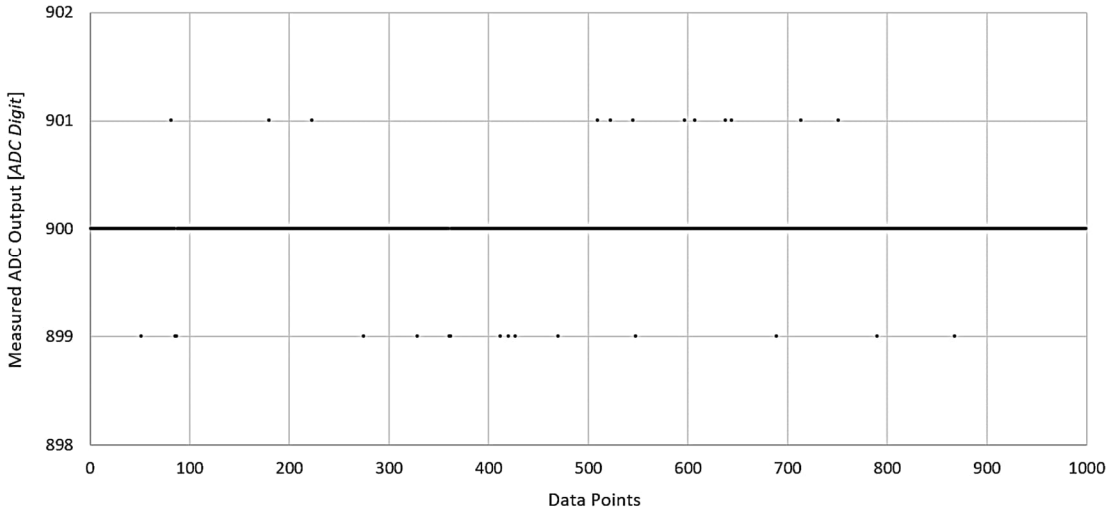

Figure A-6: Potentiometer sensor output ADC of 1000 samples at long rod extension at 900 ADC Digit (noise calibration test)

A.6.2 IR Sensor

The statistical results derived from 1000 ADC digit samples collected at four reference distances from the object, under various testing conditions, are summarised in Table A-4, Table A-5, Table A-6 and Table A-7. The typical graphical representations of the ADC digit sample, specifically at a reference distance of 70 mm between the IR sensor and the object, are provided in Figure A-7, Figure A-8, Figure A-9 and Figure A-10.

Table A-4: Statistical results of IR sensor's output ADC digit at various reference distances from the object (1000 samples) – normal concrete surface

Parameters	Object distance from IR Lens			
	30 mm	50 mm	70 mm	90 mm
Minimum Value	723.00	548.00	430.00	350.00
Maximum Value	725.00	551.00	433.00	354.00
Mode	724.00	549.00	431.00	352.00
Mean	724.066	549.058	431.204	352.205
Standard Deviation	285.9×10^{-3}	522.4×10^{-3}	434.2×10^{-3}	741.3×10^{-3}
Coefficient of Variance	0.395×10^{-3}	0.951×10^{-3}	1.007×10^{-3}	2.105×10^{-3}

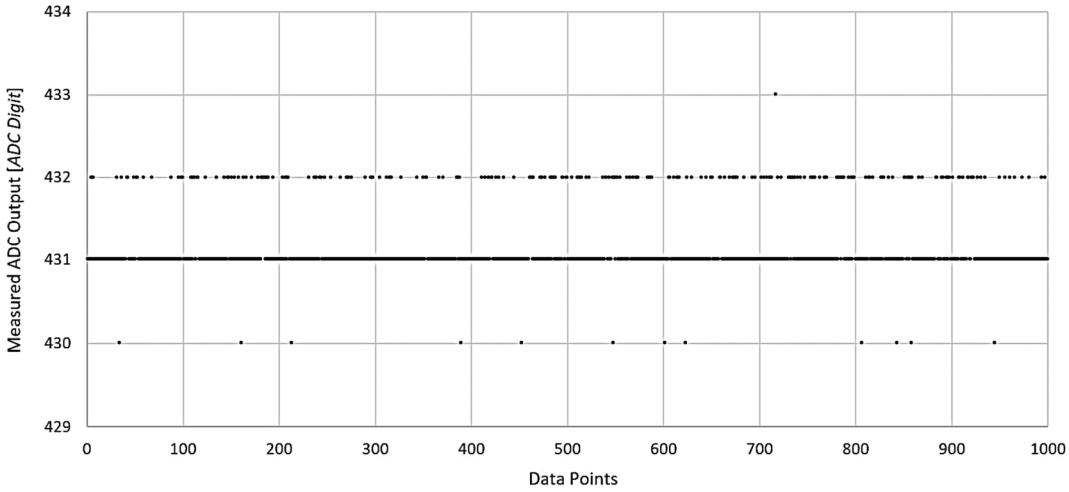

Figure A-7: IR sensor output ADC of 1000 samples at 70 mm reference distance for normal concrete surface (noise calibration test)

Table A-5: Statistical results of IR sensor's output ADC digit at various reference distances from the object (1000 samples) – acrylic white painted concrete surface

Parameters	Object distance from IR Lens			
	30 mm	50 mm	70 mm	90 mm
Minimum Value	722.00	545.00	429.00	348.00
Maximum Value	724.00	548.00	432.00	352.00
Mode	723.00	547.00	431.00	351.00
Mean	723.083	546.892	430.704	350.819
Standard Deviation	303.6×10^{-3}	436.5×10^{-3}	508.6×10^{-3}	600.5×10^{-3}
Coefficient of Variance	0.420×10^{-3}	0.798×10^{-3}	1.181×10^{-3}	1.712×10^{-3}

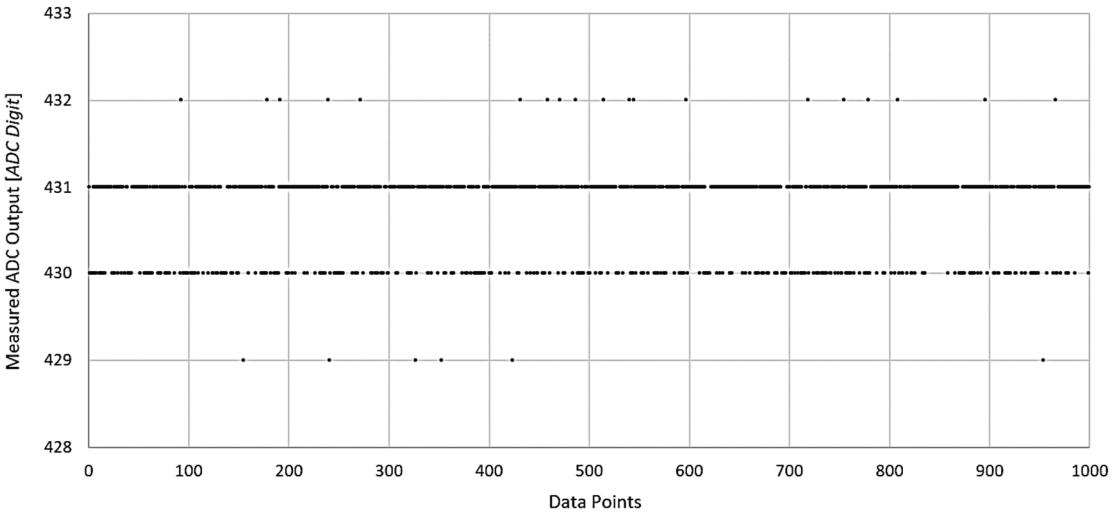

Figure A-8: IR sensor output ADC of 1000 samples at 70 mm reference distance for acrylic white painted concrete surface (noise calibration test)

Table A-6: Statistical results of IR sensor's output ADC digit at various reference distances from the object (1000 samples) – matte black painted concrete surface

Parameters	Object distance from IR Lens			
	30 mm	50 mm	70 mm	90 mm
Minimum Value	721.00	545.00	428.00	353.00
Maximum Value	722.00	548.00	432.00	356.00
Mode	722.00	547.00	431.00	354.00
Mean	721.718	546.697	430.594	354.199
Standard Deviation	450.2×10^{-3}	522.9×10^{-3}	549.1×10^{-3}	586.3×10^{-3}
Coefficient of Variance	0.624×10^{-3}	0.957×10^{-3}	1.275×10^{-3}	1.655×10^{-3}

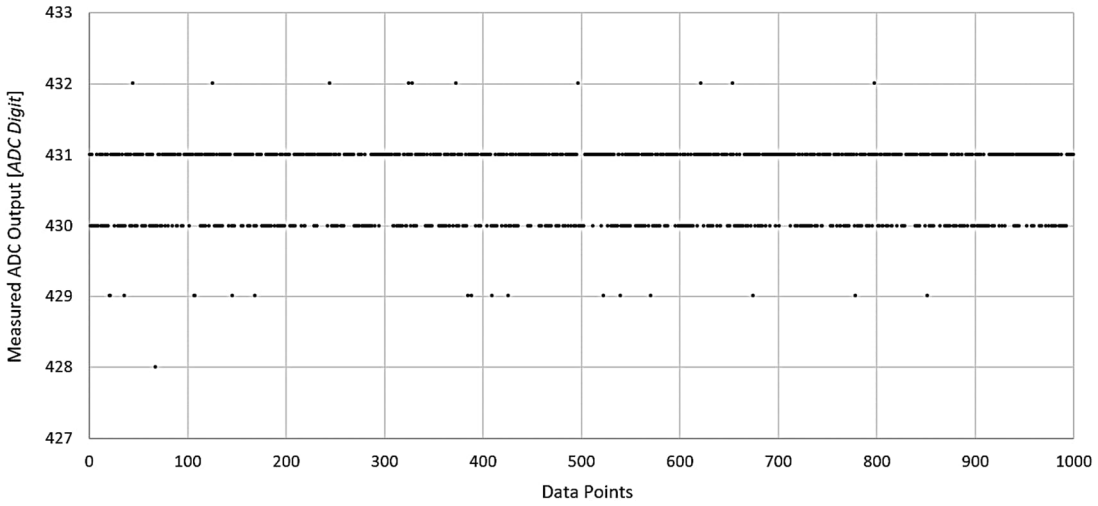

Figure A-9: IR sensor output ADC of 1000 samples at 70 mm reference distance for matte black painted concrete surface (noise calibration test)

Table A-7: Statistical results of IR sensor's output ADC digit at various reference distances from the object (1000 samples) – normal concrete surface with no light

Parameters	Object distance from IR Lens			
	30 mm	50 mm	70 mm	90 mm
Minimum Value	719.00	540.00	425.00	350.00
Maximum Value	721.00	543.00	427.00	353.00
Mode	720.00	541.00	426.00	352.00
Mean	719.979	541.099	425.951	351.584
Standard Deviation	395.9×10^{-3}	550.9×10^{-3}	405.9×10^{-3}	513.0×10^{-3}
Coefficient of Variance	0.550×10^{-3}	1.018×10^{-3}	0.953×10^{-3}	1.459×10^{-3}

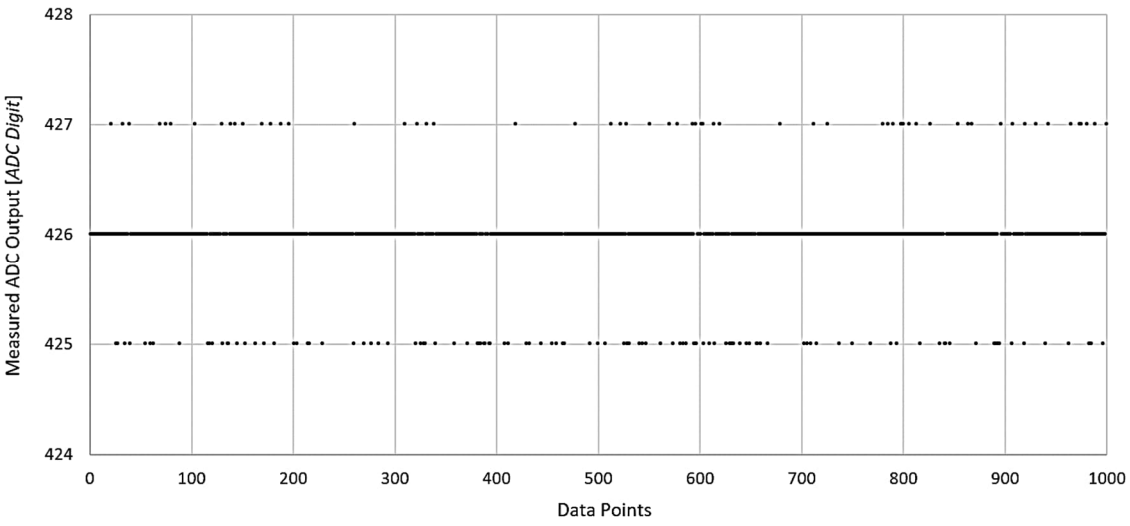

Figure A-10: IR sensor output ADC of 1000 samples at 70 mm reference distance for normal concrete surface with no light (noise calibration test)

A.7 RECONTWIN USER INTERFACE

Using the Python code and the Tkiner extension library, ReConTwin was enhanced with four interactive GUI windows to streamline processes and provide guidance and transparency to the users. These GUI windows enable users to specify preferred input parameters, automate tasks, and navigate through the ReConTwin software by interacting with graphical elements such as input fields, buttons, and display charts. The purpose of each window and their associated features are chronologically outlined below:

- GUI Window 1 – Parameter input window:
  In launching ReConTwin, Window 1 will be activated (Figure A-11) and will serve as the pre-processing interface through which the user can specify the desired analysis input parameters for the DT calibration process using the load test results.

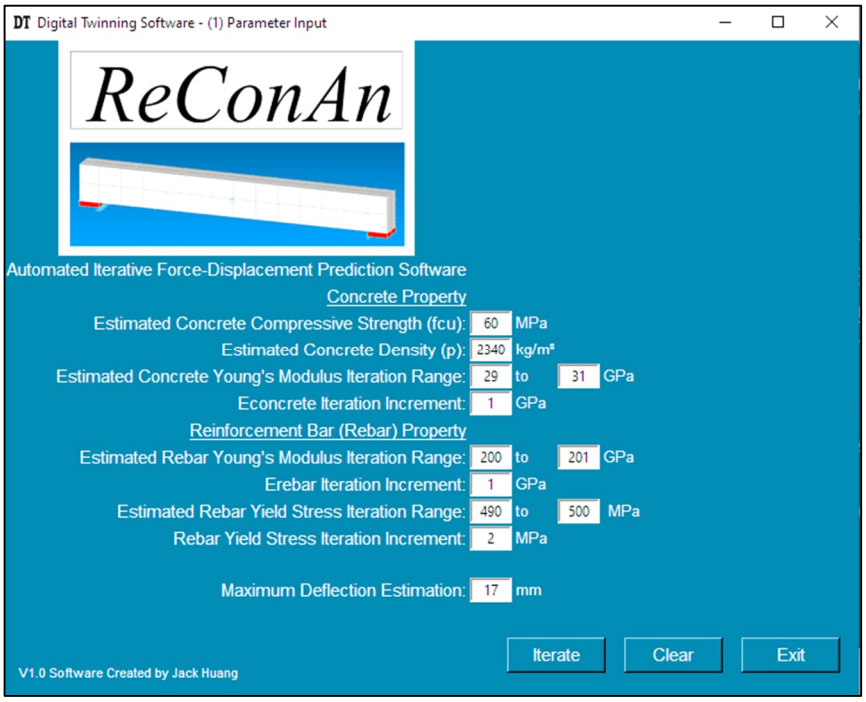

Figure A-11: GUI Window 1 – Parameter input window

The user will be prompted to provide basic information relating to the estimated concrete compressive strength and density. Additionally, the iteration ranges and increments for the three varying material properties (Young's moduli of concrete and steel, and steel yield stress) utilised in the iterative analysis process can be specified by the user in the corresponding input fields. The user can also set the upper limit of the vertical deflection to be imposed at the RC beam mid-span in the FE analysis. Upon completion of all input

fields, the user may select the “Iterate” button to proceed to GUI Window 2 and commence with the DT calibration process.

- GUI Window 2 – DT calibration window:
  In initiating the iteration process, Window 2 will activate to display the iteration progress of the DT calibration procedure (Figure A-12a). This window will inform the user about the material property combination set being analysed by *ReConAn* with which the FE baseline model possesses, and visually present the ongoing iteration progress. Additionally, an estimated remaining time to complete all iteration processes will also be provided.

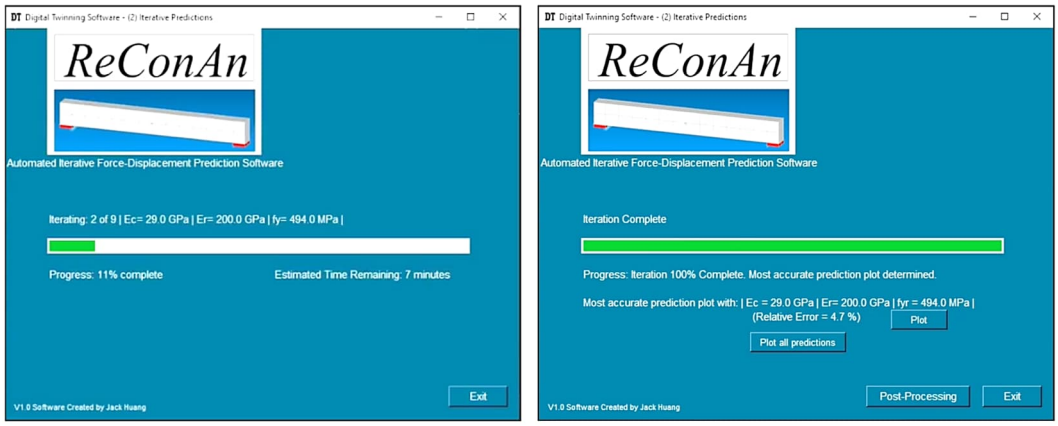

(a) (b)

Figure A-12: GUI Window 2 – DT calibration window: (a) Calibration progress display, and (b) Progress completion and result display

Once the FE analyses for all material property combination iterations are complete, the window will notify the user accordingly (Figure A-12b). The window will report the most accurate iteration material property set, which represents the DT model that could best simulate the force-displacement behaviour of the RC beam with the least relative error compared to the load test results. The corresponding relative error value will also be noted. At this point, the user will have the option to review the iteration results by generating graphical plots of either the most accurate iteration independently or all iterations predicted against the control load test results (Figure A-13). Matplotlib, a Python library extension, was used to create graphical representations in ReConTwin. The extension facilitates the creation of interactive and customisable visualisations with a wide range of graph and plot formats. Finally, the “Post-Processing” button may be selected to proceed to Window 3 for the post-processing procedures.

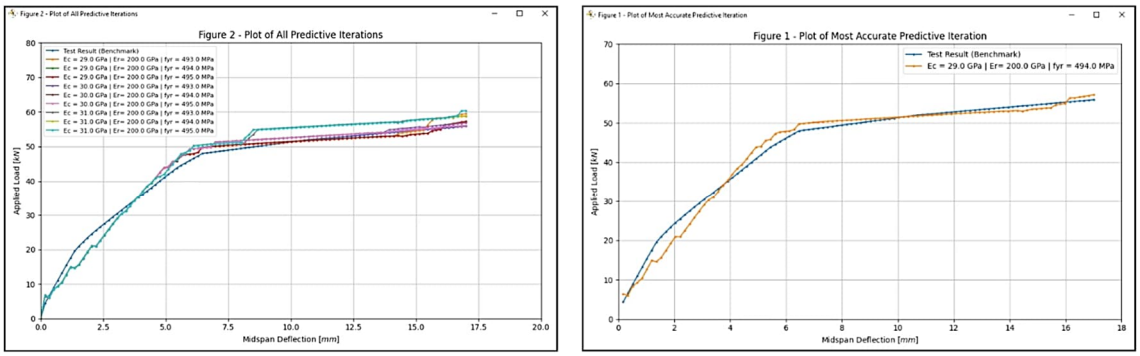

(a) (b)

Figure A-13: GUI Window 2 force-displacement plots: (a) Typical plot of all iterations against the control, and (b) Typical plot of the most accurate iteration against the control

- GUI Window 3 – Post-processing window:

  The purpose of Window 3 (Figure A-14a) is to enable the integration of sensor data retrieved from the hardware system with the calibrated DT for predicting the behaviour of the monitored RC beam under the applied mid-span load. The user can import the sensor displacement data recorded over a specified detection period, previously downloaded from the Arduino Cloud (as detailed in Chapter 3.6). Once imported, the "Plot" button can be selected to generate a historical graph of the measured displacement from the smart sensor (Figure A-15a). Concurrently, ReConTwin will determine the maximum and average deflection values during the recorded period. With this information, the user will be prompted to input the desired deflection value, which ReConTwin will adopt to estimate the imposed load (Figure A-14b).

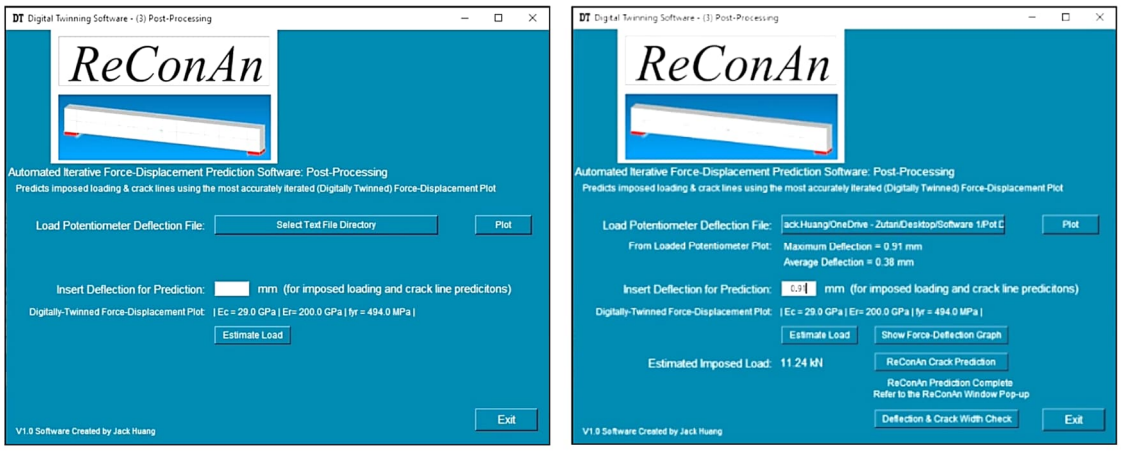

(a) (b)

Figure A-14: GUI Window 3 – Post-processing window: (a) Initial window view, and (b) Updated window after file import and load estimation

The imposed load is predicted by interpolation using the DT force-displacement graph and can be graphically illustrated after selecting the "Show Force-Deflection Graph" button (Figure A-15b). Using the same deflection value, the user can activate *ReConAn Eye* to show the predicted crack formation along the concrete beam surface by clicking the "*ReConAn* Crack Prediction" button. Finally, the user can proceed to the damage diagnosis procedure by selecting the "Deflection & Crack Width Check" button to progress to Window 4.

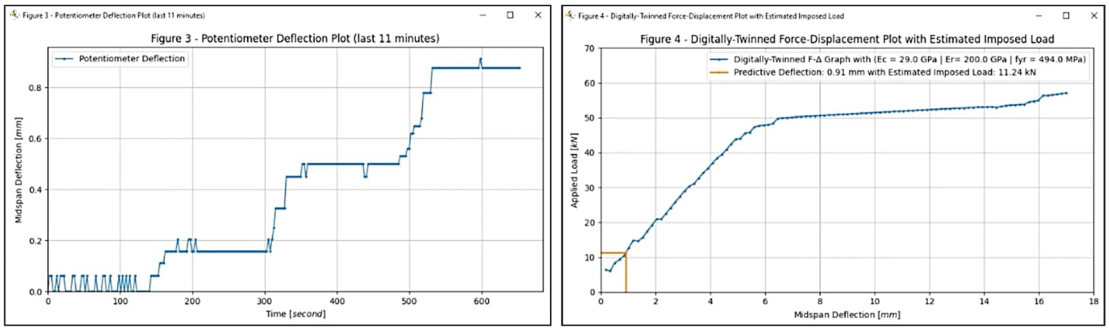

Figure A-15: GUI Window 3 plots: (a) Typical plot of the imported displacement sensor data, and (b) Typical plot of the estimated imposed load on the DT force-displacement graph

- GUI Window 4 – Damage diagnosis window:

  In the fourth and final interactive window, ReConTwin supports automated damage diagnosis based on the structural performance of the RC beam and provides recommendations on whether preventive actions are necessary (Figure A-16).

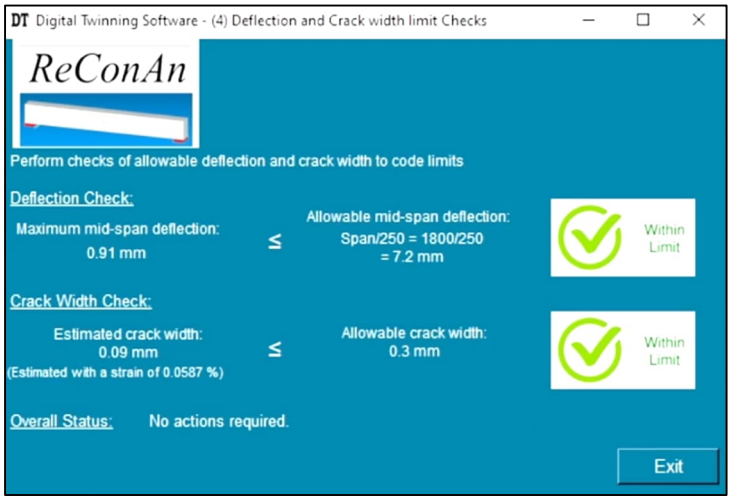

Figure A-16: GUI Window 4: Damage diagnosis

The two key structural performance indicators are assessed: allowable mid-span deflection and crack width limits. Using the deflection value specified by the user in GUI Window 3, ReConTwin verifies whether it exceeds the code-based limit of beam span/250 (or other specified code requirements). Additionally, the estimated crack width, determined under the same imposed deflection is compared against the code-based limit of 0.3 mm (or other specified code requirements). The status of both checks will also be visually indicated by either a “Within Limit” or a “Limit Exceeded” icon. If either check does not conform to the limit, ReConTwin will provide a warning under “Overall Status” and advise the user to take preventive actions.

A.8 STATISTICAL SUMMARY OF LOAD TEST STAGE 1

The statistical results derived from the three-point bending test conducted on the four RC beam specimens of Load Test Stage 1 are summarised in Table A-8. The displacement for each load step was averaged over a load maintaining duration of three minutes for each beam specimen.

Table A-8: Statistical results of measured beam mid-span displacement for four beam specimens under various applied loading

Applied Point Load	Minimum [mm]	Maximum [mm]	Mean [mm]	Standard Deviation [mm]
4 kN	0.095	0.179	0.135	0.037
8 kN	0.367	0.540	0.448	0.078
12 kN	0.664	0.888	0.779	0.116
16 kN	1.010	1.197	1.119	0.089
20 kN	1.362	1.600	1.496	0.107
24 kN	1.879	2.176	2.028	0.126
28 kN	2.561	2.923	2.731	0.154
32 kN	3.224	3.657	3.420	0.183
36 kN	3.880	4.362	4.099	0.201
40 kN	4.588	5.103	4.829	0.213
44 kN	5.296	5.893	5.569	0.248
48 kN	6.143	6.793	6.448	0.267
52 kN	9.977	11.007	10.664	0.484

A.9 DISTRIBUTED OPTIC FIBRE STRAIN MEASUREMENT

Figure A-17, Figure A-18, Figure A-19, and Figure A-20 illustrate the positive strain measurements along the beam soffit obtained from the embedded distributed optic fibre under various applied loading in Load Test Stage 1. The locations of the maximum measured strain and the beam mid-span are also graphically indicated.

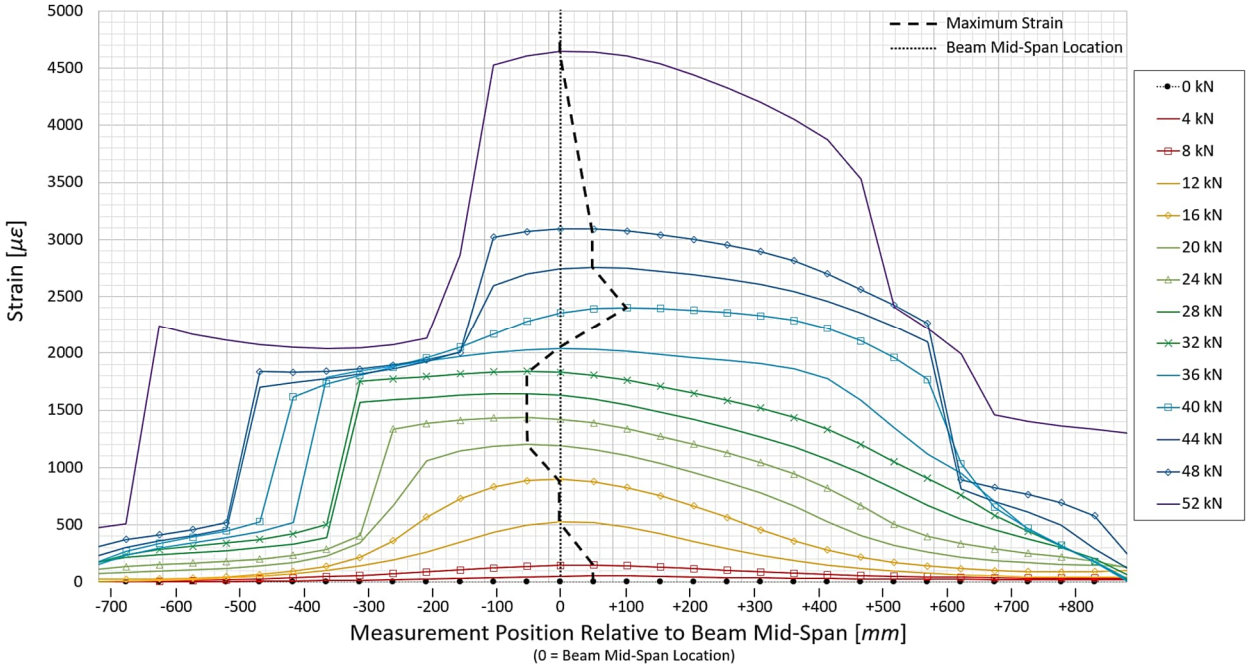

Figure A-17: Distributed optic fibre strain at mid-span soffit of Beam 1 under various applied loads (Load Test Stage 1)

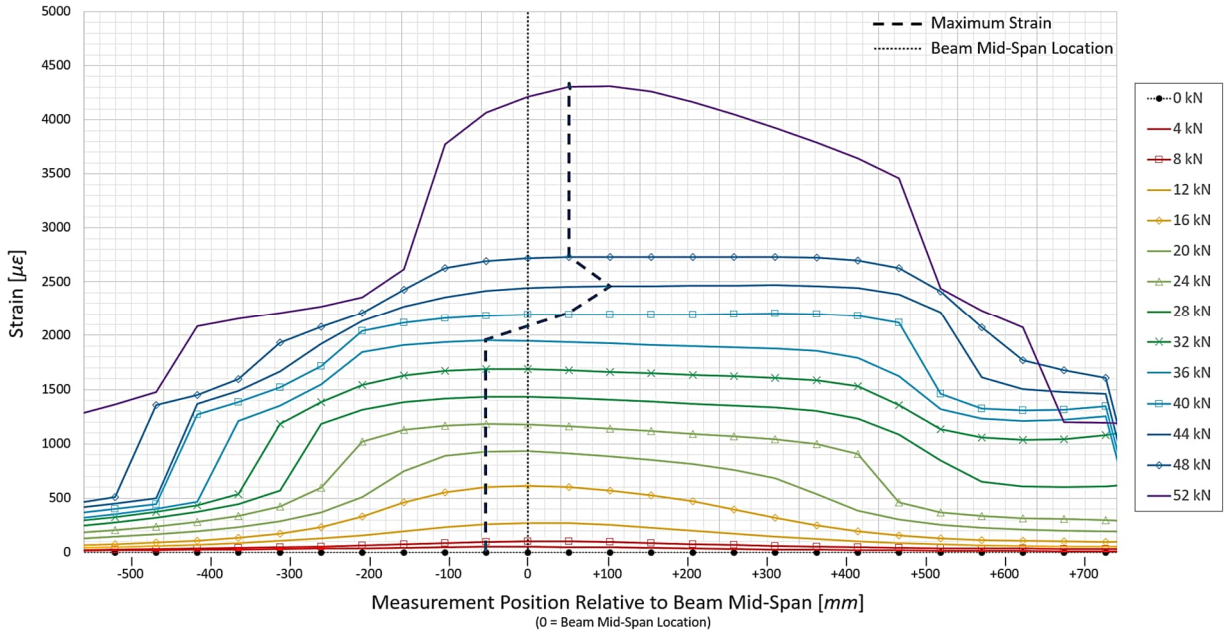

Figure A-18: Distributed optic fibre strain at mid-span soffit of Beam 2 under various applied loads (Load Test Stage 1)

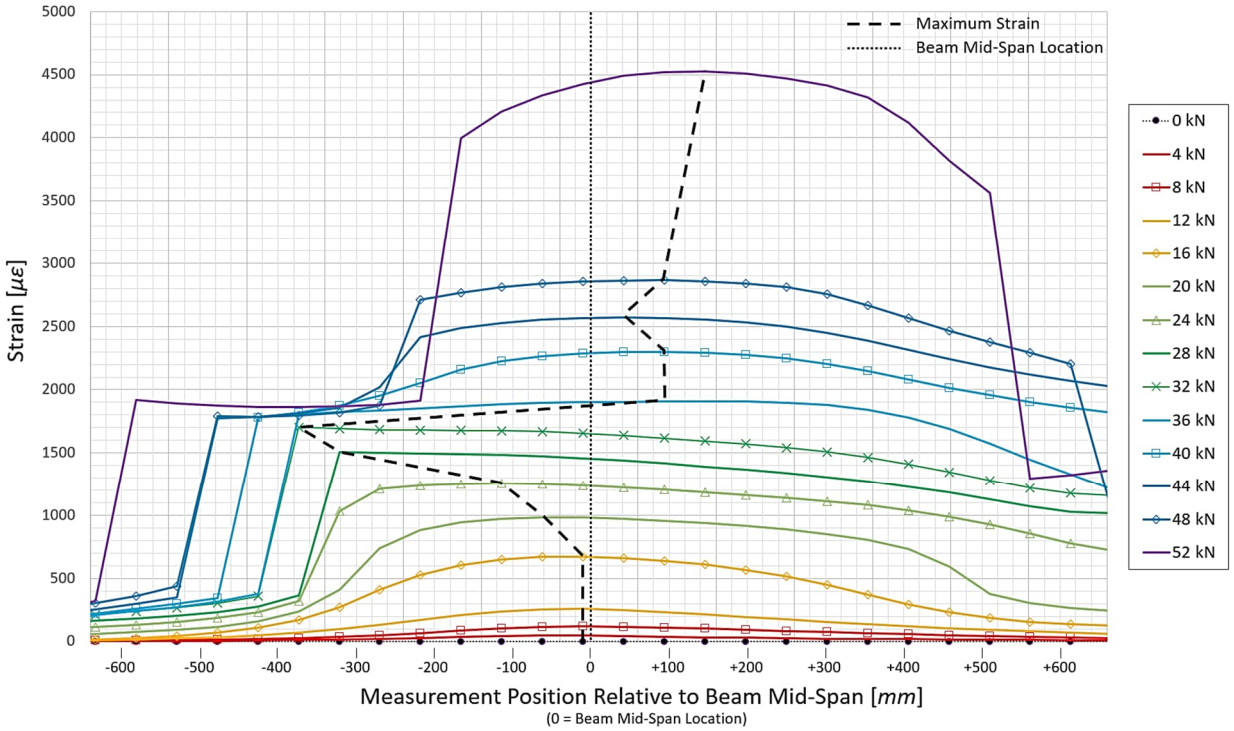

Figure A-19: Distributed optic fibre strain at mid-span soffit of Beam 3 under various applied loads (Load Test Stage 1)

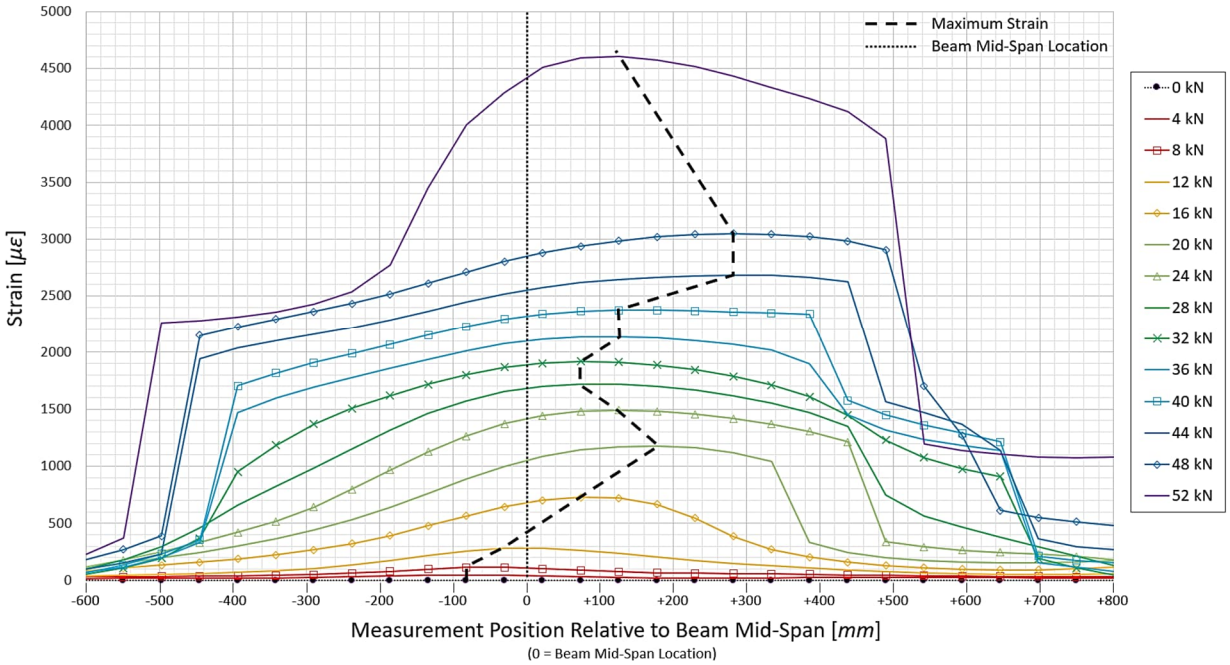

Figure A-20: Distributed optic fibre strain at mid-span soffit of Beam 4 under various applied loads (Load Test Stage 1)

A.10 LOAD TEST STAGE 2 – PHASE 1 RESULTS

Figure A-21, Figure A-22, Figure A-23, and Figure A-24 illustrate the measured vertical displacements of the contact (potentiometer) and non-contact (IR) sensors, compared to the control result (LVDT) obtained during the static-cyclic load test of Phase 1, Load Test Stage 2.

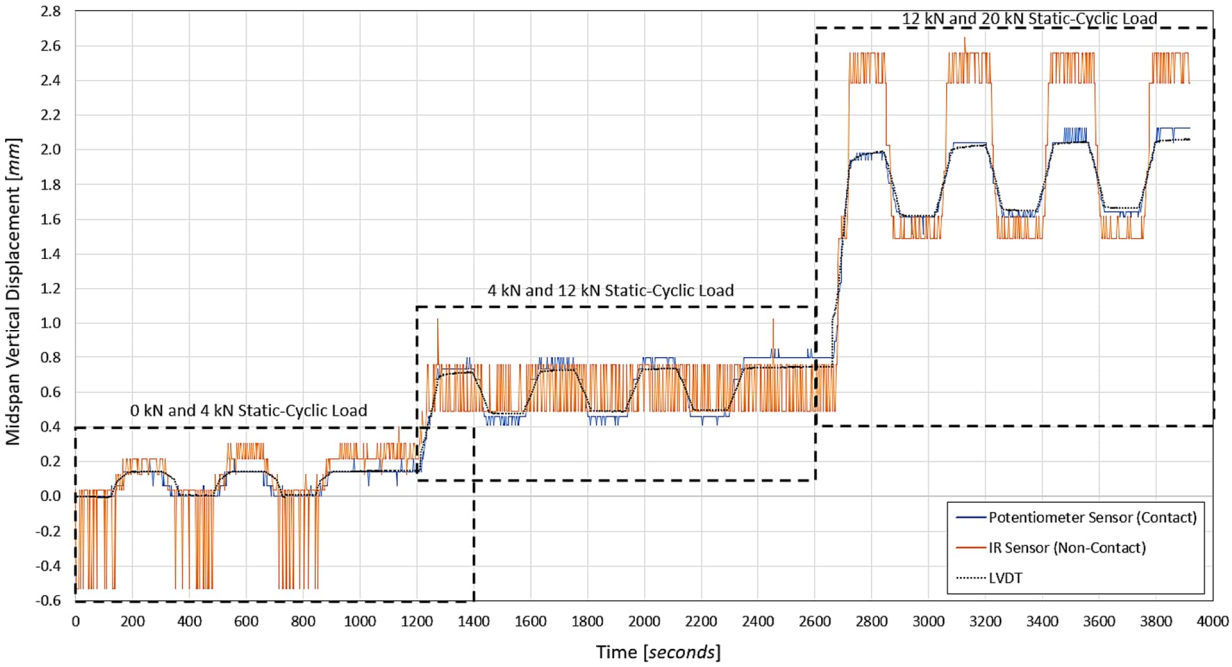

Figure A-21: Overall static-cyclic test displacement results (Phase 1, Load Test Stage 2)

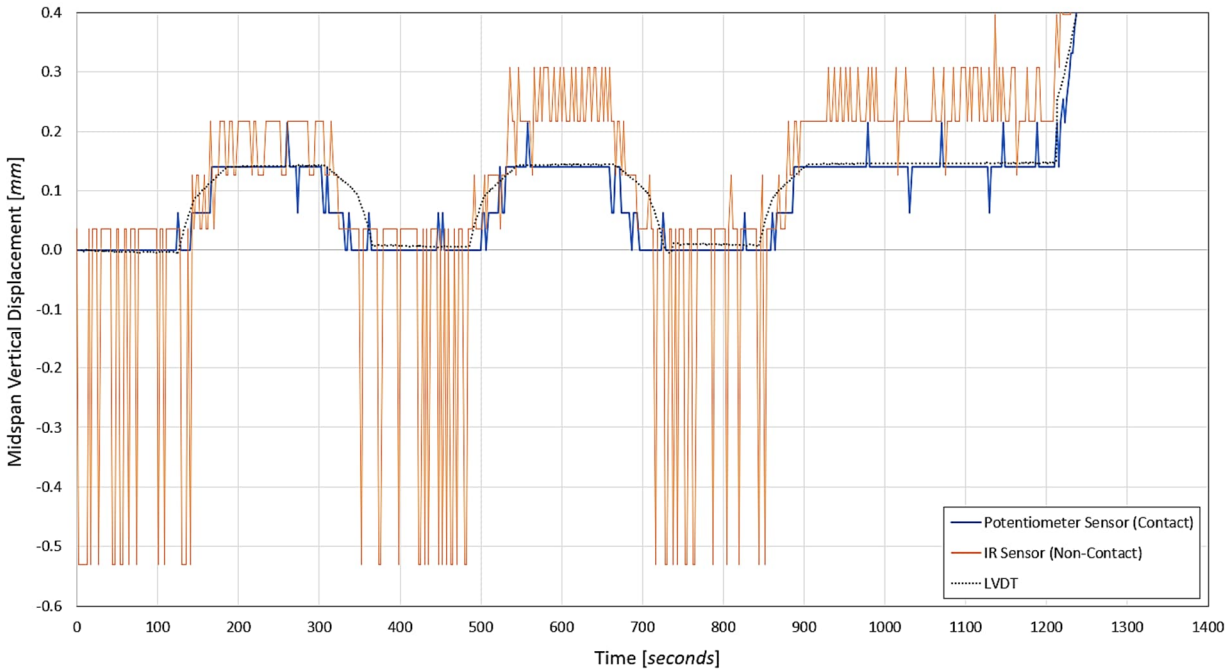

Figure A-22: Detailed static-cyclic test displacement results between 0 kN & 4 kN (Phase 1, Load Test Stage 2)

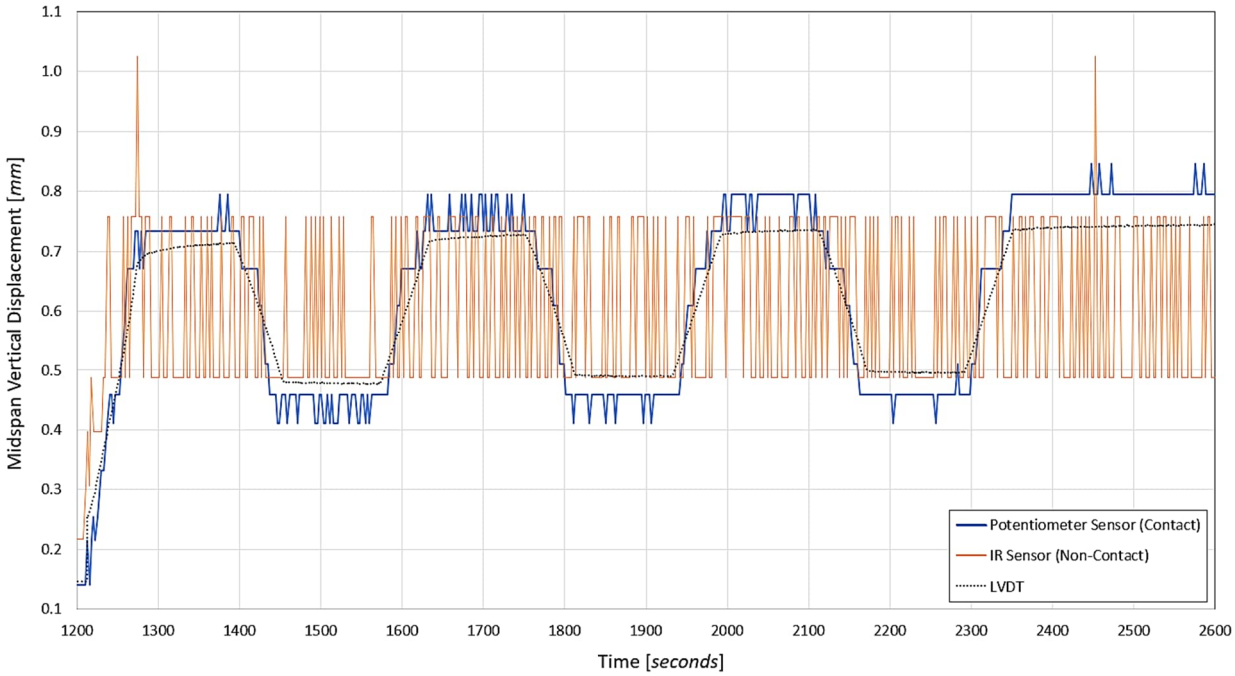

Figure A-23: Detailed static-cyclic test displacement results between 4 kN & 12 kN (Phase 1, Load Test Stage 2)

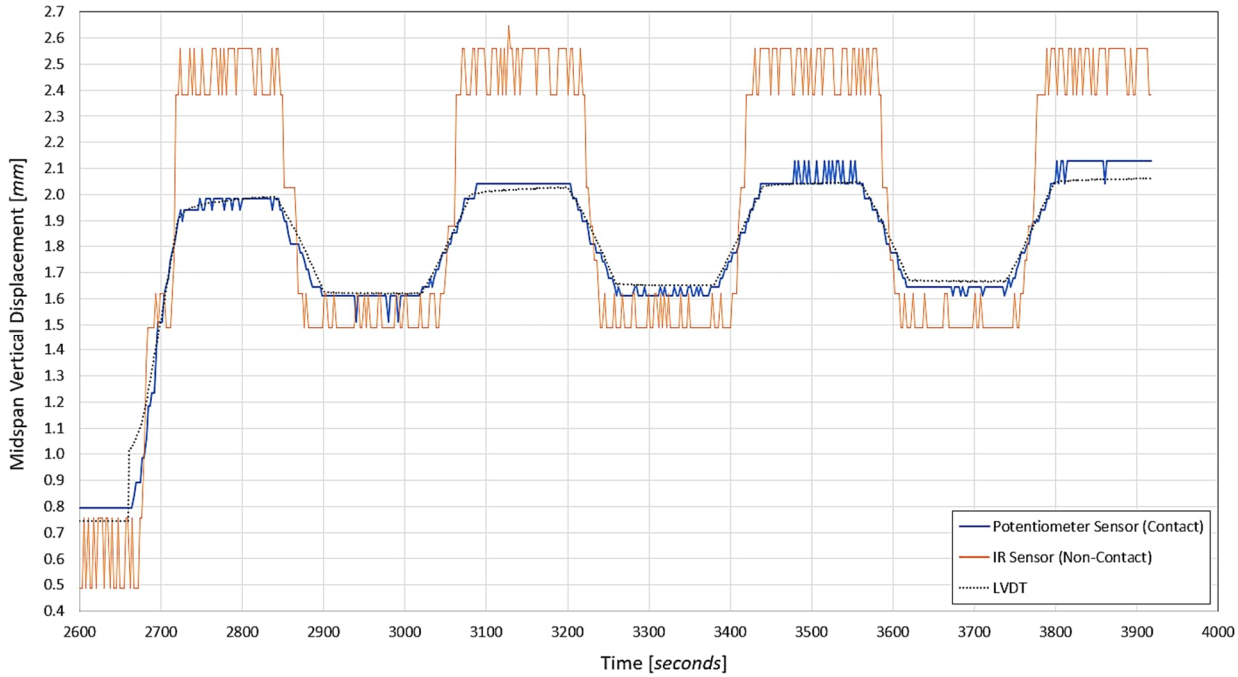

Figure A-24: Detailed static-cyclic test displacement results between 12 kN & 20 kN (Phase 1, Load Test Stage 2)

A.11 LOAD TEST STAGE 2 – PHASE 2 RESULTS

Figure A-25, Figure A-26, Figure A-27, and Figure A-28 illustrate the measured vertical displacements of the contact (potentiometer) and non-contact (IR) sensors, compared to the control result (LVDT) obtained during the static-incremental load test of Phase 2, Load Test Stage 2.

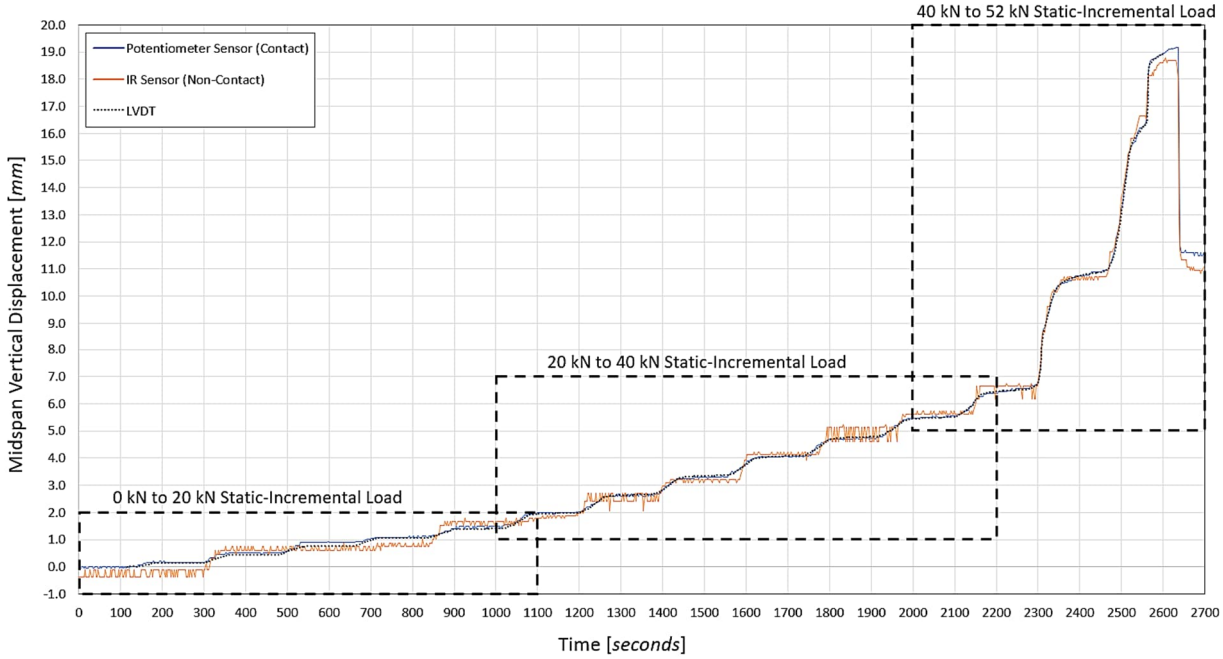

Figure A-25: Overall static-incremental test displacement results (Phase 2, Load Test Stage 2)

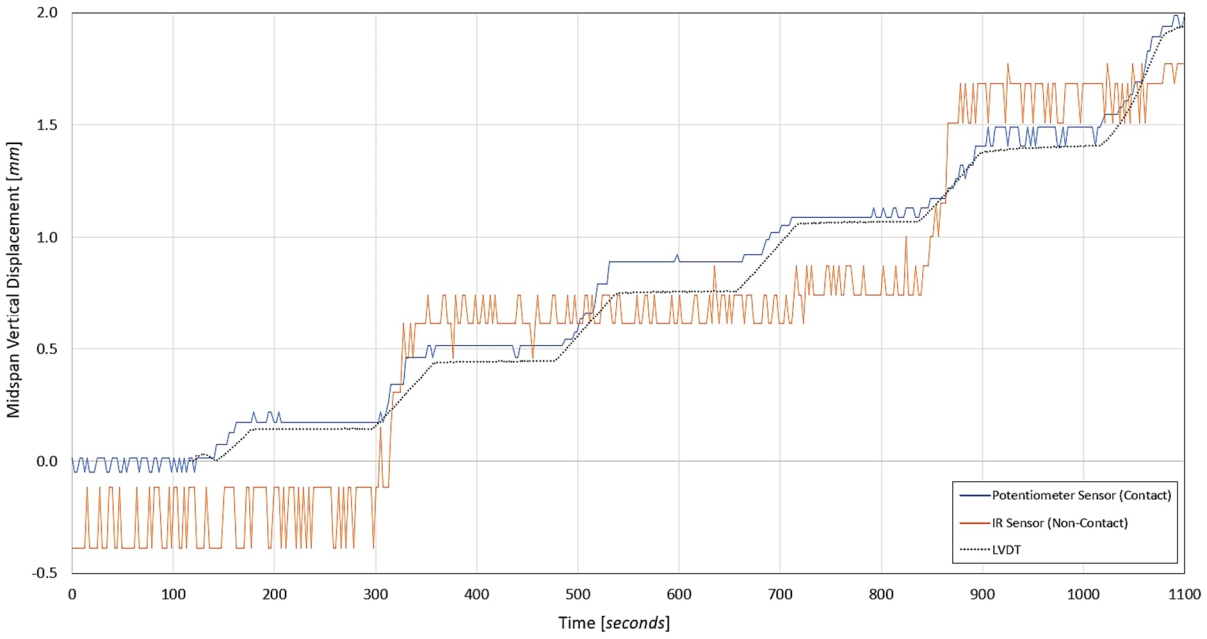

Figure A-26: Detailed static-incremental test displacement results from 0 kN to 20 kN (Phase 2, Load Test Stage 2)

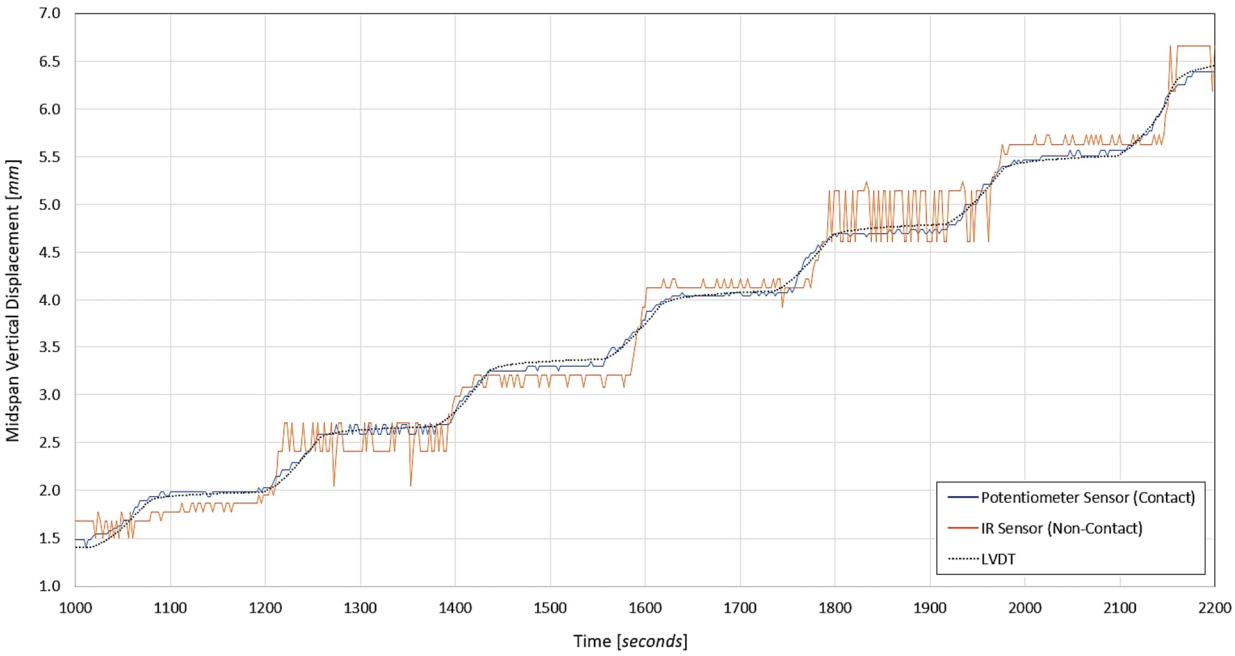

Figure A-27: Detailed static-incremental test displacement results from 20 kN to 40 kN (Phase 2, Load Test Stage 2)

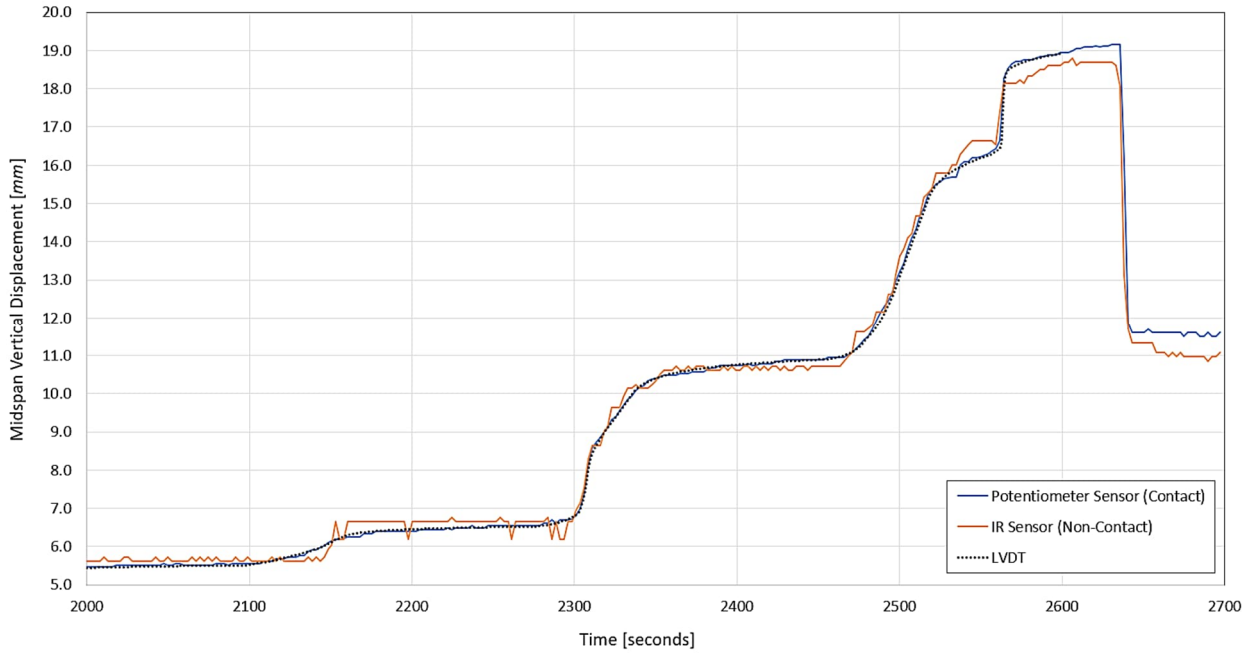

Figure A-28: Detailed static-incremental test displacement results from 40 kN to 52 kN (Phase 2, Load Test Stage 2)

This page is intentionally left blank.